ISLEY-733

NASA CONTRACTOR REPORT

NASA CR-2073



NASA CR-2073

NASA CR-2073

EVALUATION OF THE THIN DEFORMABLE ACTIVE OPTICS MIRROR CONCEPT

by Hugh J. Robertson

Prepared by
OPTICAL GROUP
PERKIN-ELMER CORPORATION
Norwalk, Conn. 06852
for Langley Research Center

NATIONAL AERONAUTICS AND SPACE ADMINISTRATION • WASHINGTON, D. C. • JUNE 1972

19720020816 IR

1. Report No.	2. Government Accession No.	3. Recipient's Catalog No.
NASA CR-2073		

4. Title and Subtitle	5. Report Date
EVALUATION OF THE THIN DEFORMABLE ACTIVE OPTICS MIRROR CONCEPT	June 1972
	6. Performing Organization Code
7. Author(s)	8. Performing Organization Report No.
Hugh Robertson	Engineering Report No. 10859
9. Performing Organization Name and Address	10. Work Unit No.
Optical Group Perkin-Elmer Corporation Norwalk, Conn. 06852	188-78-57-07
	11. Contract or Grant No.
	NAS1-9759
12. Sponsoring Agency Name and Address	13. Type of Report and Period Covered
National Aeronautics & Space Administration Washington, DC 20546	Contractor Report
	14. Sponsoring Agency Code

15. Supplementary Notes

16. Abstract

The Active Optics concept using a thin deformable mirror has been successfully demonstrated using a 30" diameter, 1/2" thick mirror and a 61 point matrix of forces for alignment. Many of the problems associated with the design, fabrication, and launch of large aperture diffraction-limited astronomical telescopes have been resolved and experimental data created that can provide accurate predictions of performance in orbit.

17. Key Words (Suggested by Author(s))	18. Distribution Statement
Optics Active optics Mirror Diffraction-limited Telescopes Distributed parameter	Unclassified - Unlimited

19. Security Classif. (of this report)	20. Security Classif. (of this page)	21. No. of Pages	22. Price*
Unclassified	Unclassified	144	$3.00

*For sale by the National Technical Information Service, Springfield, Virginia 22151

TABLE OF CONTENTS

Para.	Title	Page
1.0	INTRODUCTION	1
	1.1 Objectives	1
	1.2 Summary of Results	3
	1.2.1 Range of Mirror Control	3
	1.2.2 Experimental Determination of Influence Coefficients	3
	1.2.3 Thermal Measurements	3
	1.2.4 Modal Control Using Natural Modes of Mirror Vibration	4
	1.2.5 Control System Response to Step Error Disturbances	5
	1.2.6 Feedforward Localization	5
2.0	RANGE OR MIRROR CONTROL	6
3.0	EXPERIMENTAL DETERMINATION OF INFLUENCE COEFFICIENTS	18
4.0	THERMAL MEASUREMENTS	40
	4.1 Thermal Instrumentation	46
	4.2 Test Method	53
	4.3 Results	55
	4.4 Conclusions	72
5.0	MODAL CONTROL	73
	5.1 Introduction	73
	5.2 System Analysis	75
	5.3 Verification of Modal Control Approach	79
	5.3.1 Selected Configuration	79
	5.3.2 Design Procedure	82
	5.3.3 Implementation of Controller Design	90
	5.3.4 Experimental Results with Modal Controller	95
6.0	TRANSIENT RESPONSE TO STEP ERROR	104
7.0	FEEDFORWARD LOCALIZATION	108
8.0	REFERENCES	111
	APPENDIX A- DERIVATION OF MIRROR SUPPORT SYSTEM EIGENFUNCTIONS	A-1
	A-1 Analytical Approach	A-2
	A-2 Experimental Determination of Modal Contours by Time-Lapse Holography	A-16
	A-3 Relation Between Modal Control Law and Mirror Stiffness Control Law	A-24

LIST OF ILLUSTRATIONS

Figure	Title	Page
1-1	30-Inch Diameter, Thin, Deformable Mirror and Actuator Assembly	2
2-1	Scanner, Optical Schematic Diagram	7
2-2	Mirror Figure Error Versus Change in Radius of Mirror Curvature	9
2-3	Pinhole Image Profile Scans at Best Mirror Alignment with 58 Actuators	10
2-4	Interferogram, Pinhole Image, and Pinhole Image Scans for Best Mirror Alignment with 58 Actuators	11
2-5	Interferogram, Pinhole Image, and Pinhole Image Scans for Mirror Aligned with 58 Actuators, 0.100" from Position of Best Alignment	12
2-6	Interferogram, Pinhole Image, and Pinhole Image Scans for Mirror Aligned with 58 Actuators, 0.225" from Position of Best Alignment	13
2-7	Interferogram, Pinhole Image, and Pinhole Image Scans for Mirror Aligned with 16 Actuators, 0.050" from Position of Best Alignment	14
2-8	Interferogram, Pinhole Image, and Pinhole Image Scans for Mirror Aligned with Four Actuators, 0.015" from Position of Best Alignment	15
2-9	Interferogram, Pinhole Image, and Pinhole Image Scans for Mirror Aligned with Four Actuators, 0.030" from Position of Best Alignment	16
3-1	Interferogram of Mirror with 3-Pound Force Applied at Center After Alignment	19
3-2	Stiffness Coefficient (for Local Displacement at Center of Mirror)	21
3-3	Interferograms of Mirror Deformed by 1-Pound Force at Various Actuator Locations	22
3-4	Actuator Locations at Which 1-Pound Force is Applied in Figure 3-3	23

LIST OF ILLUSTRATIONS (Continued)

Figure	Title	Page
3-5	Typical Influence Coefficient Reduction from Interferogram	24
3-6	Measured Influence Coefficients	26
4-1	Projected Thermal Profiles	41
4-2	Heater Blanket	43
4-3	Circumference Heater Blanket	44
4-4	Profiles to 700Km of Temperature, Pressure, and Molecular Weight	45
4-5	Recommended Correlation for Free Convection around Vertical Plane Surfaces	47
4-6	Thermocouple Arrangement on Back of 30-Inch Mirror	48
4-7	Thermocouple Arrangement on Front of 30-Inch Mirror	49
4-8	Thermocouple Arrangement as seen from Back of Mirror	51
4-9	Thermal Control Panel and Thermocouple Jack Panel	52
4-10	Automatic Heater Temperature Control	54
4-11	Mirror Deformations Due to Axisymmetric Distributed Thermal Gradients, Numbers 1 through 4	57
4-12	Distributed Thermal Gradient, Number 5 and Resultant Mirror Deformation	58
4-13	Localized Thermal Gradients Applied to Mirror	59
4-14	Interferograms Showing Mirror Deformations Due to Distributed Gradients of Figure 4-11(a)	60
4-15	Interferograms Showing Mirror Deformations Caused by Local Thermal Gradients of Figure 4-13	61
4-16	Localized Thermal Gradient, Number 1 and Resultant Mirror Deformation	62
5-1	Model of Modal Control System	76
5-2	Partitioned Model of Modal Control System	76

LIST OF ILLUSTRATIONS (Continued)

Figure	Title	Page
5-3	Nodal Contours of First Seven Dominant Modes	80
5-4	Superposition of Nodal Contours for Modes 5,6, and 7	81
5-5	Actuator Numbering Arrangement	83
5-6	OP-AMP Resistor Realization of Controller	87
5-7	Mode Analyzer, U_N^{-1} (Controlled Modes)	88
5-8	Mode Analyzer (Uncontrolled Modes)	89
5-9	Pad Compensator, H_N^{-1}	91
5-10	Layout of Modal Controller	92
5-11	Four Actuator Modal Controller Breadboard Unit	94
5-12	Open Loop Phase and Mode Errors versus Force Applied at Uncontrolled Actuator No. 28.	96
5-13	Phase and Mode Errors and Corrective Forces with Closed Loop Corrections for Point Force Error	98
5-14	Mirror Deformation Produced by 0.175 lb. Force Applied by Actuator No. 28	99
5-15	Open Loop Phase and Mode Errors versus Axial Spacing Between Mirror and Figure Sensor	100
5-16	Phase and Mode Errors and Corrective Forces with Closed Loop Correction for Axial Error	102
5-17	Change in Axial Spacing Between Mirror and Figure Sensor	103
6-1	Transient Response with Straight-Parallel Control Loops ..	105
6-2	Transient Response with Feedforwards	106
6-3	Transient Response with Modal Controller	107
7-1	Interferograms Showing "Localized" Deflections Produced by Feedforward Network	109
A-1 thru A-12	Deflection Modes	A-4 thru A-15

LIST OF ILLUSTRATIONS (Continued)

Figure	Title	Page
A-13	Normalized Exposure as a Function of Vibration Amplitude for a Time-Lapse Hologram	A-17
A-14	Interferograms of Vibrating Mirror at 272 Hz	A-19
A-15	Modal Contours Derived from Exposure in Figure A-14	A-20
A-16	Modal Contours Taken from SAMIS Program	A-21
A-17	Interferogram of Vibrating Mirror at 296 Hz	A-22
A-18	Interferograms of Vibrating Mirror	A-23

EVALUATION OF THE THIN DEFORMABLE ACTIVE OPTICS MIRROR CONCEPT

By Hugh J. Robertson

The Perkin-Elmer Corporation

1.0 INTRODUCTION

1.1 OBJECTIVES

The Active Optics concept using a thin deformable mirror has been successfully demonstrated using a 30" diameter, 1/2" thick mirror (figure 1-1) and a 61 point matrix of forces for alignment*. Many of the problems associated with the design, fabrication, and launch of large aperture diffraction-limited astronomical telescopes have been resolved and experimental data created that can provide accurate predictions of performance in orbit.

The work that has been performed under this contract was designed to further evaluate the present system to determine its parameters more completely in order to facilitate the optimum design for larger active telescopes. Specifically the evaluation included the following tasks as design objectives:

1. Determination of the maximum degree of control possible as a function of actuator spacing. (The range of radius of curvatures that the mirror can assume with a given number of actuators.)

2. Experimental determinations of mirror influence coefficients.

3. Determination of the effects of thermal gradients on the thin mirror and the ability of the control system to accommodate these effects.

4. Determination, implementation, and evaluation of an actuator arrangement designed to take advantage of natural modes of deflection of the mirror. In particular it was desired to determine the optimum positioning of actuators and distribution of actuator forces in order to minimize the number of control channels required and to decouple their action so as to optimize system response.

---

*Reference No. 1

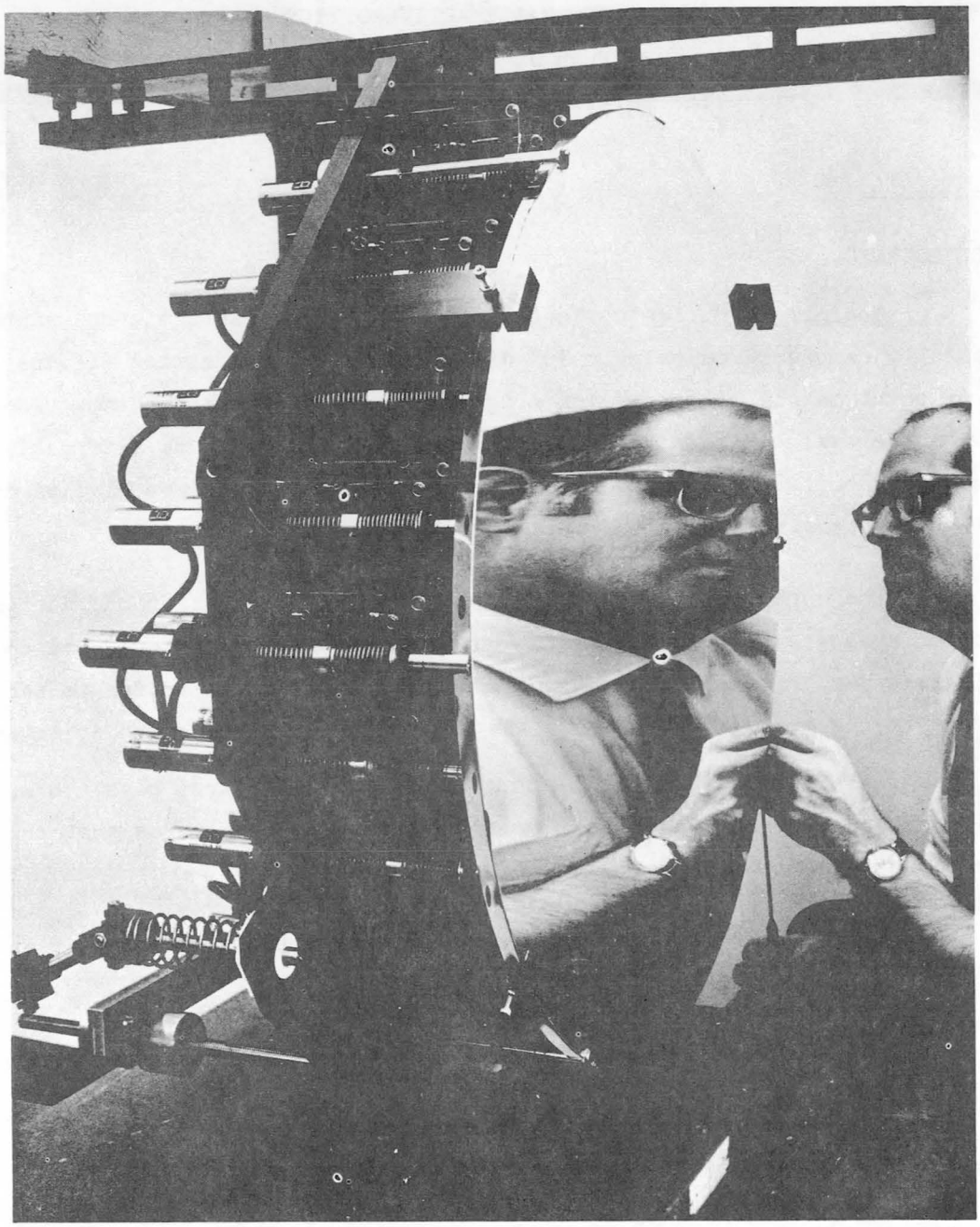


Figure 1-1. 30-Inch Diameter, Thin, Deformable Mirror and Actuator Assembly

5. Determination of the response of the control system to step error disturbances with and without feedforwards for each actuator arrangement.

6. Determination of the degree to which localization is achieved using the force patterns derived analytically under NASA Contract NAS 1-7103.

1.2 SUMMARY OF RESULTS

1.2.1 Range of Mirror Control

The range of radius of curvatures that the active thin mirror could assume was investigated and the figure error was plotted against change in radius of curvature using 4, 16, and 58 actuators. The mirror figure was observed to deteriorate exponentially as the radius varied from the minimum error alignment position, at a rate inversely proportional to the number of actuators used. The 58 actuators with a maximum force capability of ±2 pounds were able to change the radius of curvature over a range of approximately 1/2 inch. The effects of the changes of curvature on the mirror figure and its ability to image a pinhole source were documented using interferograms, pinhole photographs and pinhole image profile scans.

1.2.2 Experimental Determination of Influence Coefficients

To obtain accurate experimental data on the 30-inch thin mirror in order to provide more precise calibration of analytical determination techniques, the mirror influence coefficients were measured. The mirror influence coefficients were determined experimentally by measuring the displacement of the stressed mirror at various points, from interferograms. The necessary data was acquired and reduced to give a full set of the individual rows of the influence coefficient matrix.

1.2.3 Thermal Measurements

The thermal effects induced by the space environment and the resulting optical performance of a large aperture diffraction limited system

is a major problem area that bears more detailed analytical and experimental investigation. Once the anticipated temperature and temperature changes have been established, the resulting effect on performance can be predicted and proper open or closed loop compensation can be designed into the system and/or spacecraft. As yet, however, no complete analytical solution to the thermo-elastic problem in large primary mirrors has been developed. Among other things, the solution requires the development of mathematical models of complex mirror structures. This represents a tedious, time-consuming and extremely complex analytical problem and can best be handled via suitable approximations once parameters can be experimentally determined.

The thermal program was undertaken to experimentally determine figure degradation and focus shifts resulting from various thermal inputs to a thin, 30-inch diameter, 1/2-inch thick deformable mirror. The induced thermo-elastic deformations of a 30-inch diameter, 1/2-inch thick, fused silica primary mirror were recorded with a phase measurement interferometer, and the ability of the active control system to maintain alignment in the presence of thermal gradients was assessed. Various thermal patterns were developed in the test mirror by 26 electric heater pads located at the mirror back and edge surfaces. The temperatures at the mirror surfaces were measured by approximately 105 five-mil thermocouples that were attached to the mirror. The tests were conducted in a horizontal vacuum tank with the mirror supported in the Active Optics System to simulate the gravity-free environment experienced in space.

The results of the thermal measurements show that localized gradients generated by small area heat sources on the back of the mirror produce localized deformations. It should be possible to predict the effect of distributed gradients of low spatial frequency by linear superposition of the deformations due to localized gradients that add up to the distributed gradient.

1.2.4 Modal Control Using Natural Modes of Mirror Vibration

Using the modal control approach* the final figure error of a deformable mirror with a given actuator configuration in an active control system, can be decreased relative to the final error achieved by the technique

*Reference No. 2

of nulling the figure error in the vicinity of each actuator. The corollary to this is that the number of actuators required to reduce an initial figure error a specific amount to reach a given design figure error can be significantly less for a modal control system than for a straight nulling system.

The technique of modal control was investigated using the natural modes of vibration of the mirror as an orthogonal set. Analysis of the natural vibrational modes of a mirror simply supported at three points yielded solutions that showed good agreement with modal contours experimentally observed by time lapse holography. The initial figure error of the 30-inch thin mirror was analyzed in terms of the vibrational modes, and the number and location of actuators required to reduce the largest modal components was investigated.

Because of the complexity of the problem for any large number of actuators, a limited number of actuator and sensor points were selected to demonstrate the performance of the control approach. The controller for a four actuator and seven sensor point arrangement was tested, and the results established that the modal control approach performs as predicted.

1.2.5 Control System Response to Step Error Disturbances

The control system response was investigated using step errors introduced at individual actuators and step errors introduced in the axial spacing between mirror and figure sensor. Errors were applied to the system for straight parallel control, feedforward decoupling, and modal control configurations.

1.2.6 Feedforward Localization

The degree to which localization was achieved using the 19 point force patterns generated under NAS 1-7103 was investigated. It was found that the force patterns were not being achieved due to actuator dead zones. Readjustment of driving point resistance values provided a very high degree of localization, however, by producing seven-point force patterns.

2.0 RANGE OF MIRROR CONTROL

It might be desirable for some applications for an active system to be able to change the radius of curvature of the mirror, possibly enough to produce a more useful aspheric surface. As will be shown, a spherical profile can be maintained over a range of radii. The exact range that can be obtained with a given number of actuators before the mirror figure deteriorates as a result of a buildup of excessive ripple between the actuators was investigated. The performance of the mirror as it approaches the limits of control was evaluated primarily from interferograms and scanning of the pinhole image.

The pinhole image scanner, shown in figure 2-1, consists of a high power microscope objective which enlarges the image and refocuses it on a pinhole. A motor driven micrometer moves this pinhole across the image, with the transmitted light entering a photomultiplier tube. A chart recorder records the photomultiplier output. Repeated scans provide an accurate mapping of the image intensity profile.

A low power objective, beamsplitter, and eyepiece is used to view the image by eye and allow coarse alignment of the pinhole. A field lens in front of the photomultiplier assures that the light entering the tube will always fall on the same part of the tube face, eliminating the effect of non-uniform response of the photocathode.

The pinhole is removable to allow viewing the whole image and also to permit different sized pinholes to be used.

The figure error of the mirror is a minimum at only one axial position. This position was found by computer analysis of straight-fringe interferograms taken with the mirror aligned at different points throughout the focus range of the system. This was done first with the whole system of 58 actuators operating. After the best-focus position was established, the mirror was aligned at that position and the focus was again changed with only 16 actuators active and finally with only four actuators.

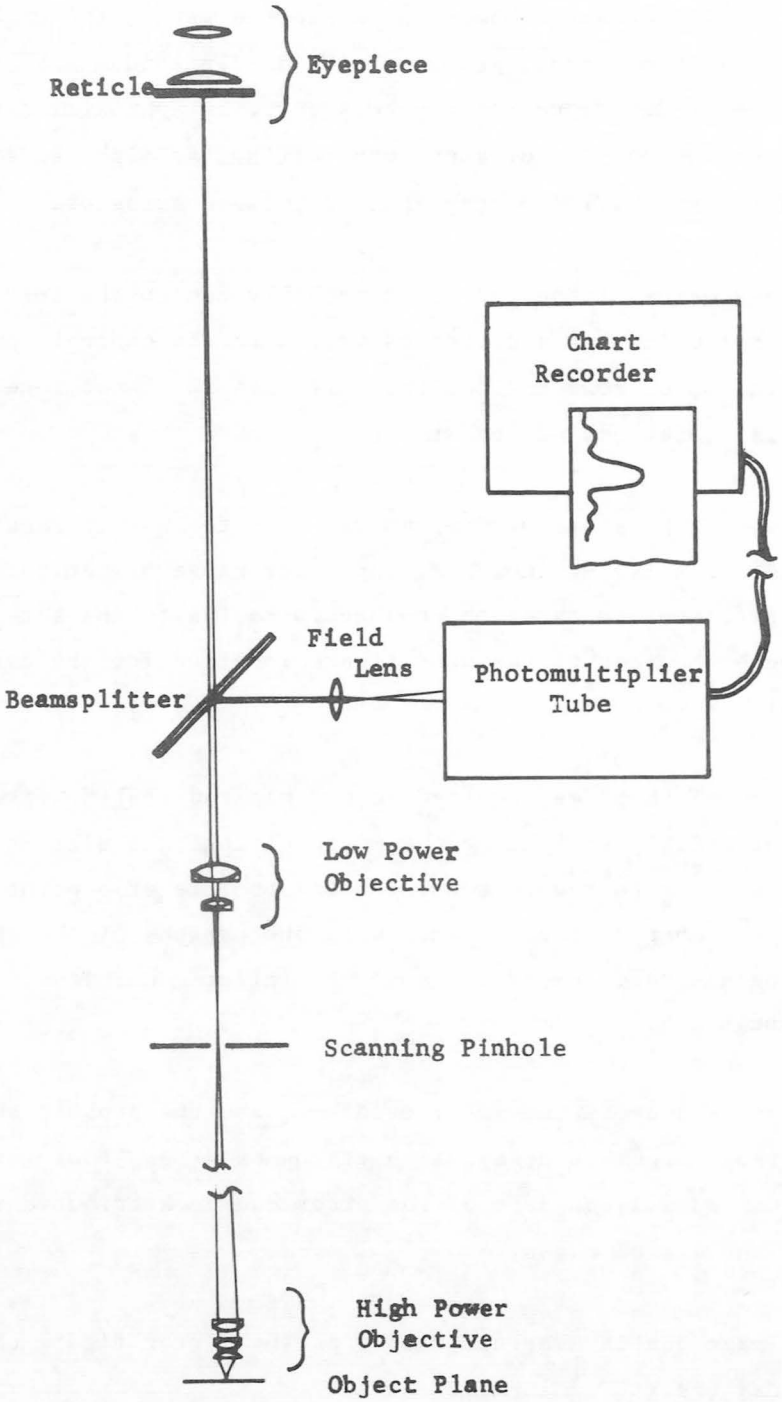


Figure 2-1. Scanner, Optical Schematic Diagram

The rms figure error observed is plotted versus the change in radius of curvature of the thin mirror, produced with 58, 16, and 4 actuators, in figure 2-2. The rate of deterioration can be seen to be approximately inversely proportional to the number of actuators controlling, as might be expected simply from geometrical consideration of the spacing between actuators.

The asymmetry of the curves is probably due to the initial figure error of the mirror which has a different radius in the central zone of the mirror than in the outer zone so that the best fits for these zones may occur at different axial locations of the mirror.

The spring constant of the central actuator was increased to extend the range of radii available. However, the force range of peripheral actuators was still not sufficient to carry the change in radius to the same level of deterioration on both sides of the best figure location for the case of the 58 actuator control.

Because of the time required to process and analyze interferograms, another method of quickly evaluating the mirror figure was also used. This involved using the image scanner to record the intensity profile of a point source imaged by the mirror. A number of these scans, with photographs of the image and associated interferograms taken under the same or similar conditions, are shown in figures 2-3 through 2-9.

As can be seen in the interferograms, and the pinhole photos and profiles, the errors occur in hexagonal patterns as a result of the actuator location pattern, and a large part of the error can be attributed to the uncontrolled area at the mirror edges.

The image quality varies greatly as the mirror figure changes and, for small degradations ($< \frac{1}{8} \lambda$ rms),

$$I_m \sim 1 - \left(\frac{4\pi}{\lambda}\right)^2 \left(\quad\right)^2 \qquad (1)$$

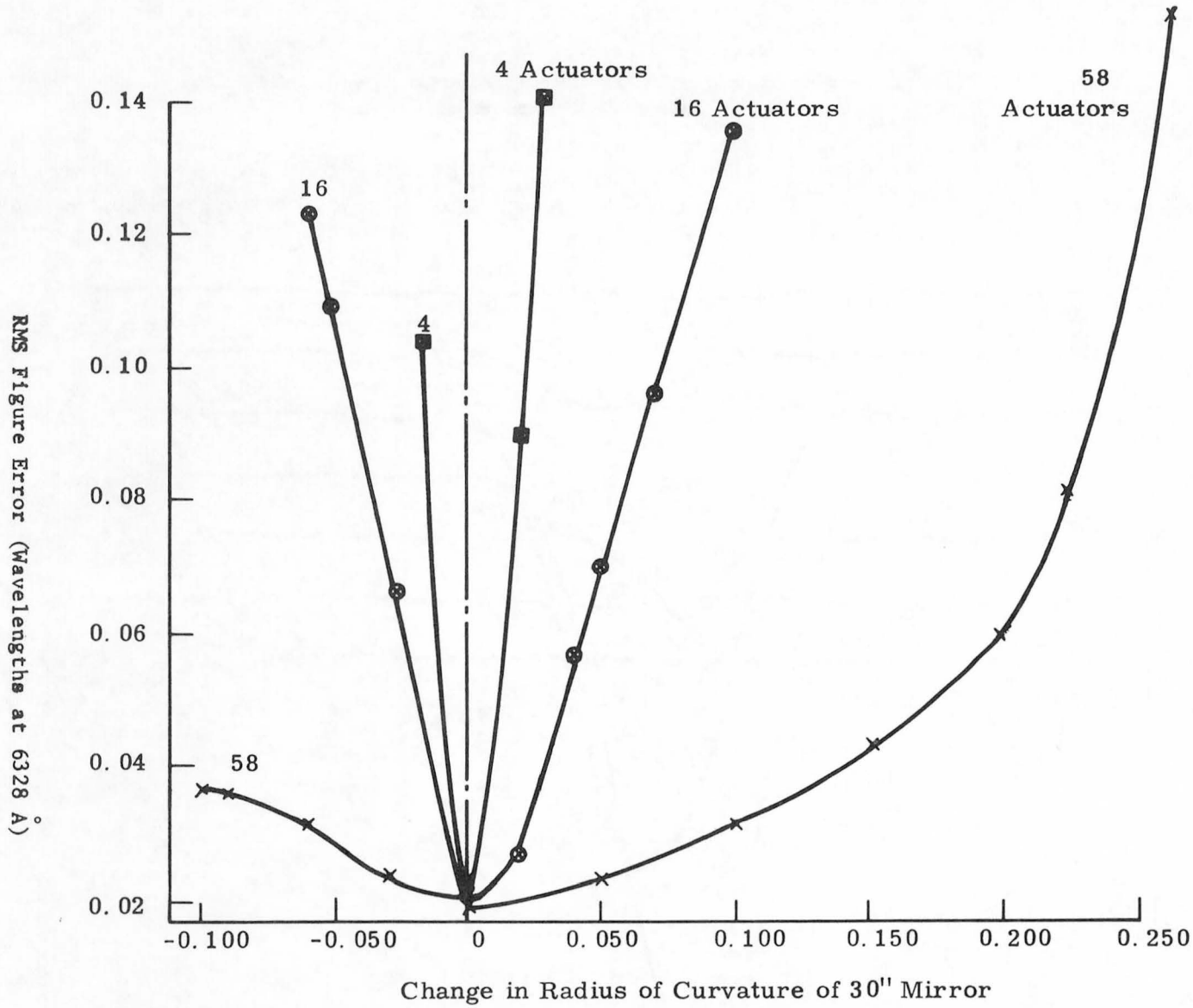


Figure 2-2 Mirror Figure Error versus Change in Radius of Mirror Curvature

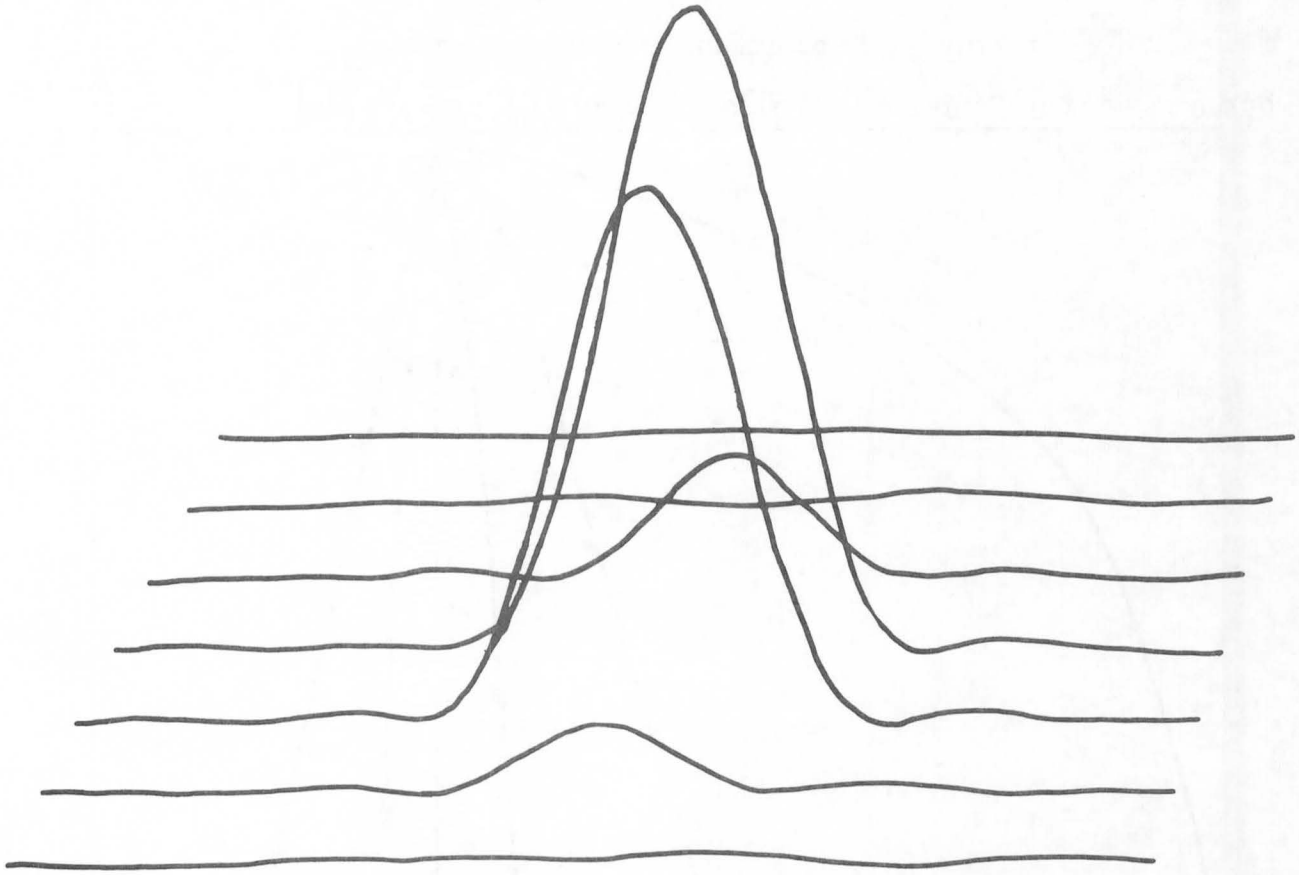


Figure 2-3 Pinhole Image Profile Scans at Best Mirror Alignment with 58 Actuators

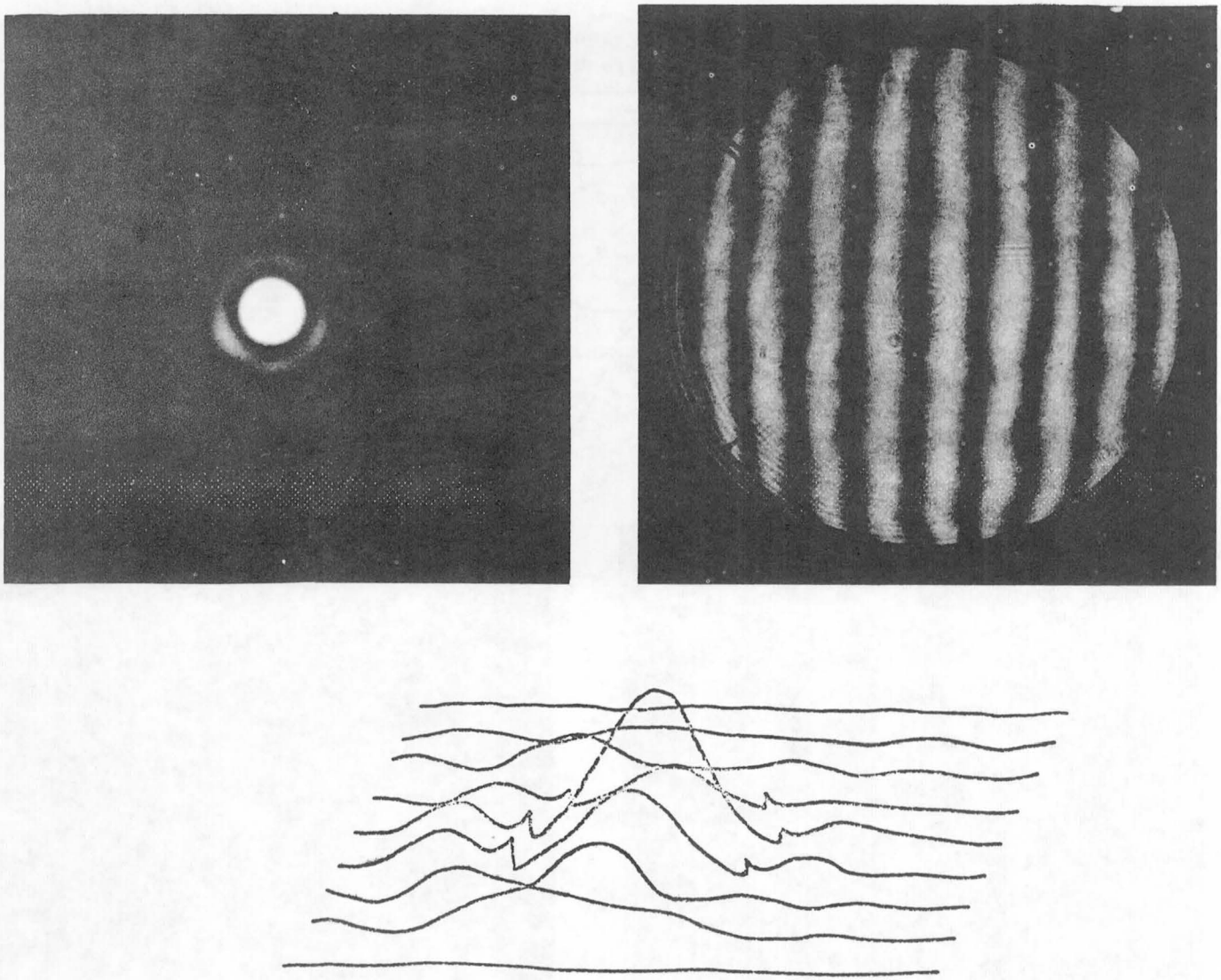


Figure 2-4. Interferogram, Pinhole Image, and Pinhole Image Scans for Best Mirror Alignment with 58 Actuators (Scale in Center 1/10 Scale of Rest of Image Scans)

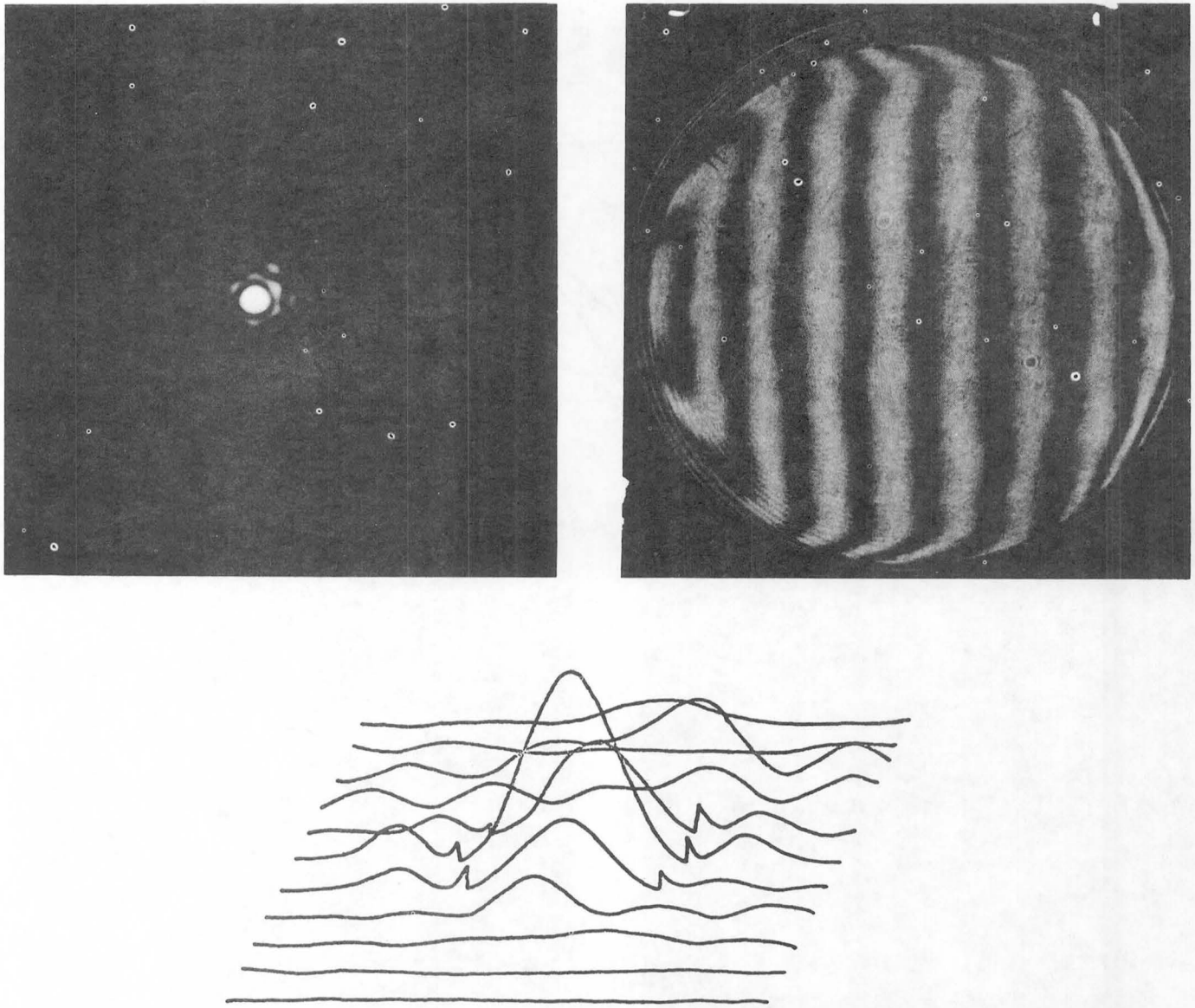
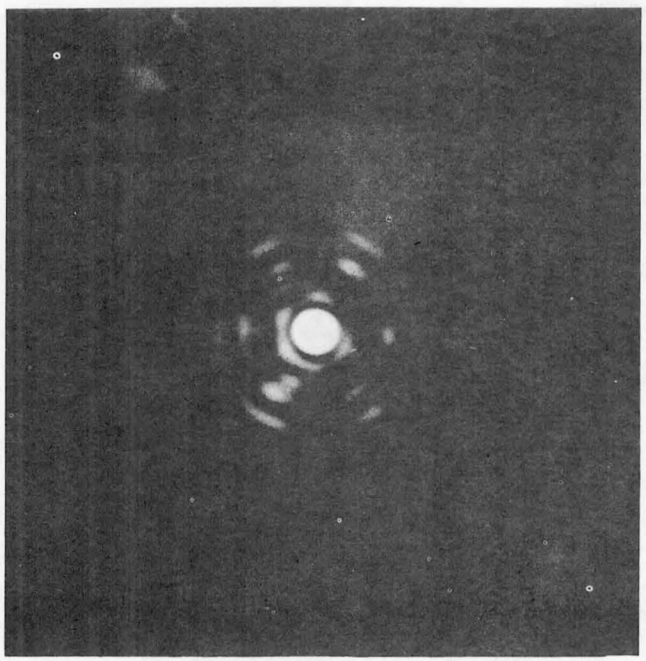
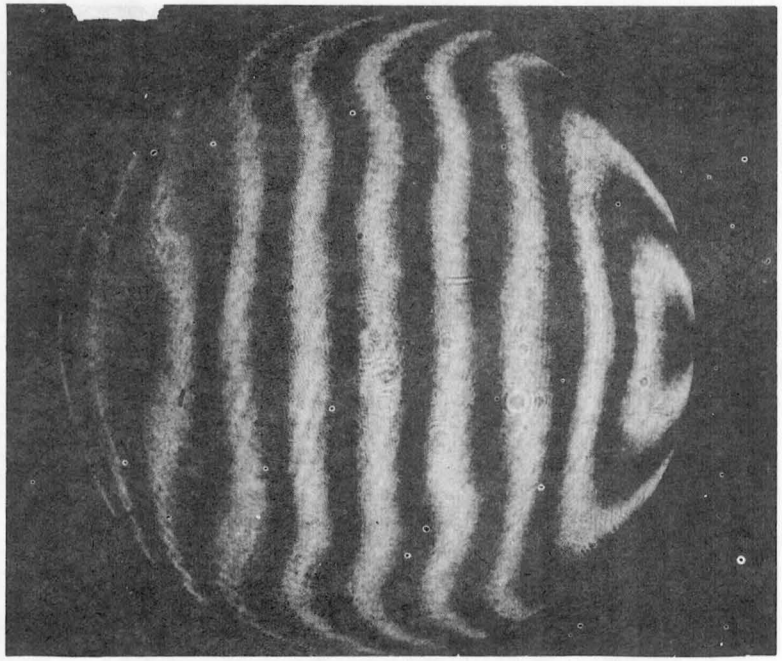


Figure 2-5. Interferogram, Pinhole Image, and Pinhole Image Scans for Mirror Aligned with 58 Actuators, 0.100" from Position of Best Alignment (Scale in Center 1/10 Scale of Rest of Image Scans)





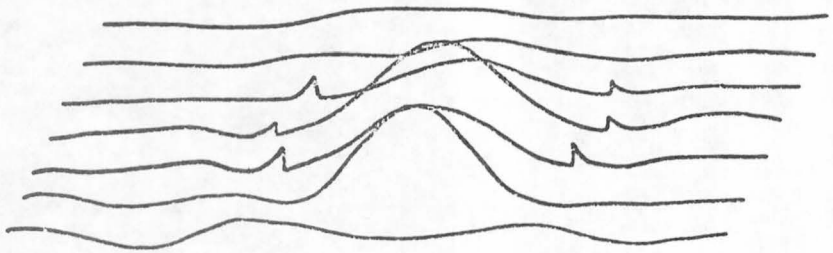


Figure 2-6. Interferogram, Pinhole Image, and Pinhole Image Scans for Mirror Aligned with 58 Actuators, 0.225" from Position of Best Alignment (Scale in Center 1/10 Scale of Rest of Image Scan)

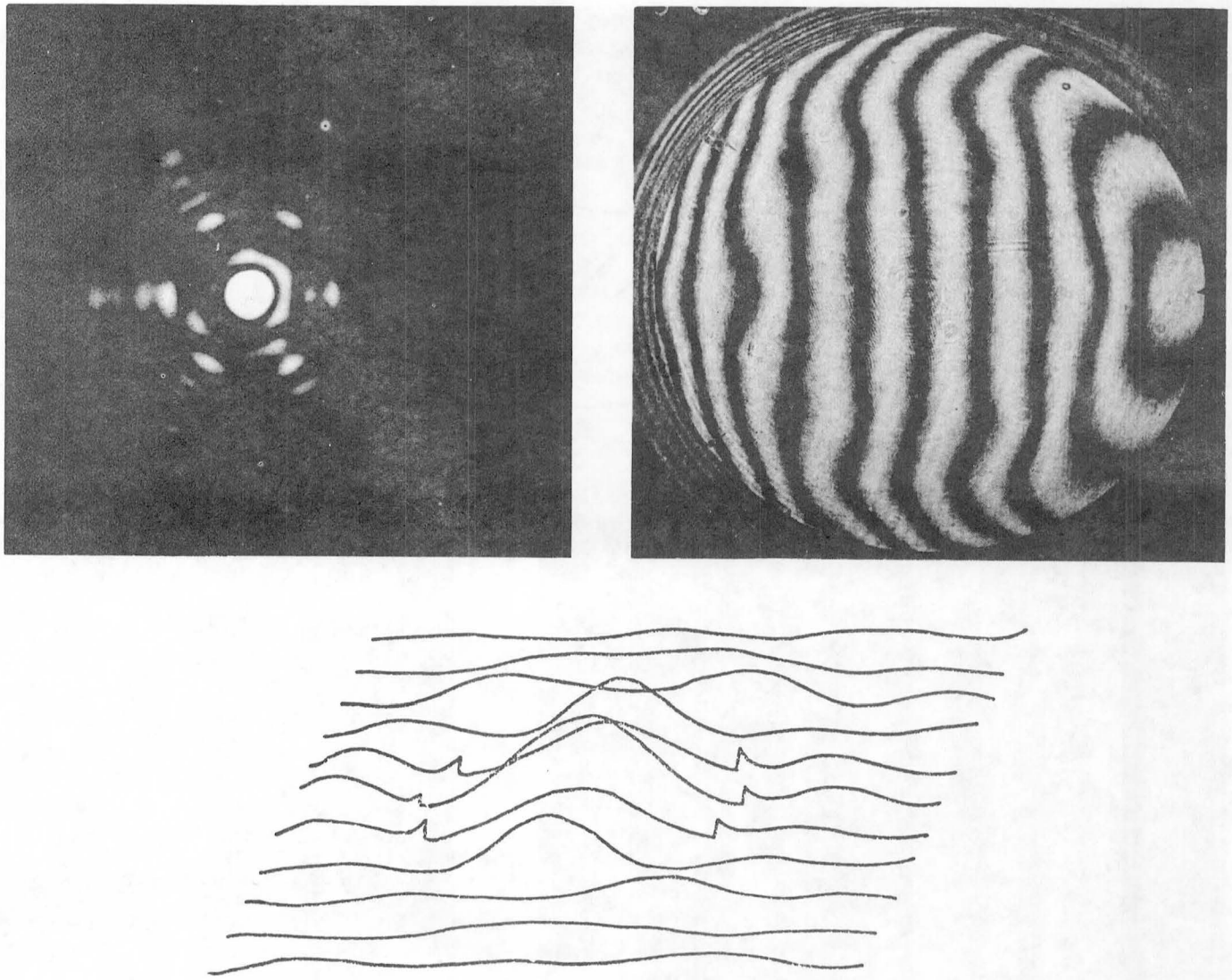


Figure 2-7. Interferogram, Pinhole Image, and Pinhole Image Scans for Mirror Aligned with 16 Actuators, 0.050" from Position of Best Alignment (Scale in Center 1/10 Scale of Rest of Image)

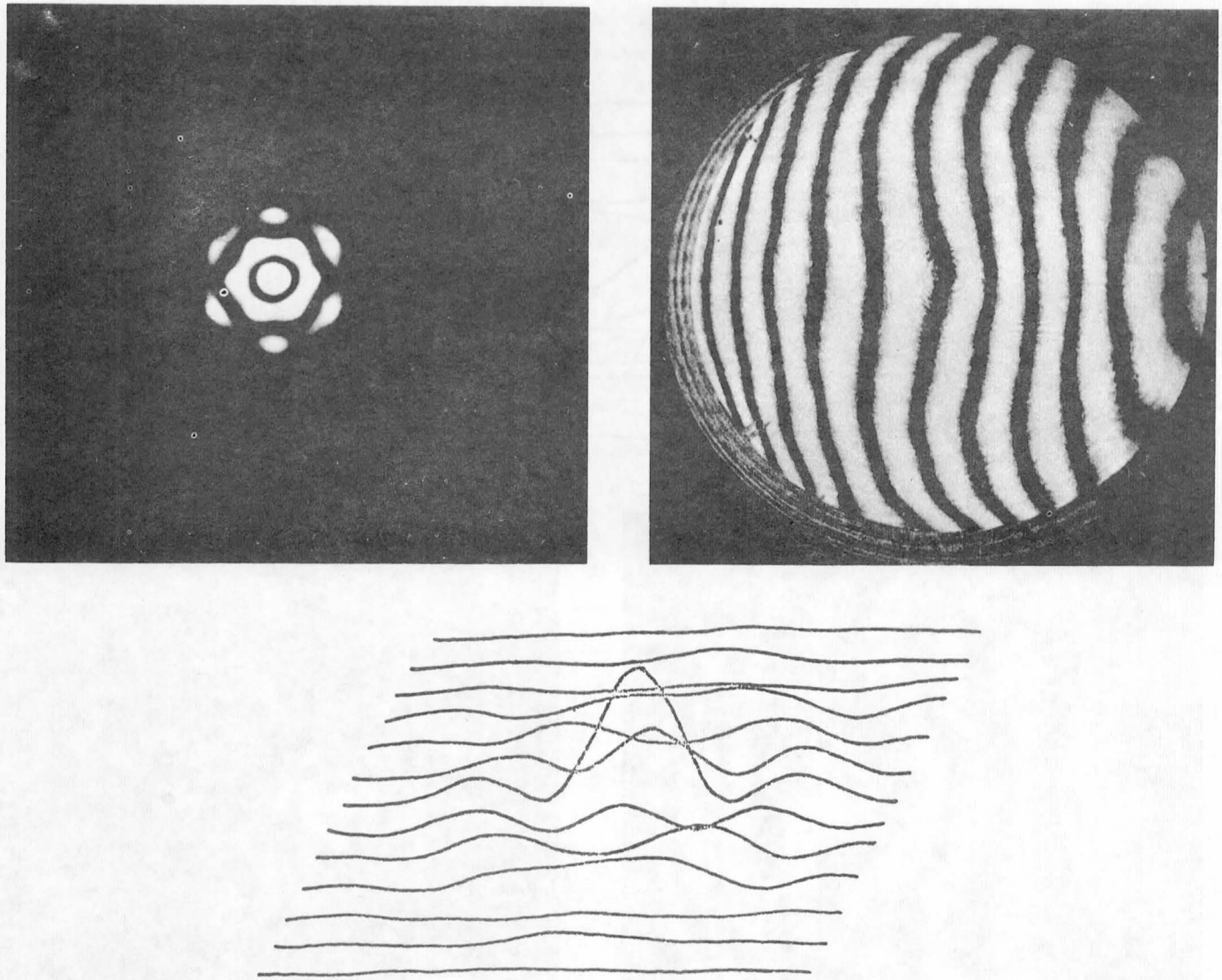


Figure 2-8. Interferogram, Pinhole Image, and Pinhole Image Scans for Mirror Aligned with 4 Actuators, 0.015" from Position of Best Alignment (Scale in Center 1/10 Scale of Rest of Image)

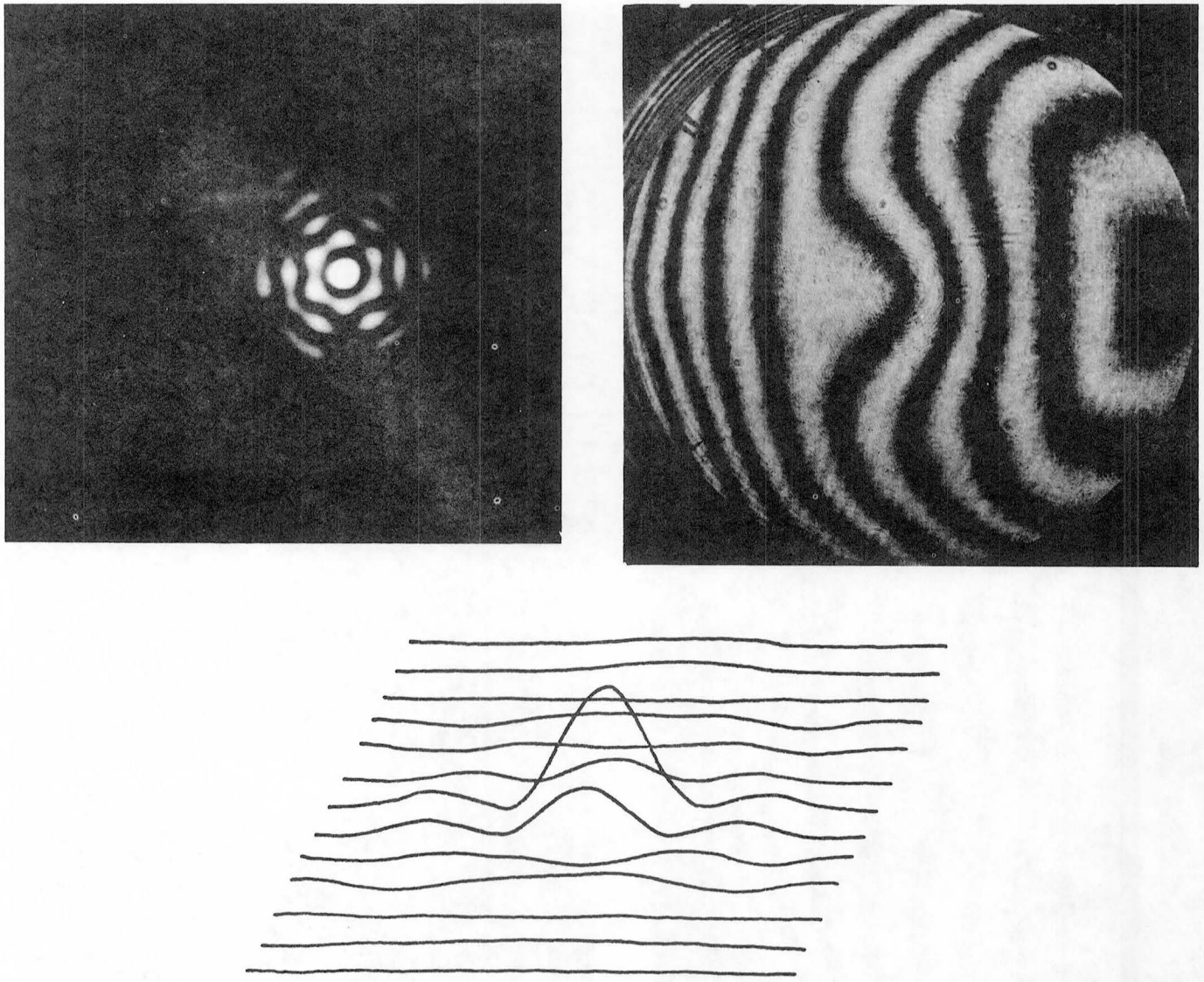


Figure 2-9. Interferogram, Pinhole Image, and Pinhole Image Scans for Mirror Aligned with 4 Actuators, 0.030" from Position of Best Alignment (Scale in Center 1/10 Scale of Rest of Image)

where I_m = maximum intensity at center of image normalized to that of a perfect image

ε_r = rms deformation of mirror surfaces

Thus, changes in the mirror error can be determined rather quickly by monitoring the peak intensity of the point source image. This assumes, however, that the total intensity is also known at all times. For the present scans, the intensity of the source illuminating the pinhole (He-Ne laser) was assumed to be constant although it appears that it did change over long periods of time. For future analysis a means of measuring the total intensity could be added to provide more quantitative information.

3.0 EXPERIMENTAL DETERMINATION OF INFLUENCE COEFFICIENTS

Influence coefficients for the 30-inch thin mirror were previously obtained analytically from a structural analysis program (SAMIS)*. These influence coefficients had never been corroborated experimentally although there was good reason to believe that they were reasonably accurate since a comparison of calculated and measured influence coefficients for a scaled model had shown good agreement. It was now possible, however, to make measurements of the static deflections of the 30-inch-diameter, 1/2-inch-thick mirror including the effects of the mounting structure, the mounting pads, and the other actuators.

The influence coefficients were measured from interferograms of the mirror obtained using the phase measurement interferometer. The mirror was first aligned using the Active Optics closed loop control system. The control system was turned off and then the mirror was stressed by applying a force at one actuator point. The displacement at all points of the mirror with respect to any reference point on the mirror were measured directly from the interferogram, in fringes and fractions of a fringe of the 6328Å light used to obtain the interferogram.

Figure 3-1 shows the interferogram obtained by displacing the center actuator so as to change the force it applies by three pounds with respect to the aligned condition. The interference pattern for the interferogram shown was adjusted to put the three support points in approximately the same phase to facilitate comparison of the mirror deflections with the calculated values, since the calculated values assume that the support points are perfectly rigid and have zero displacement. This is not exactly the case in practice, and the support points actually show some displacement with respect to the reference. Different reaction support arrangements to increase the stiffness at these points have been investigated.

---

*Reference No. 3

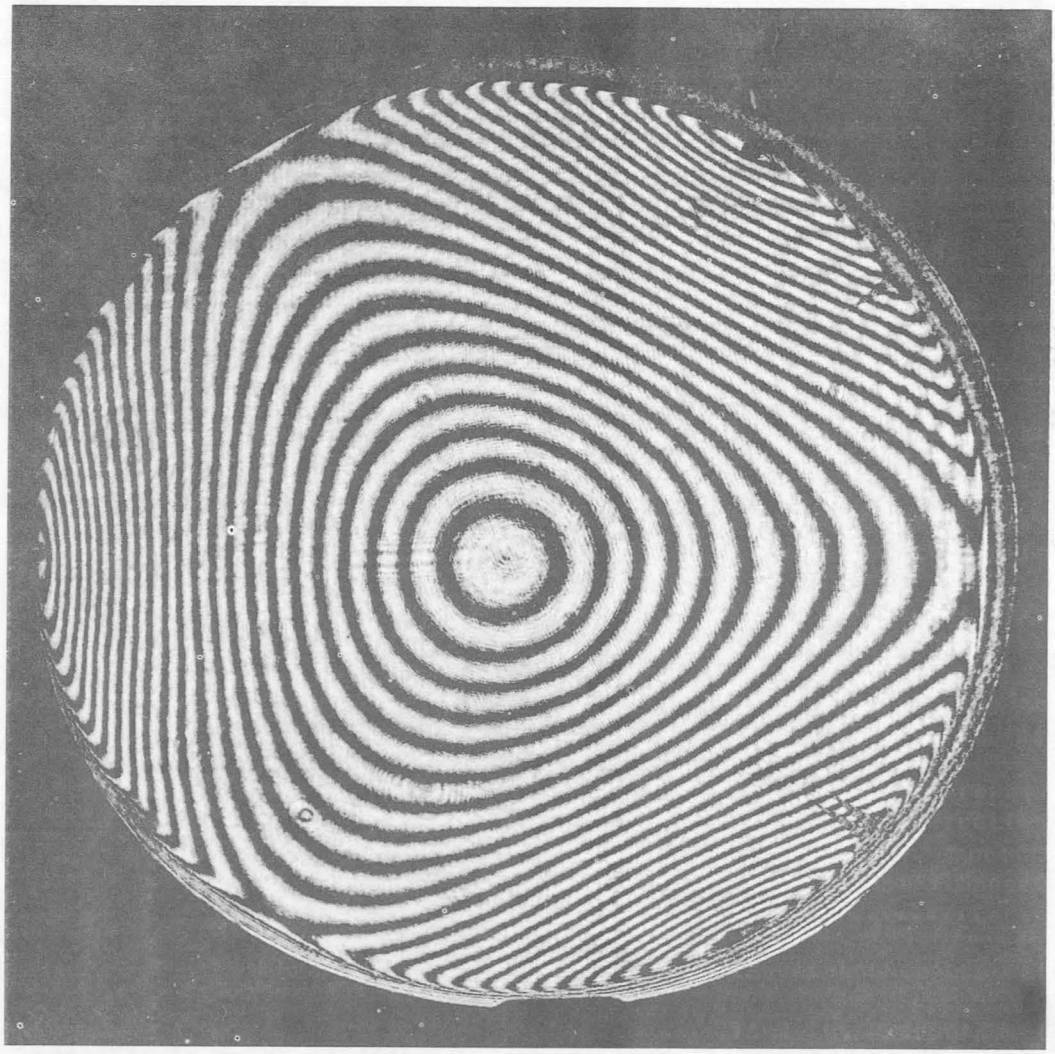


Figure 3-1. Interferogram of Mirror with 3-Pound Force Applied at Center after Alignment

An attempt was made to obtain a measurement of the forces required to obtain local mirror deflections, for comparison with the calculated stiffness coefficient matrix. The mirror was first aligned with the Active Optics closed loop control system. One channel at a time was then opened and the mirror was driven out of alignment at the corresponding actuator while alignment at all other points was maintained. The change in actuator forces should give the forces required to obtain a local displacement and can be determined from the change in displacement of the actuator nuts. A linear potentiometer attached to each actuator provides the actuator nut displacement measurement. A set of forces for a local displacement at one point provides the stiffness coefficients for one column of the stiffness matrix. A set of forces for a local displacement of one fringe at the center point of the mirror is shown in figure 3-2 . It was found, however, that it was very difficult to obtain reproducible results for any one column of the stiffness matrix. This is believed to be due to dead zones in the actuators due to friction and even though the dead zones are equivalent to less than ±1/200 wavelength in their effect on nulling at any one actuator, they still allow for different sets of forces and their corresponding stiffness coefficients. This effect is discussed further in Section 6.0.

Figure 3-1 shows the interferogram for the deflection due to a centrally applied force. Figure 3-3 shows typical interferograms at other locations for an applied force of one pound. Figure 3-4 shows the locations at which the force is being applied in figure 3-3. The actuator numbering code used here is shown in figure 3-5.

The displacement of the mirror measured at all the actuator locations gives the influence coefficients for those locations. The displacement at any particular point is measured with respect to a reference point by counting the number of fringes and fractions of a fringe between it and the reference point. The three mirror support points located at 120-degree intervals around the mirror edge are taken to be in the zero displacement reference plane and the interferometer is aligned in tilt to put these three points as closely as possible

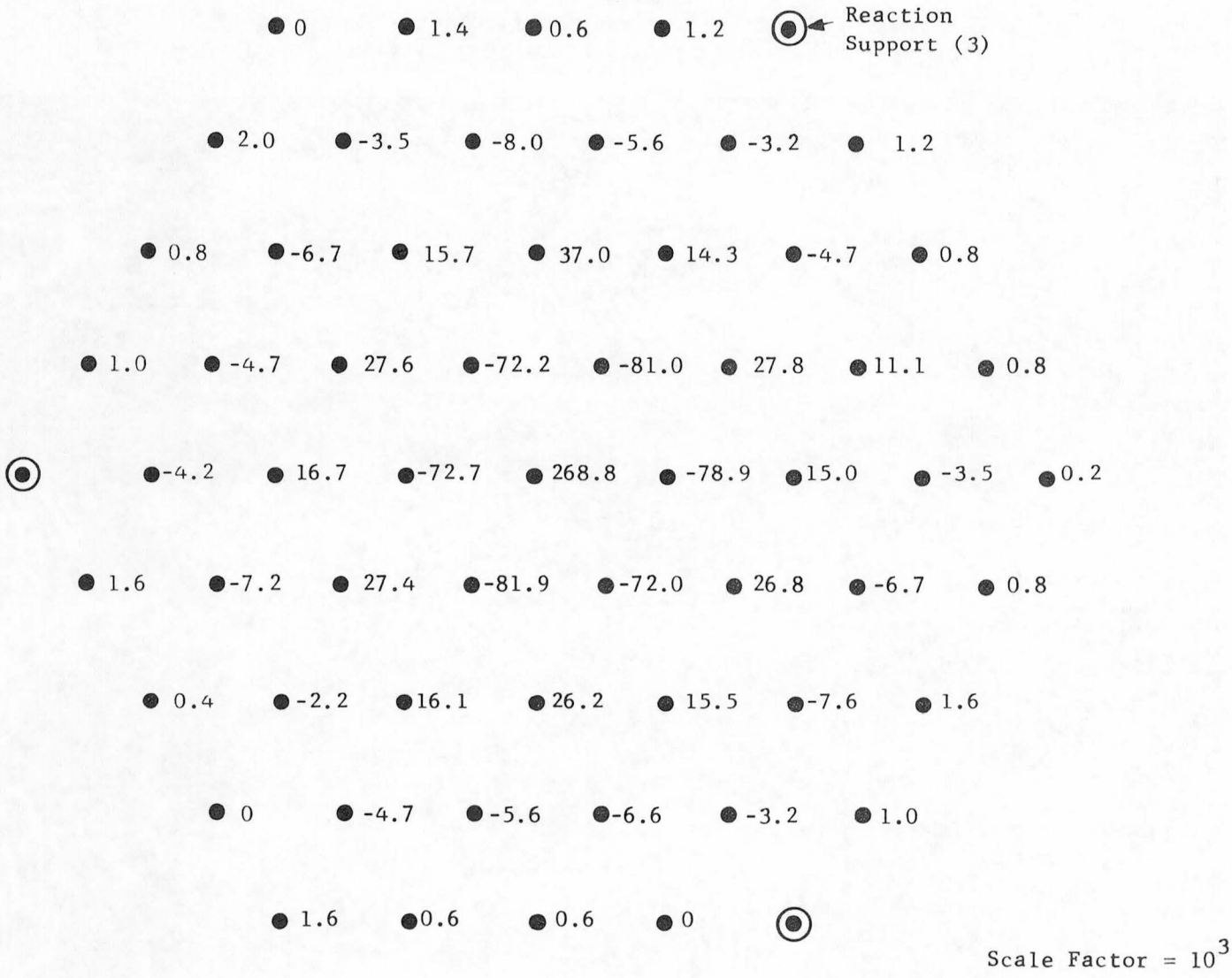


Figure 3-2. Stiffness Coefficients (For Local Displacement at Center of Mirror)

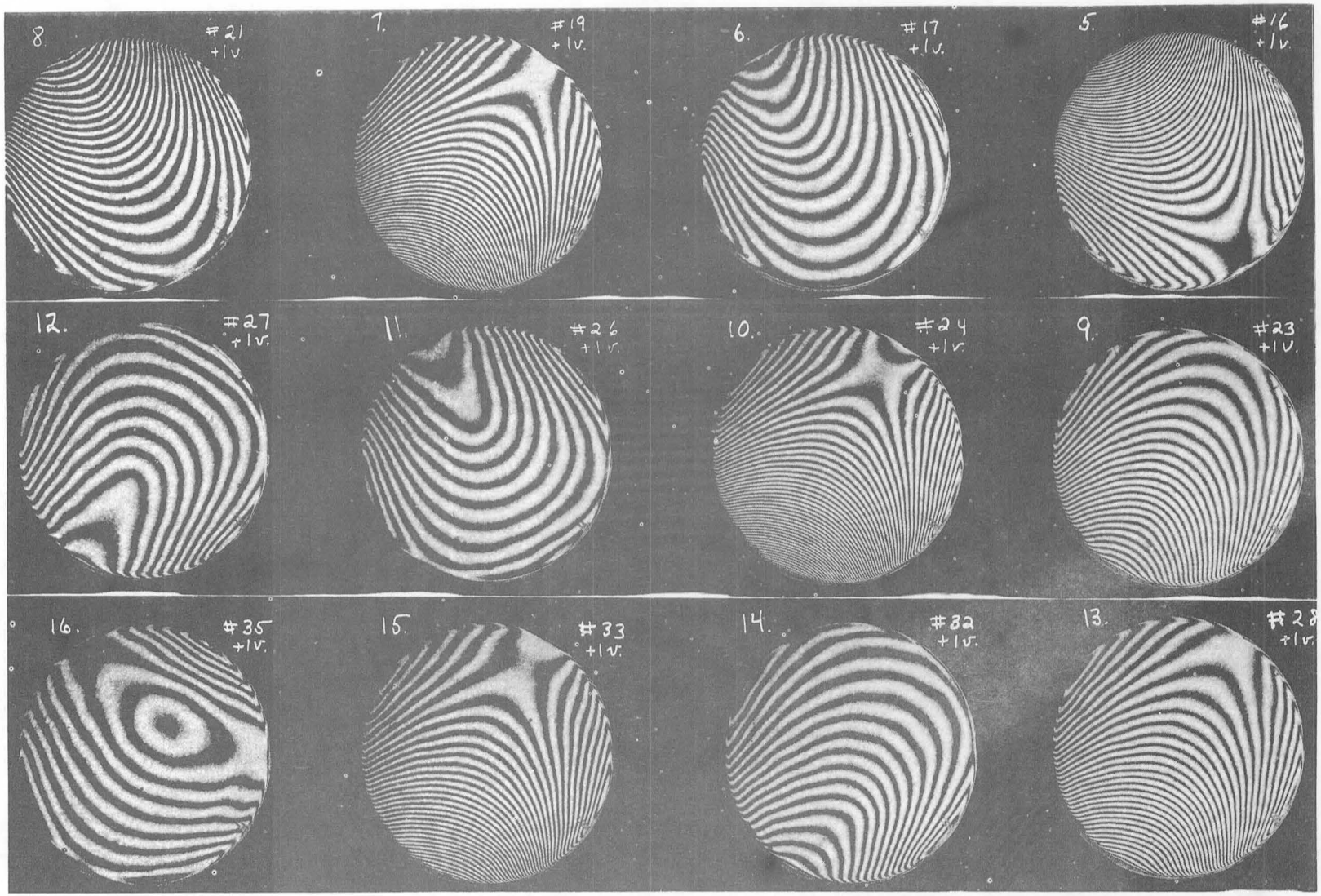


Figure 3-3. Interferograms of Mirror Deformed by One Pound Force at Various Actuator Locations

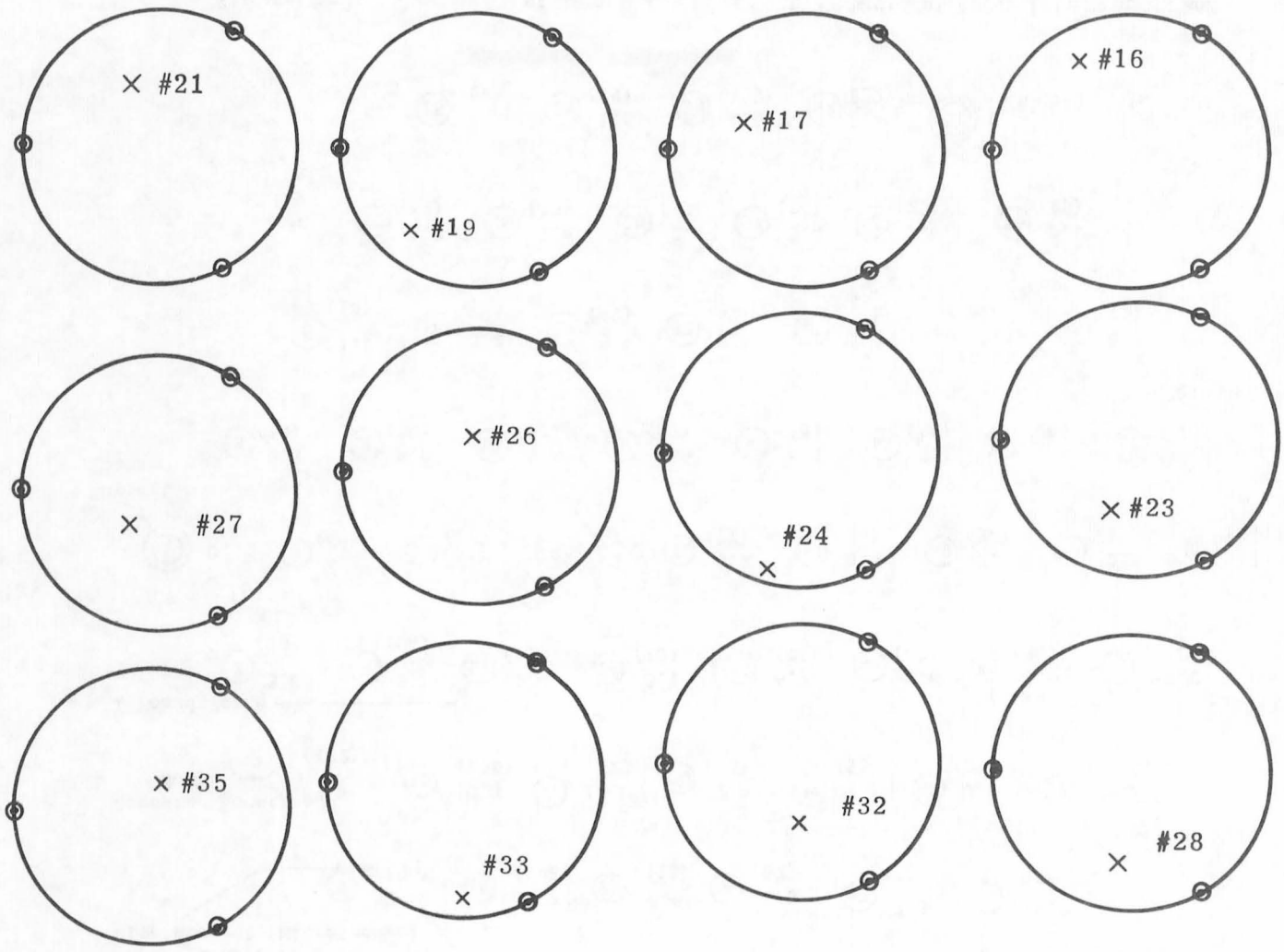


Figure 3-4. Actuator Locations at Which One Pound Force is Applied in Figure 3-3

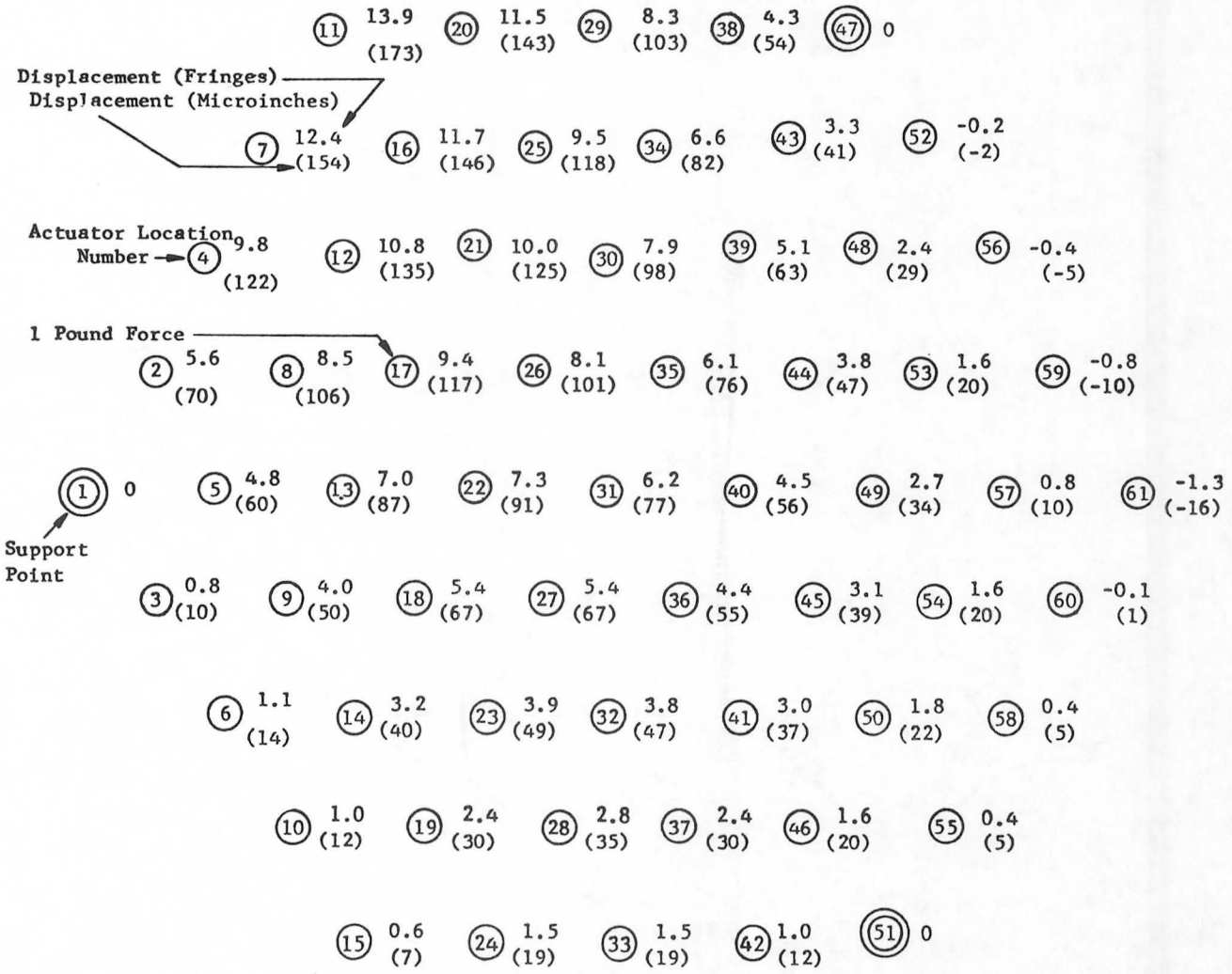


Figure 3-5. Typical Influence Coefficient Reduction from Interferogram

at equal phase in the interferograms. The displacement counted in fringes is converted to microinches by the relation one fringe equals 12.46 microinches. Figure 3-5 is a set of influence coefficients measured for the mirror deformation shown in frame 6 of figure 3-3 for a force applied at point no. 17. The deformations are given in fringes of 6328Å light and in microinches and represent an average of measurements from three interferograms. Further averaging was possible in some instances due to symmetry. The averaging tends to reduce the effect due to errors in the initial alignment and differences in the actuator spring constants. The one-pound force in each case is applied by displacing the actuator spring a specific distance and since all the springs do not have exactly the same spring constant, there was some variation in the actual force applied.

The set of influence coefficients shown in figure 3-5 represents one row of the influence coefficient matrix and from symmetry can represent several other rows of the matrix by appropriate changes of coordinates.

A full set of influence coefficients as required to produce a complete matrix was obtained. Inconsistencies due to differences in the spring constants were compensated for, after measurement of the spring constants, in the final matrix rows which are shown in Figures 3-6 (a) through 3-6 (n). There are only 14 nonredundant rows, and the actuator locations (according to the numbering arrangement shown in figure 5-5) to which each of the rows applies is given in the title of each figure. The number of the actuator at which the force is applied gives the first subscript for the influence coefficients in the matrix row. The number of the actuator location at which the mirror deflection is observed gives the second subscript identifying the influence coefficient column.

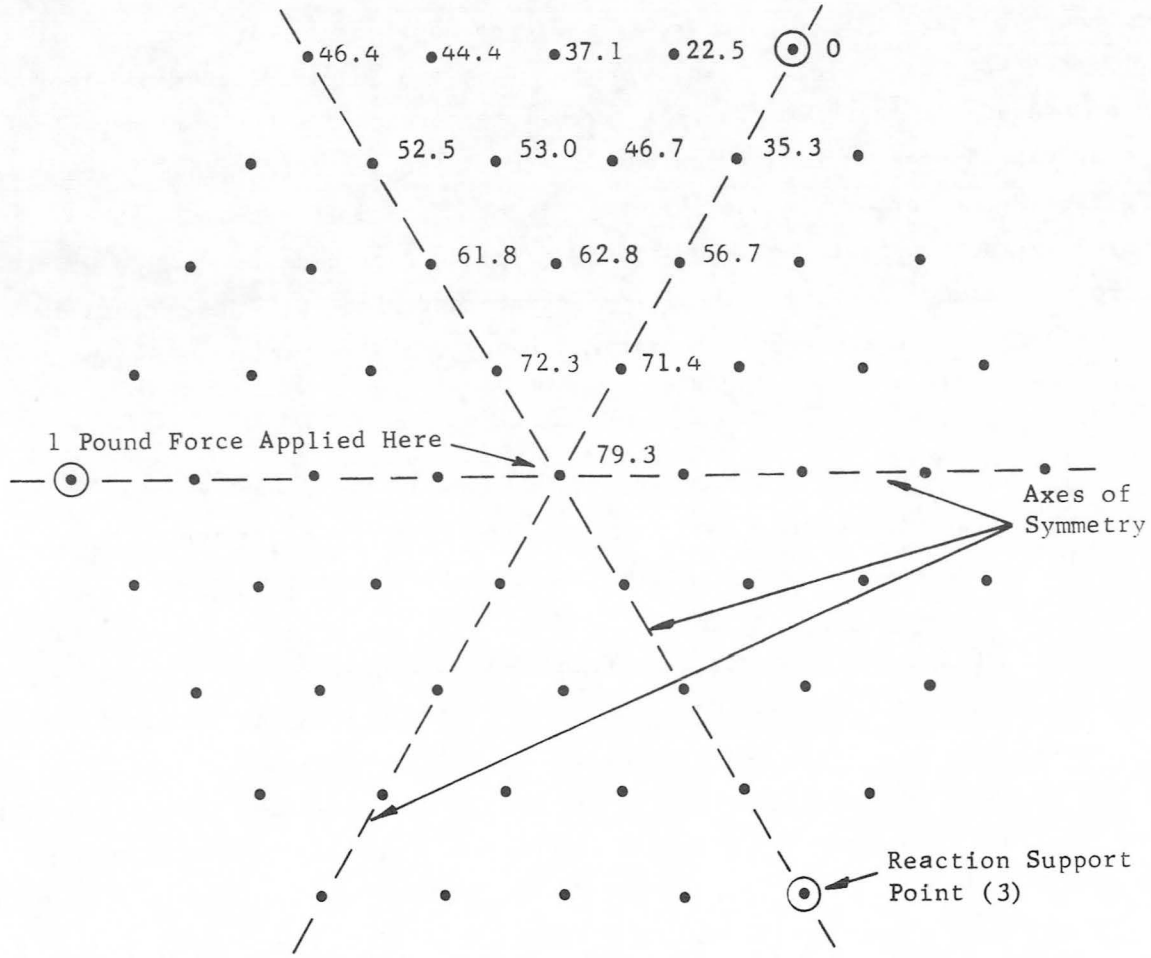


Figure 3-6(a). Measured Influence Coefficients (Microinches Per Pound) For Force Applied at Actuator #20 (Per # Arr. Shown in Figure 5-5)

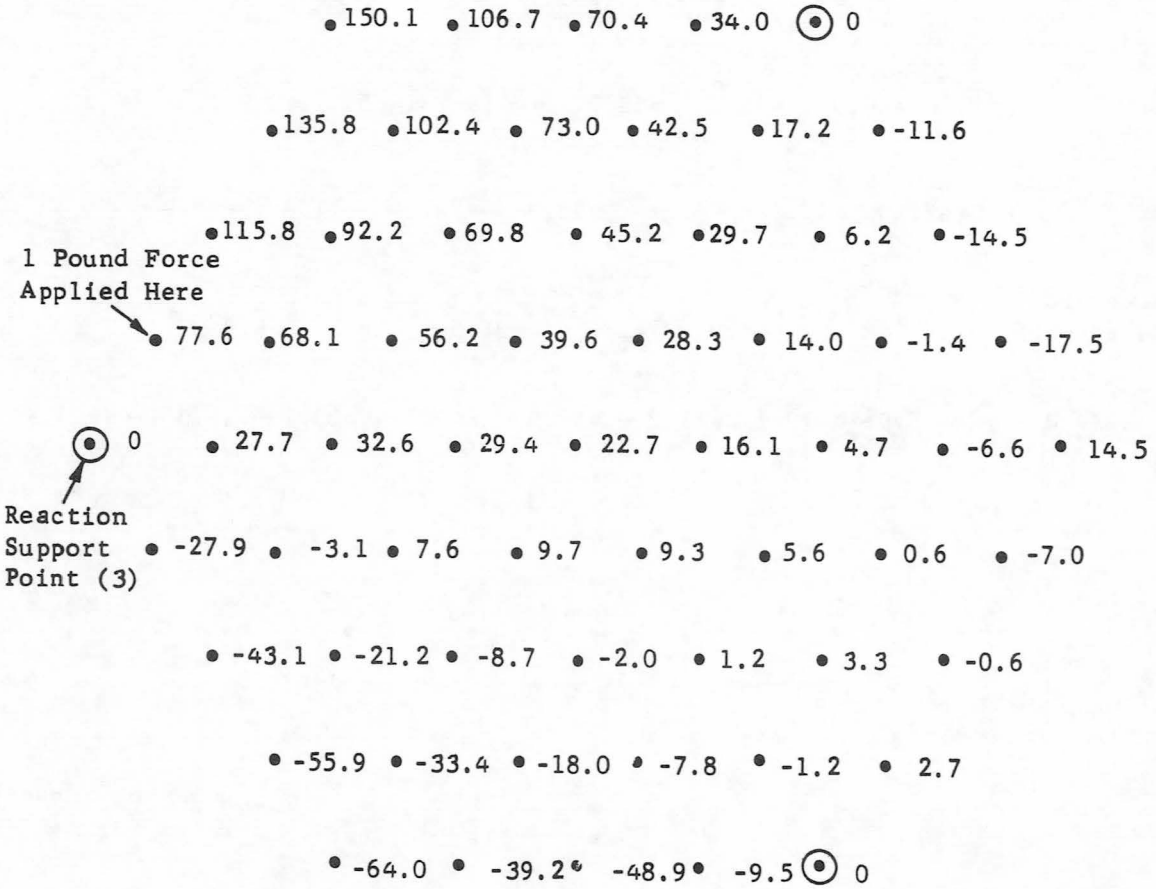


Figure 3-6(b). Measured Influence Coefficients (Microinches Per Pound) For Force Applied at Actuator #1, 3, 43, 51, 52, or 58

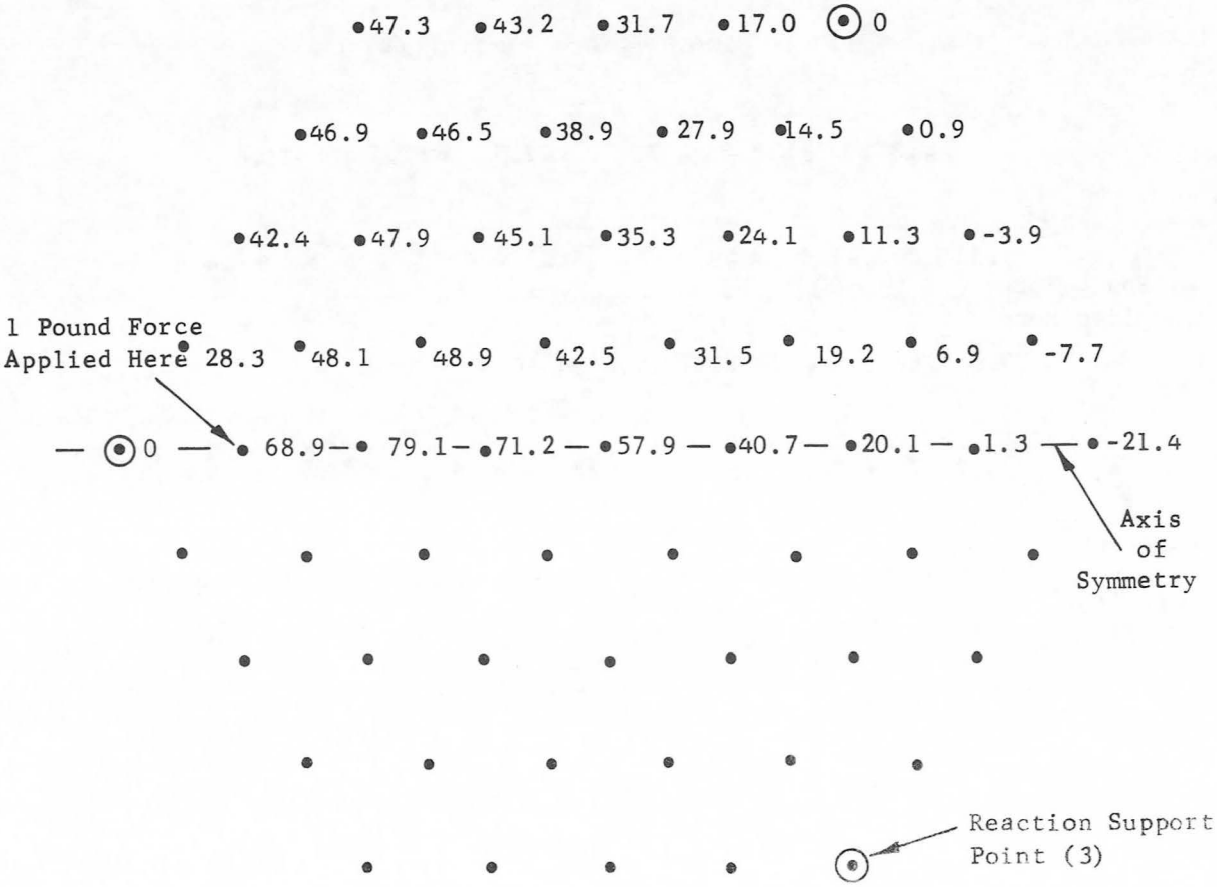


Figure 3-6(c). Measured Influence Coefficients (Microinches Per Pound) for Force Applied at Actuator 2, 44, or 50

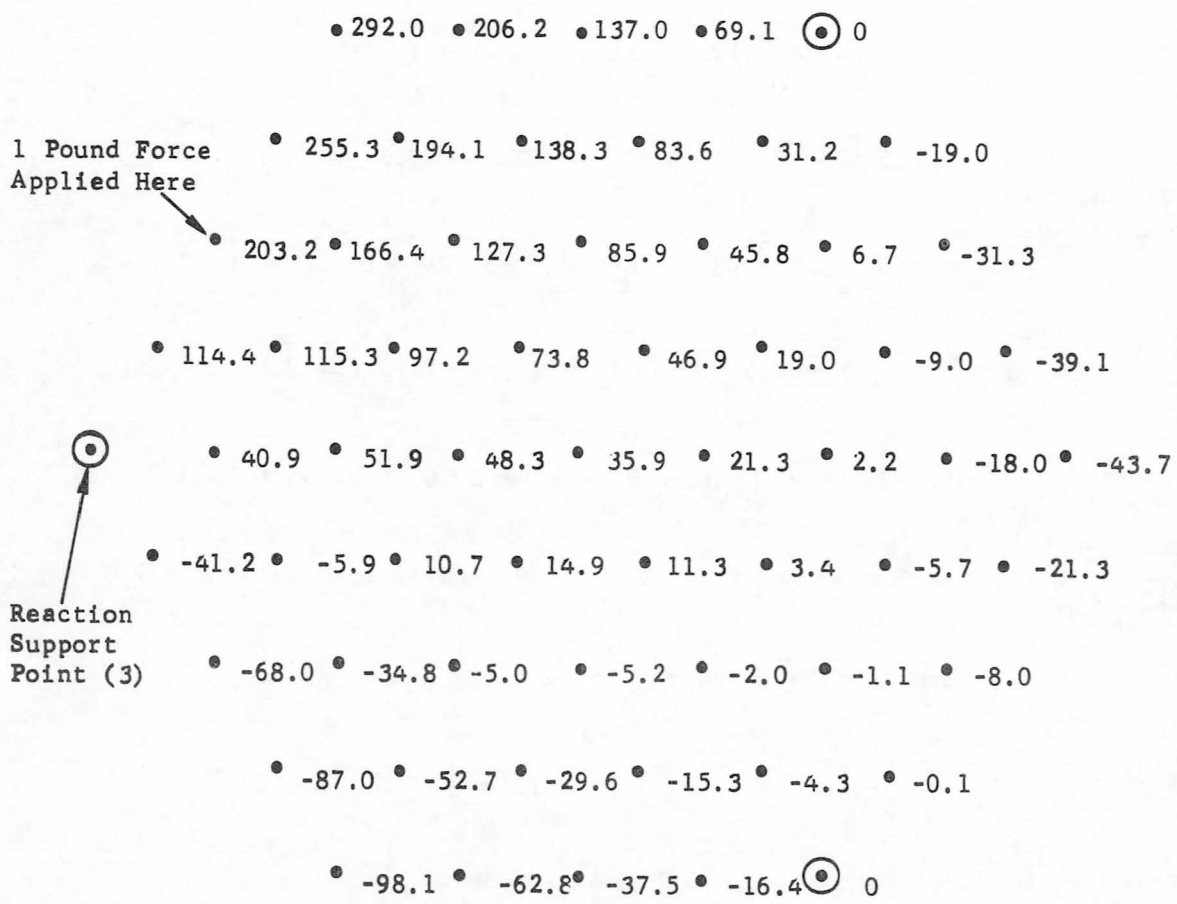


Figure 3-6(d). Measured Influence Coefficients (Microinches Per Pound) for Force Applied at Actuator 4, 8, 34, 38, 53, or 57

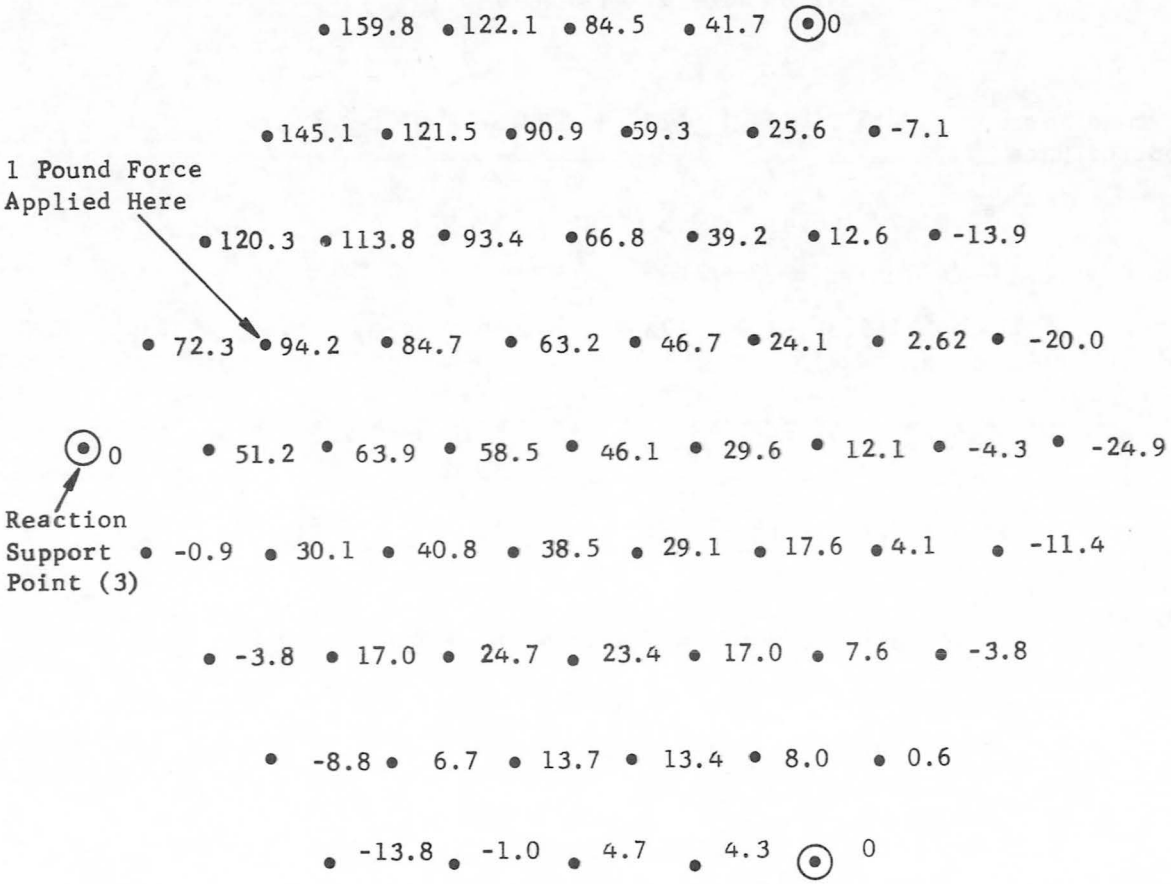


Figure 3-6(e). Measured Influence Coefficients (Microinches Per Pound) for Force Applied at Actuator 5, 7, 36, 42, 45, or 49

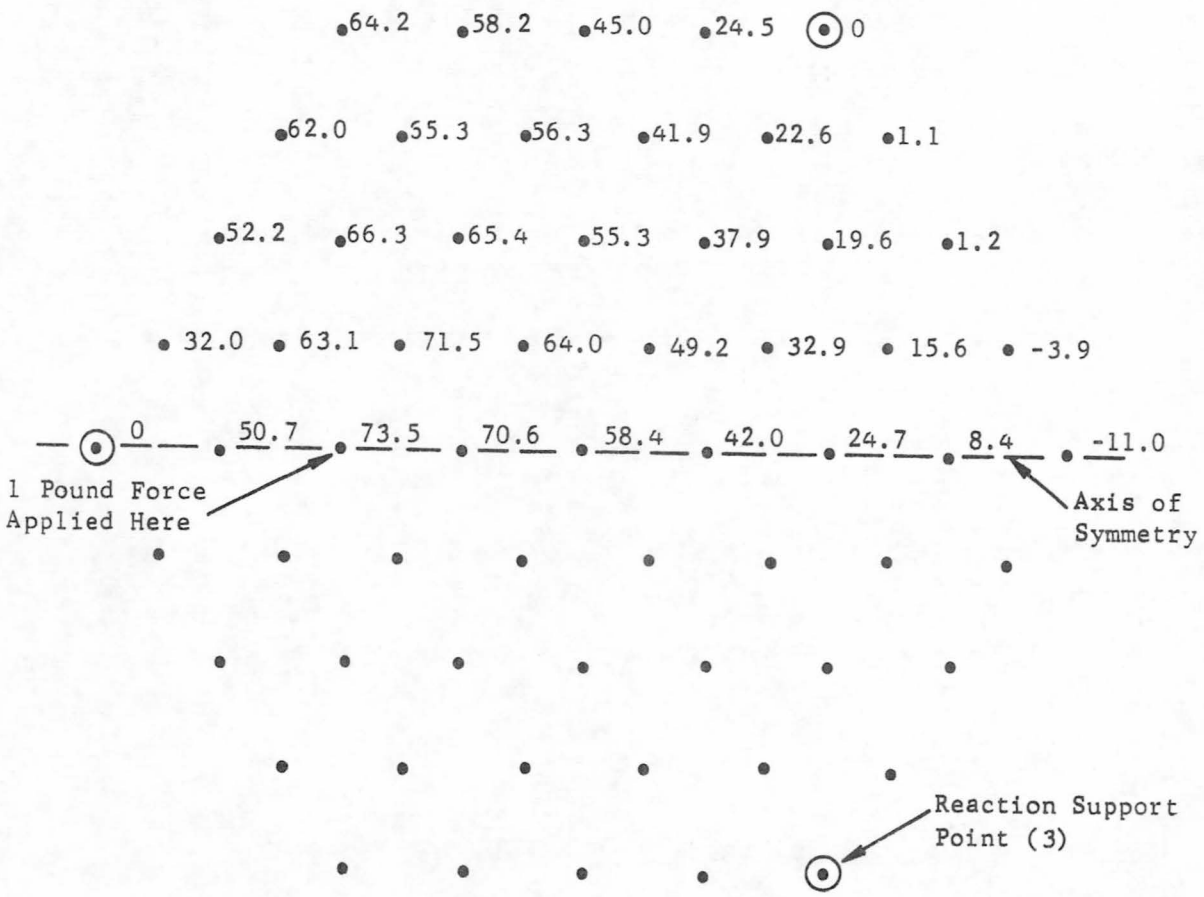


Figure 3-6(f). Measured Influence Coefficient (Microinches Per Pound) for Force Applied at Actuator 6, 37, or 41

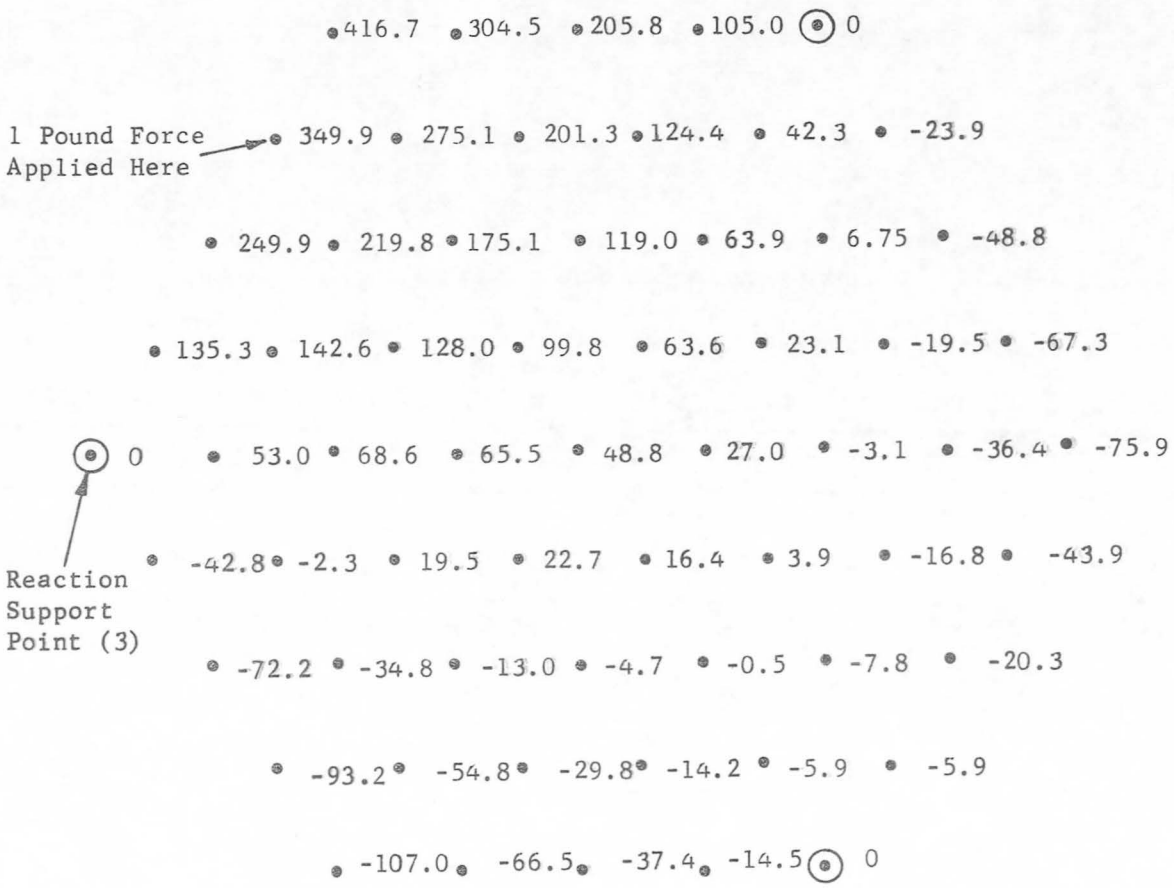


Figure 3-6(g). Measured Influence Coefficients (Microinches Per Pound) for Force Applied at Actuator 9, 15, 25, 33, 54, or 56

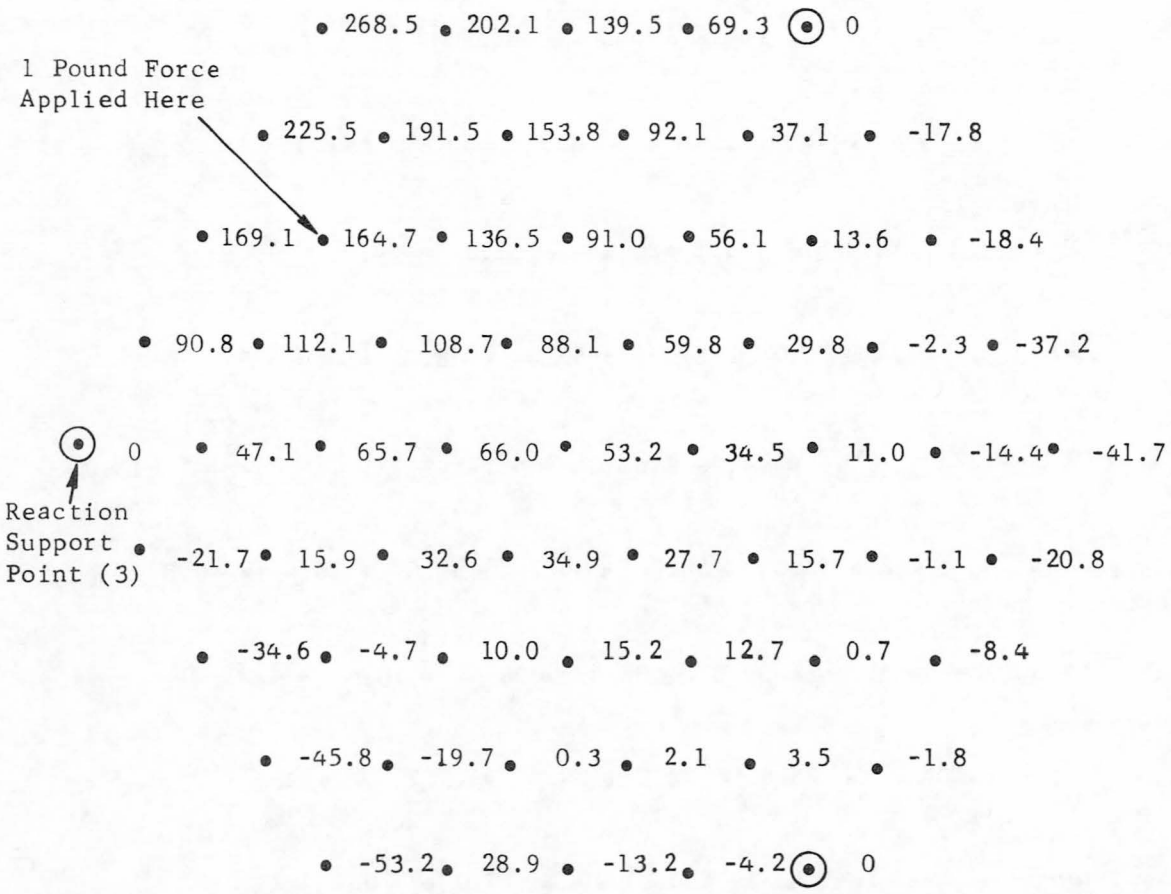


Figure 3-6(h). Measured Influence Coefficients (Microinches Per Pound) for Force Applied at Actuator 10, 14, 26, 32, 46, or 48

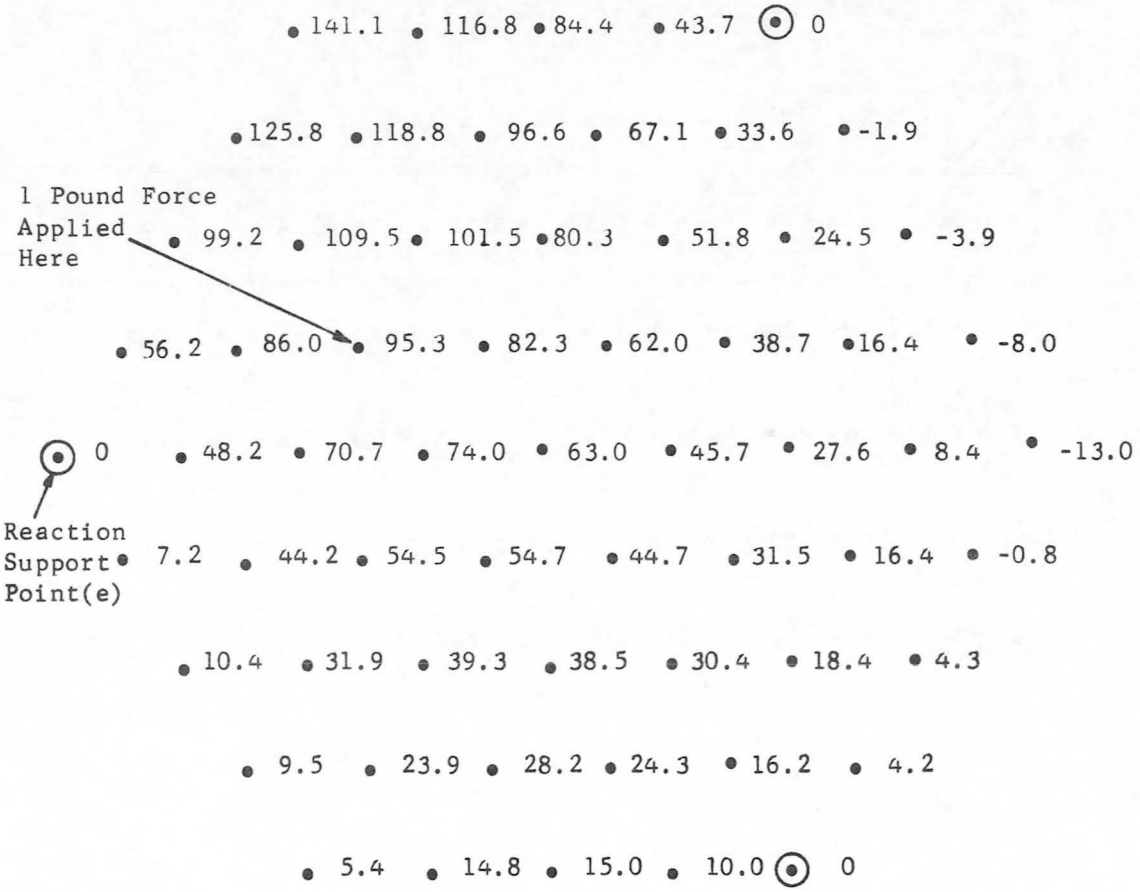


Figure 3-6(i). Measured Influence Coefficients (Microinches Per Pound) for Force Applied at Actuator 11, 13, 27, 31, 35, or 40

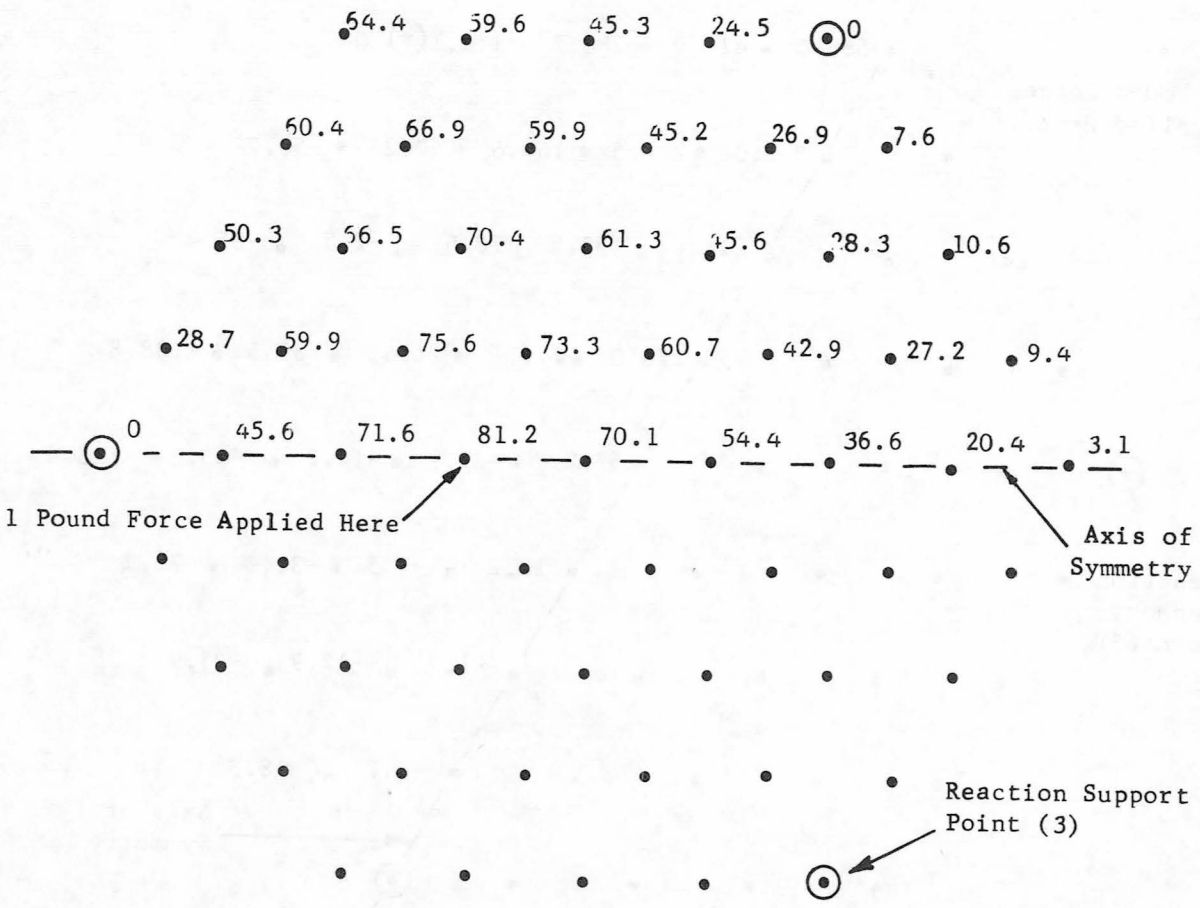


Figure 3-6(j). Measured Influence Coefficients (Microinches Per Pound) for Force Applied at Actuators 12, 28, or 30

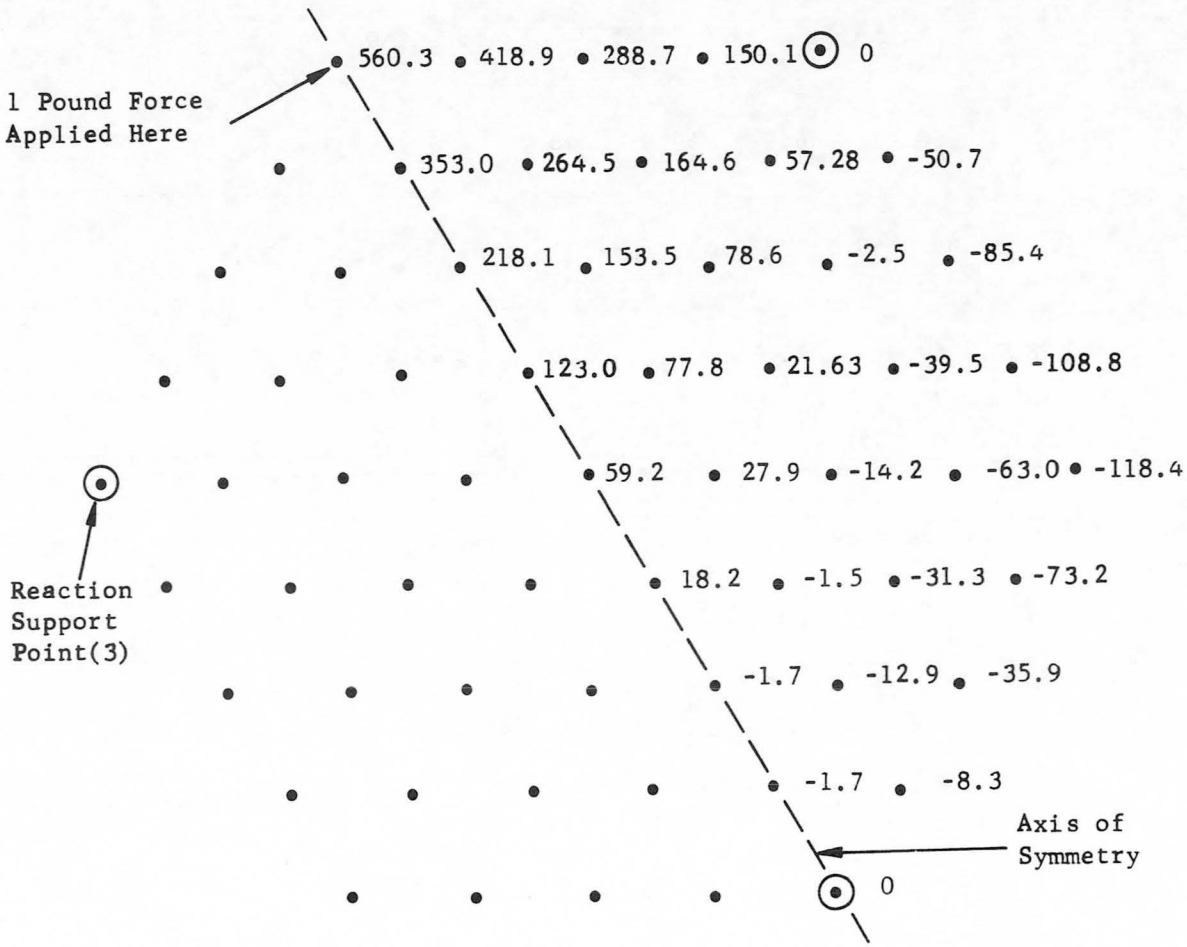


Figure 3-6(k). Measured Influence Coefficients (Microinches Per Pound) for Force Applied at Actuator 16, 24, or 55

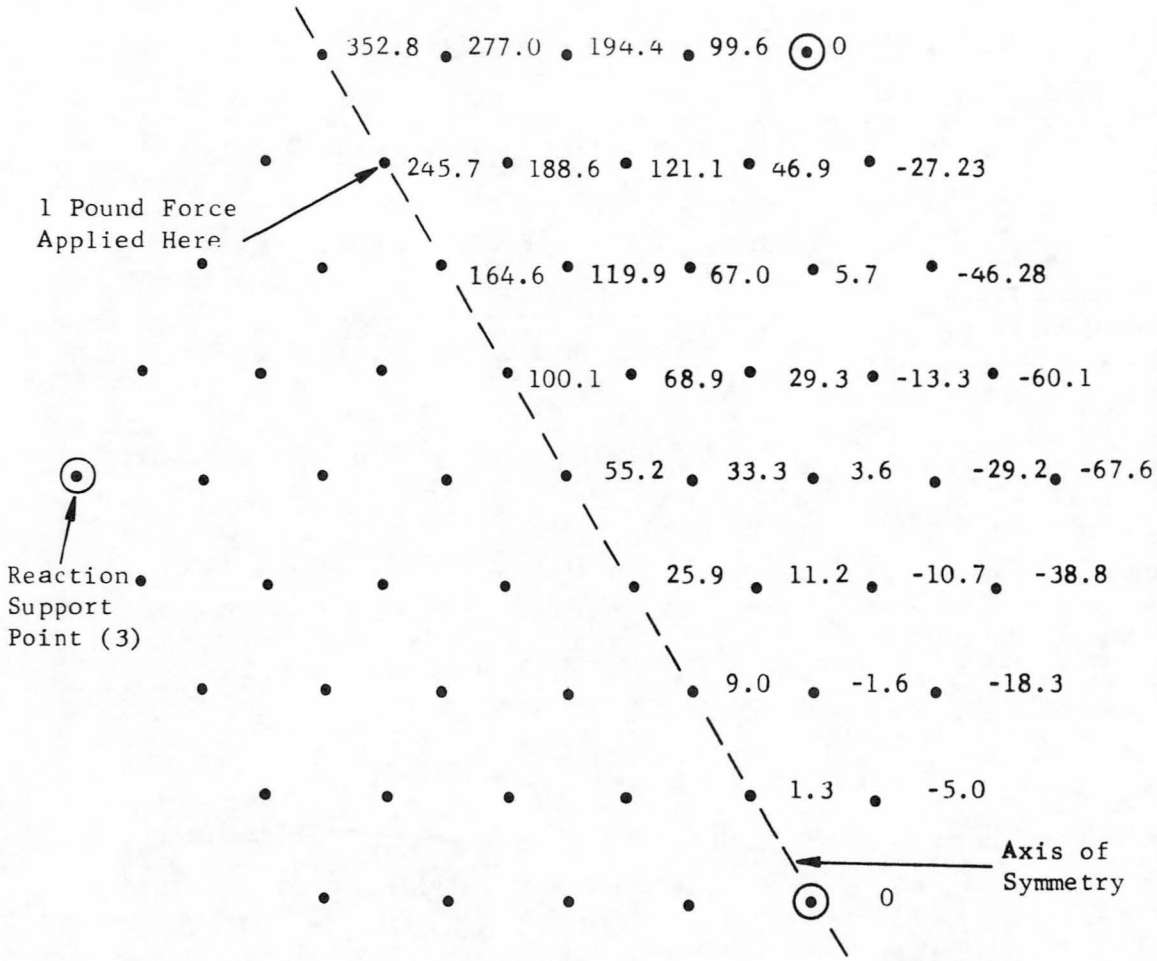


Figure 3-6(1). Measured Influence Coefficients (Microinches Per Pound) for Force Applied at Actuator 17, 23, or 47

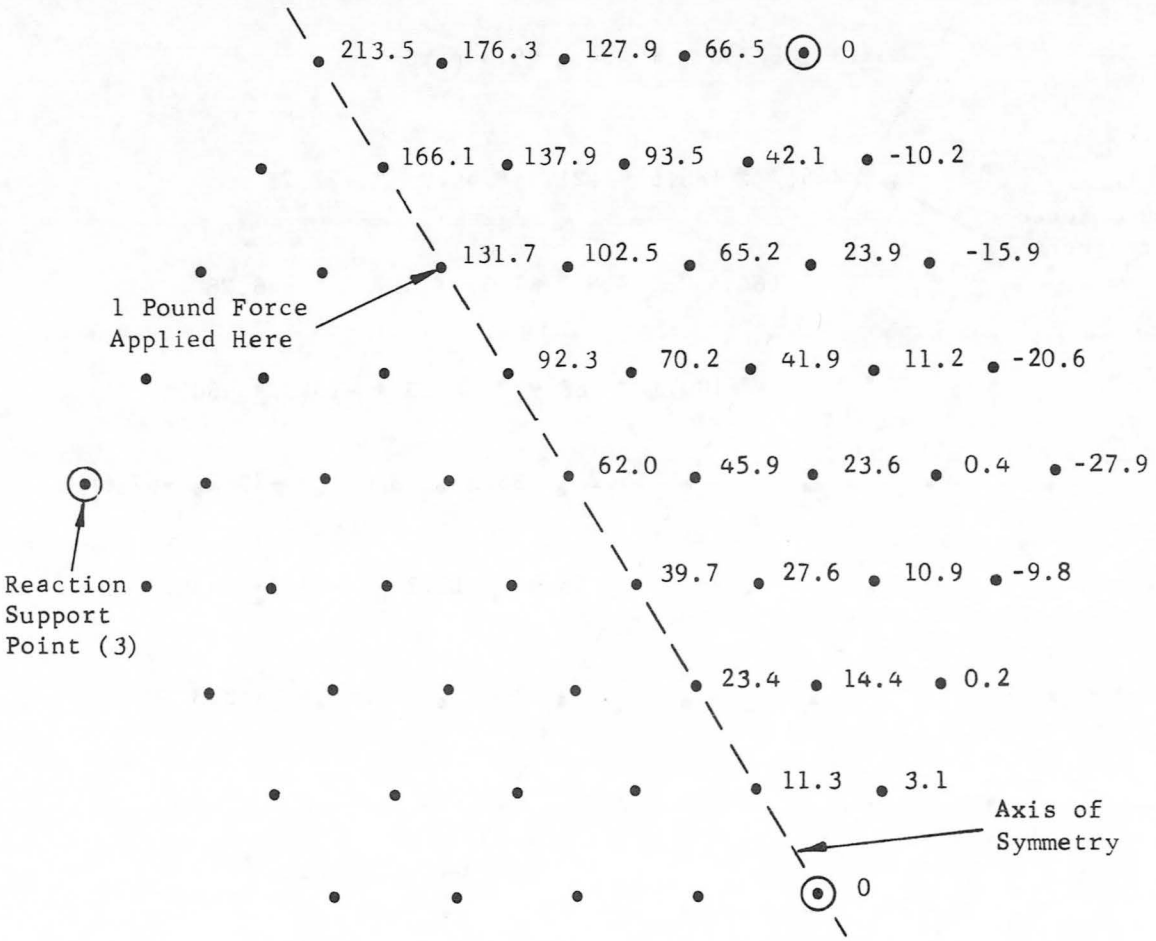


Figure 3-6(m). Measured Influence Coefficients (Micrometers Per Pound) for Force Applied to Actuator 18, 22, or 39

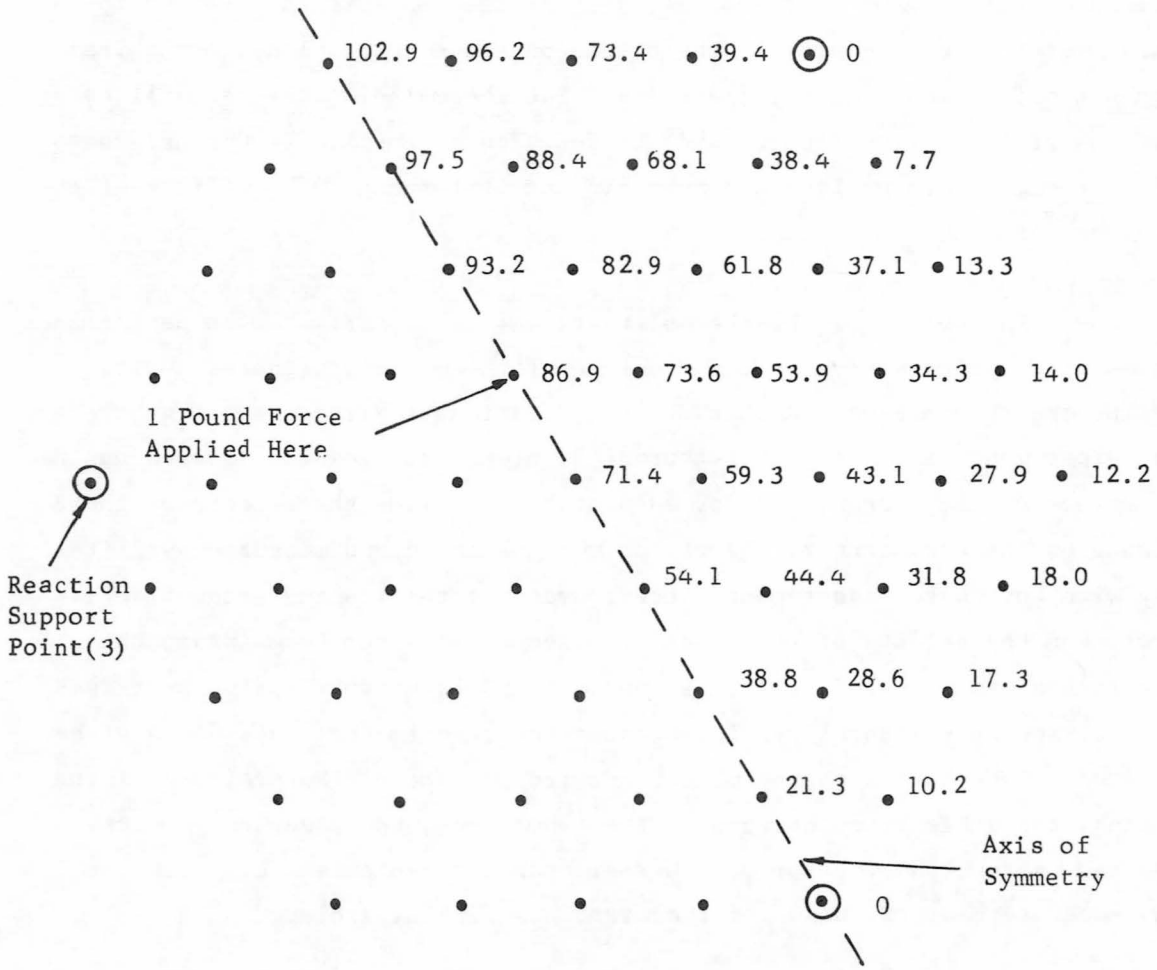


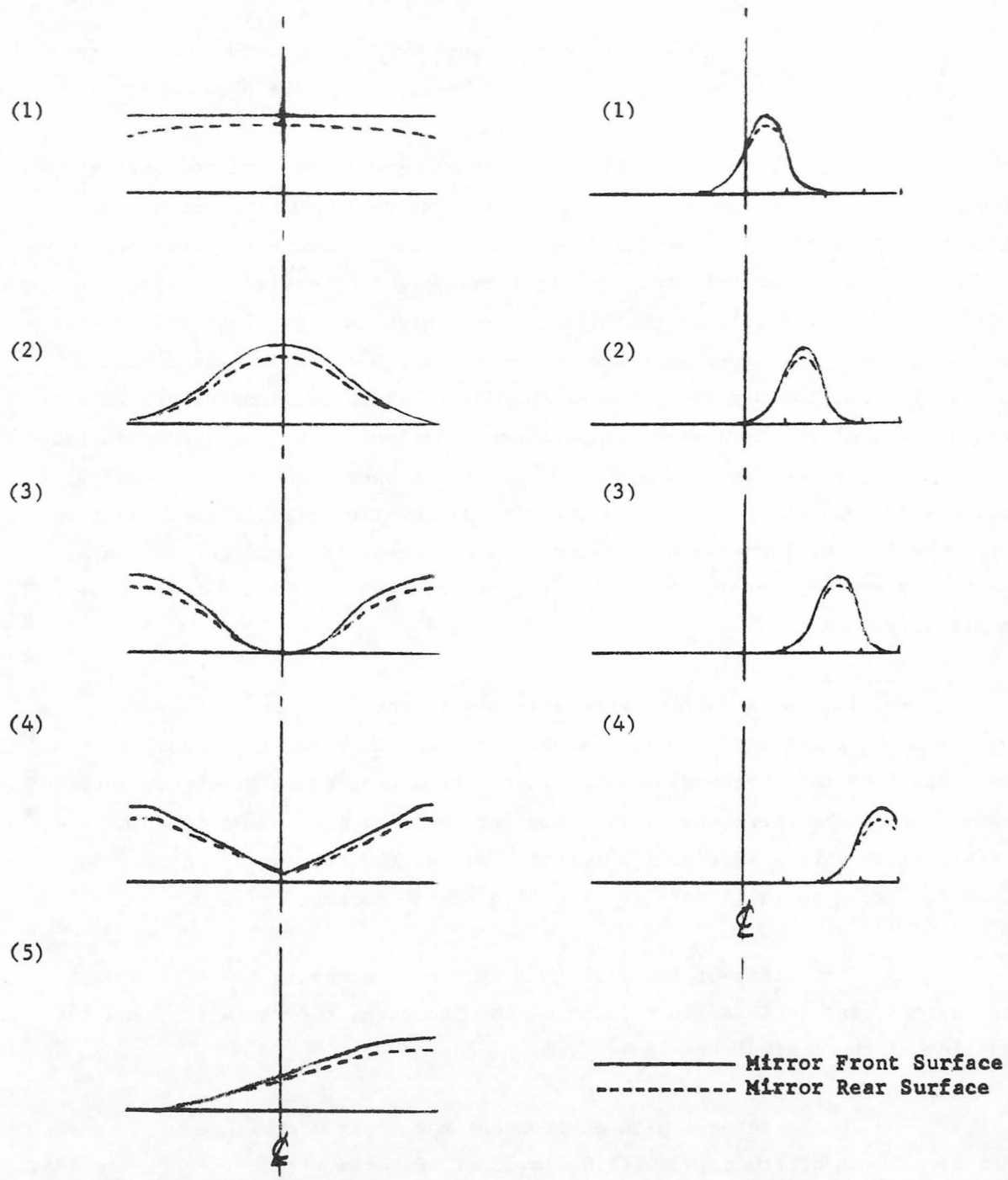
Figure 3-6(n). Measured Influence Coefficients (Microinches Per Pound) for Force Applied at Actuators 19, 21, or 29

4.0 THERMAL MEASUREMENTS

The Active Optics system in space will be subject to thermal disturbances due to many heat sources, such as the sun's irradiation on the primary mirror or on the side of the telescope, and electrical and mechanical components being heated during operation. The thermal disturbances will cause distortion of the mirror figure, and the function of the Active Optics system is to correct for distortions and maintain the performance of the diffraction-limited optics.

The object of the thermal tests was to investigate the performance of the Active Optics system in the presence of thermal disturbances and to determine the response of the thin mirror to various applied thermal gradients. In the experiment, a given set of thermal gradient profiles was imposed on the back surface of the mirror, and for each of the profiles the effects of these gradients on the curvature of the mirror were observed and measured quantitatively with the phase measurement interferometer both with and without active control, and the ability of the closed loop control system to maintain the mirror figure was assessed. In this approach the laboratory environment does not affect the experimental results because the experimental data for a given temperature distribution on the mirror are independent of the pressure of the test tank, the ambient temperature of the laboratory, the size and geometry of the test setup, and the various thermal transfer mechanisms by which the given temperature distribution on the mirror is finally achieved.

The set of thermal gradient profiles that were to be imposed on the mirror consisted of simple and basic profiles such as a constant or linear or radial gradient, as shown in figure 4-1(a), and localized thermal gradients produced by heat applied at small areas on the back of the mirror as shown in figure 4-1(b). It was assumed that most arbitrary thermal distributions can be considered as linear combinations of these basic profiles and that the resulting mirror deformation is the sum of the deformations due to the basic thermal profiles. In practice, the distributed thermal profiles shown in



(a) Distributed Temperature Gradients (b) Local Temperature Gradients

Figure 4-1. Projected Thermal Profiles

figure 4-1(a) were difficult to obtain as uniformly as desired so that some smoothing was required by averaging measurements around the axes of symmetry.

The design of the heating blanket used to produce the desired thermal gradients is shown in figure 4-2 and the design of the guard heater is shown in figure 4-3. The guard heater is located around the edge of the mirror to maintain distributed gradients that might otherwise be difficult to obtain because of heat loss to the test tank which is very close and is essentially a room temperature heat sink. The heating blanket and guard heater consist of many independently heated regions in which the temperature is controlled to achieve the desired temperature distribution on the mirror surface. The heating pads are several layers of silicon rubber that enclose heating elements in separate regions, and the nominal power dissipation is 1 watt per square inch. The temperature measurements were made by 5 mil cu/constantan thermocouples and thermistors, achieving an accuracy of 0.1°C differential temperature.

The thermocouples were attached to the front and back surfaces of the mirror by a patch of pressure sensitive aluminum tape which equalizes the temperature of the surrounding area of the thermocouple to the mirror surface temperature. The thermocouple readings were made by a Leeds-Northrop K-5 potentiometer with a melting ice thermal bath as the reference. A test panel was constructed to facilitate the sampling of the thermocouples.

Some items of interest that were considered in connection with the thermal test include the effects of the pressure, the radiation, and the profiles of the thermal gradient.

In the actual space environment the maximum pressure will be 10^{-6} torr for 150-Km altitude and will be lower at higher altitude (see figure 4-4). The effect of the presence of higher pressure near the surface of the mirror in the experiment is to introduce larger convection heat transfer and, thereby, to increase the total heat flow rate. The simplified analysis of the free convection heat transfer for the vertical plane indicates that

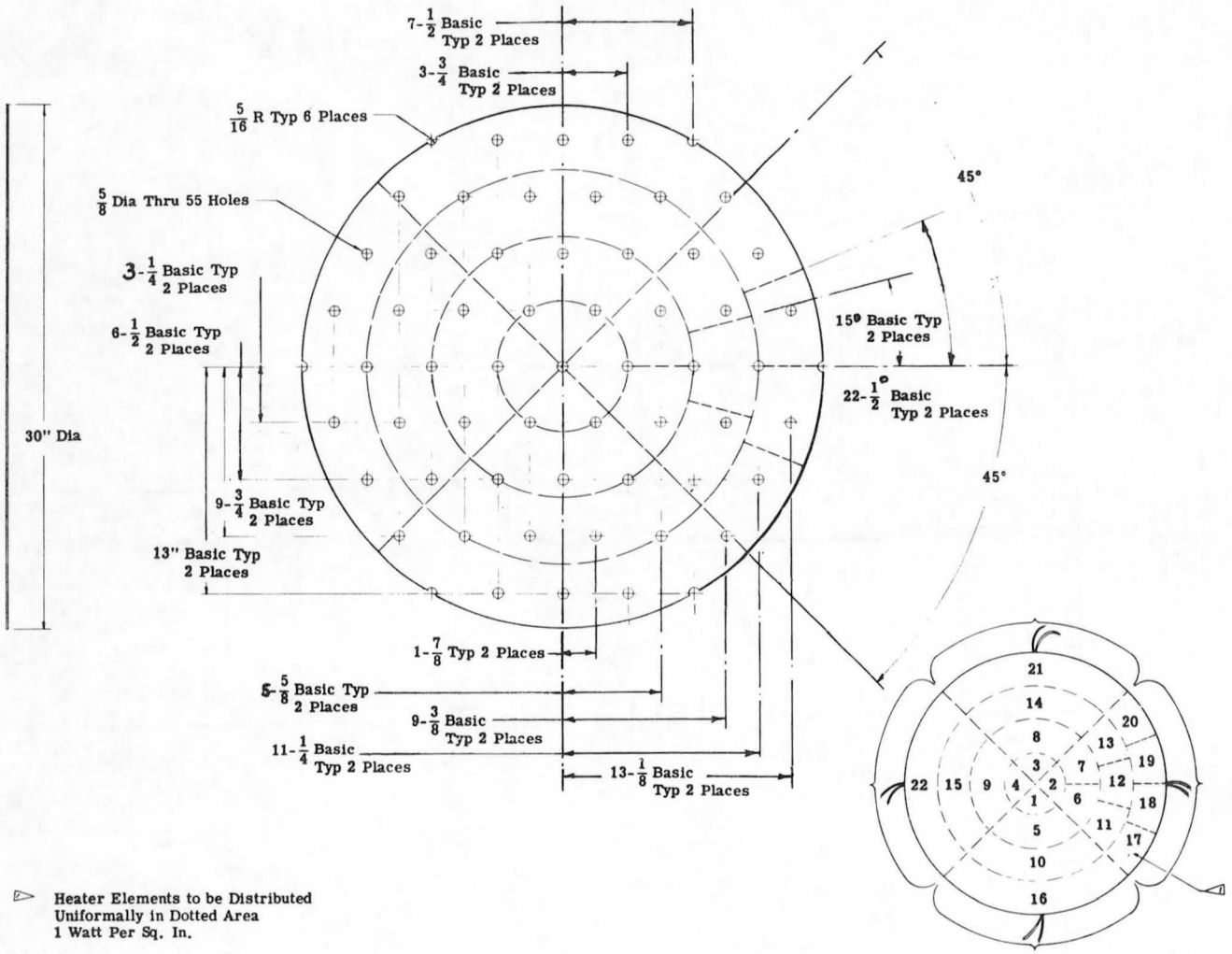


Figure 4-2. Heater Blanket - Deformable Mirror

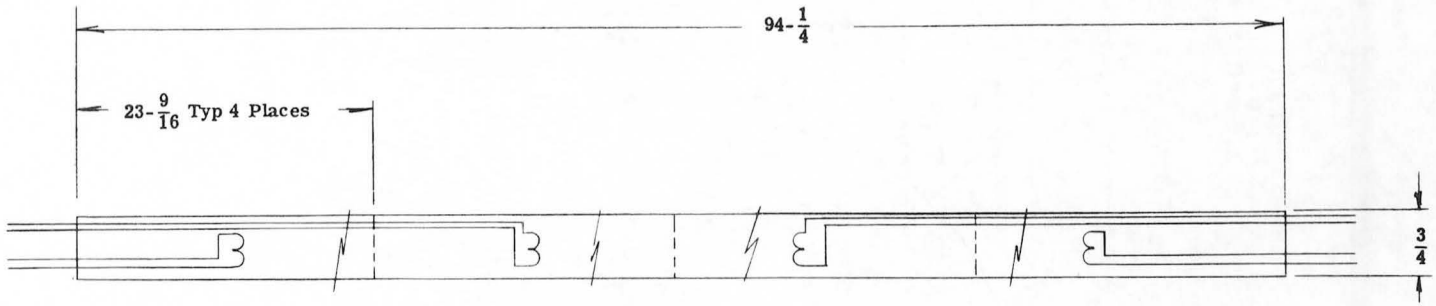


Figure 4-3. Circumference Heater Blanket - Deformable Mirror

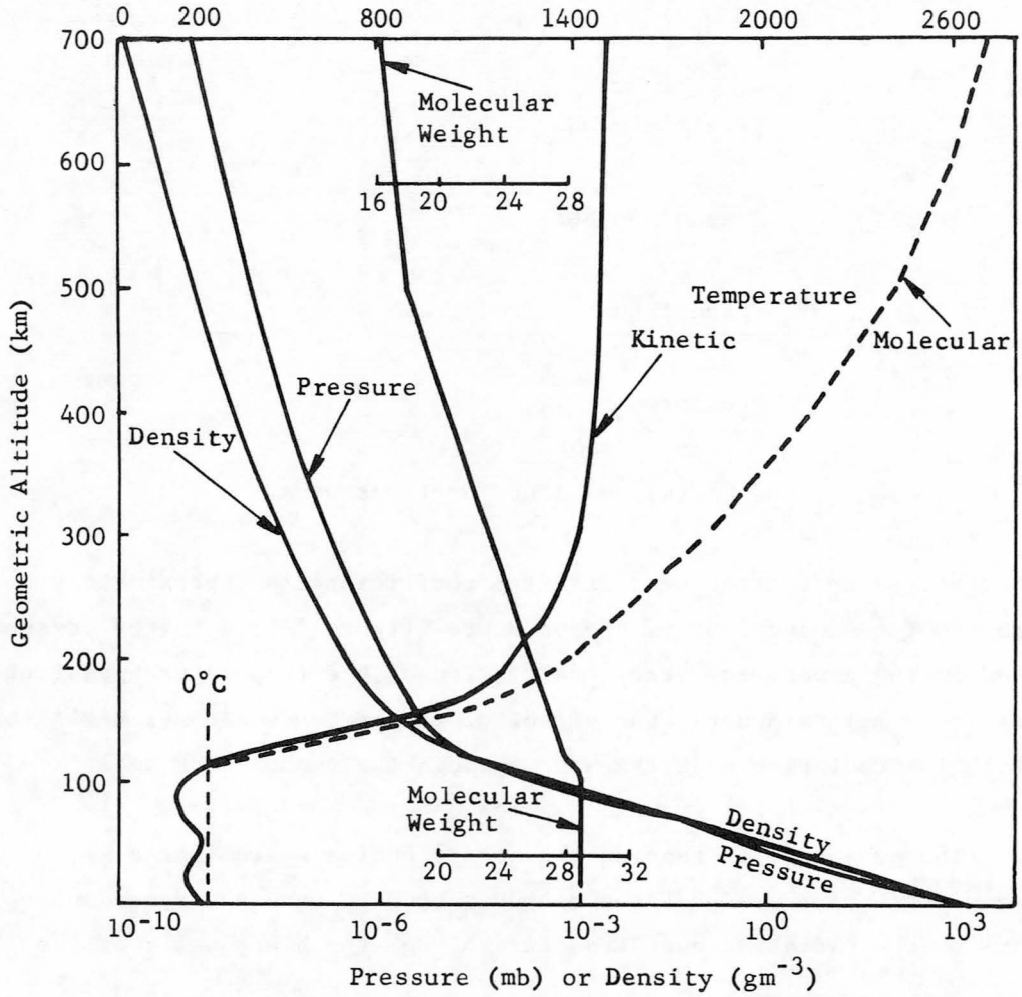


Figure4-4. Profiles to 700km of Temperature, Pressure, and Molecular Weight, According to U.S. Standard Atmosphere, 1962

$$N_{NU} = \mathfrak{F}\left[(N_{PR}\, N_{GR})^{1/4}\right]$$

$$N_{GR} = \mathfrak{F}\left[P^2\right]$$

where

N_{NU} = Nuselt's number

N_{GR} = Grashof number

N_{PR} = Prandtl number

P = Pressure

$\mathfrak{F}(x)$ and $\mathfrak{G}(x)$ = sine functions of x

Therefore, the free convection heat transfer coefficient is approximately proportional to the square root of the pressure (figure 4-5). As the pressure is decreased in the experiment, the localization of the temperature gradients becomes easier to maintain until the effect of the pressure becomes negligible compared with the radiation heat transfer through the vacuum tank wall.

The advantage of testing the Active Optics system for a given temperature distribution was that the measurement data were not dependent on the pressure or the radiation heat transfer through the black walls of the test tank.

4.1 THERMAL INSTRUMENTATION

Five-mil copper/constantan thermocouples were attached to the front and back surfaces of the mirror to measure the thermal contours produced. Figure 4-6 and 4-7 show the thermocouple distribution on the back and front surfaces of the mirror, respectively. The thermocouples were covered by small patches of pressure sensitive aluminum tape to help make good thermal contact with the mirror. Eight more thermocouples, which do not show in figure 4-6 and 4-7 were spaced at equal intervals around the edge of the mirror.

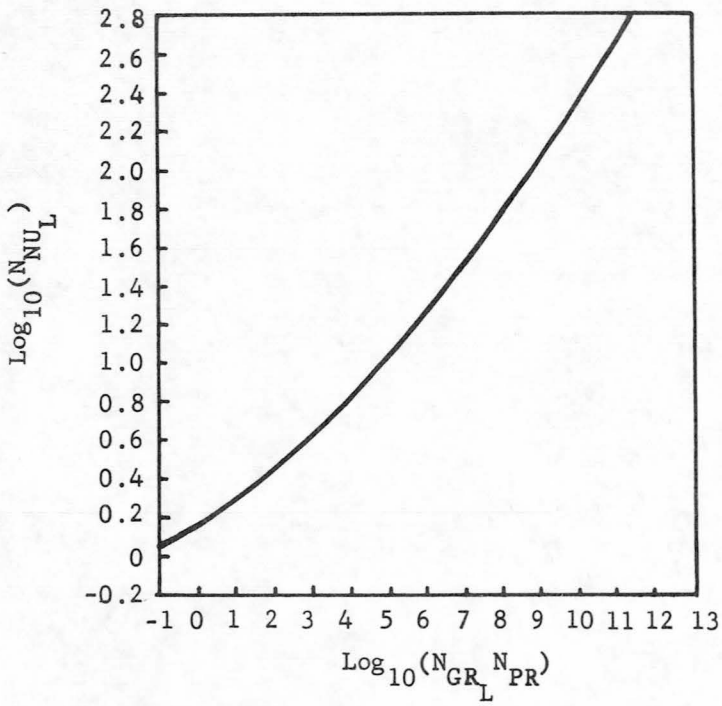


Figure 4-5. Recommended Correlation for Free Convection Around Vertical Plane Surfaces. (From W.H. McAdams, Heat Transmission, 3rd ed., New York, McGraw-Hill, 1954.)

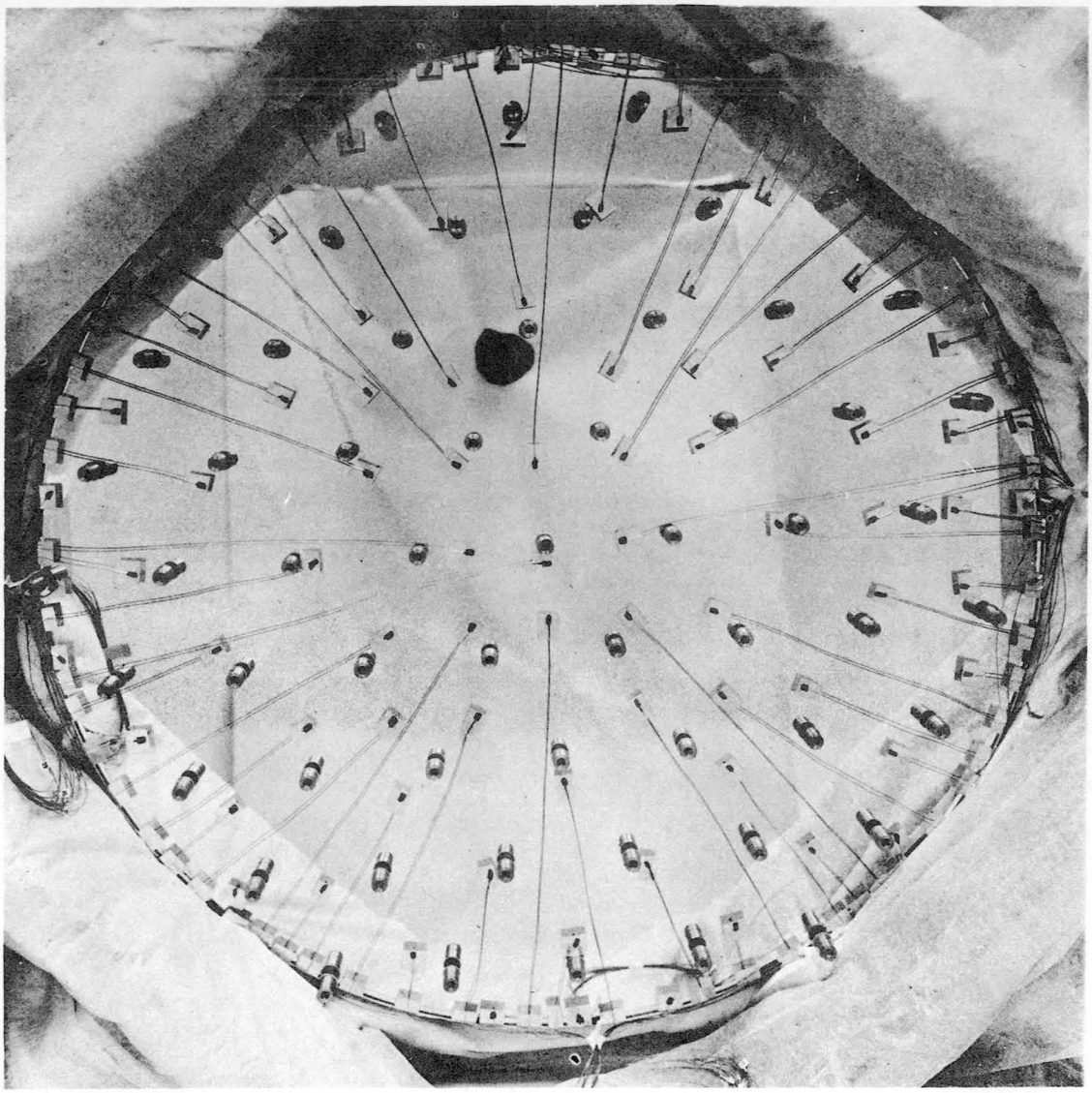


Figure 4-6. Thermocouple Arrangement on Back of 30 Inch Mirror

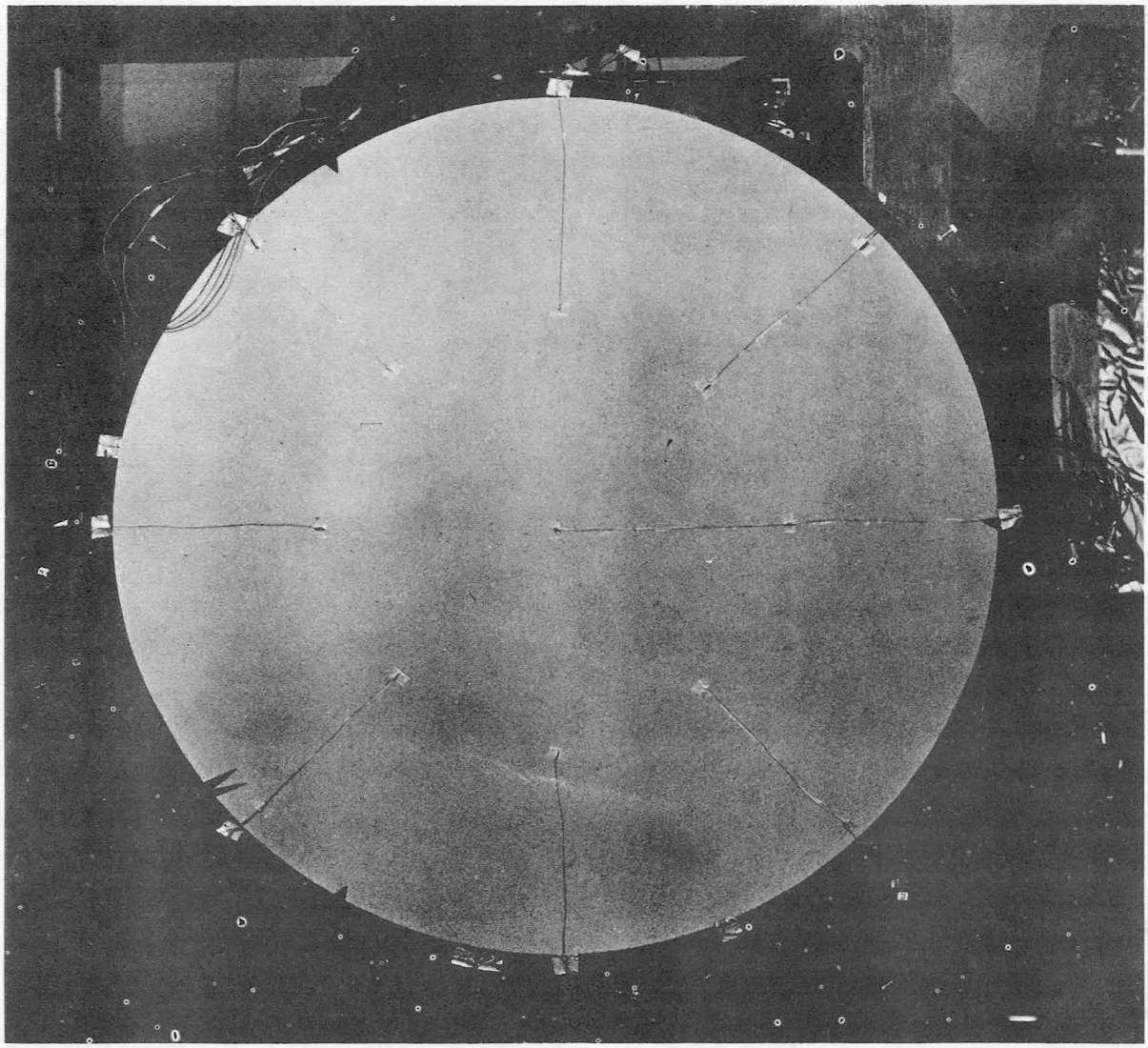


Figure 4-7. Thermocouple Arrangement on Front of 30 Inch Mirror

On the back of the mirror, over the thermocouples, the heating blanket was cemented in place using contact cement. The arrangement and orientation of the heating zones and the thermocouple numbering arrangement are shown in figure 4-8. The guard strip which is divided into four equal heating zones was cemented in place over the thermocouples around the mirror edge. Thermistors were attached to each heating zone to monitor the individual zones for use in automatically maintaining stead temperature levels.

Several layers of superinsulation were placed between the heating blankets and the backing plate in order to reduce heat loss from the blanket to the backing plate and to isolate the mirror from the heating effects of the actuator motors.

Twenty-six heaters were spatially arrayed on the mirror and individually held via associated thermiator sensors to desired set temperatures. Accurate determination of mirror temperature was accomplished by means of the array of thermocouples attached to the mirror front and back surfaces and its edge. Figure 4-9, a view of the associated control panel, shows the thermocouple jack panel on the left. The right-hand half of the panel pictorially presents the shape and location of the individual heaters as they would appear when the rear of the mirror is viewed. Heater No. 1, for example is pie-shaped and located just below the center of the mirror. As is apparent from the figure, the heater locations are panel designated by numbers appearing on the white squares. The positions of the various thermocouples are designated by the other numbers. All numbers are on overaly sheets that can be lifted to permit access to the temperature set potentiometers, which are mounted to the panel.

The dark circle below each heater designation number is the position of a neon indicator light, which lights whenever the blanket is receiving power. Directly below these neons are the screw-driver adjusted temperature set potentiometers.

Thermocouple Numbers 1 through 80 Are on Mirror Back Surface.
Thermocouple Numbers 81 through 88 Are on Mirror Edge.
Thermocouple Numbers 89 through 105 Are on Mirror Front Surface.

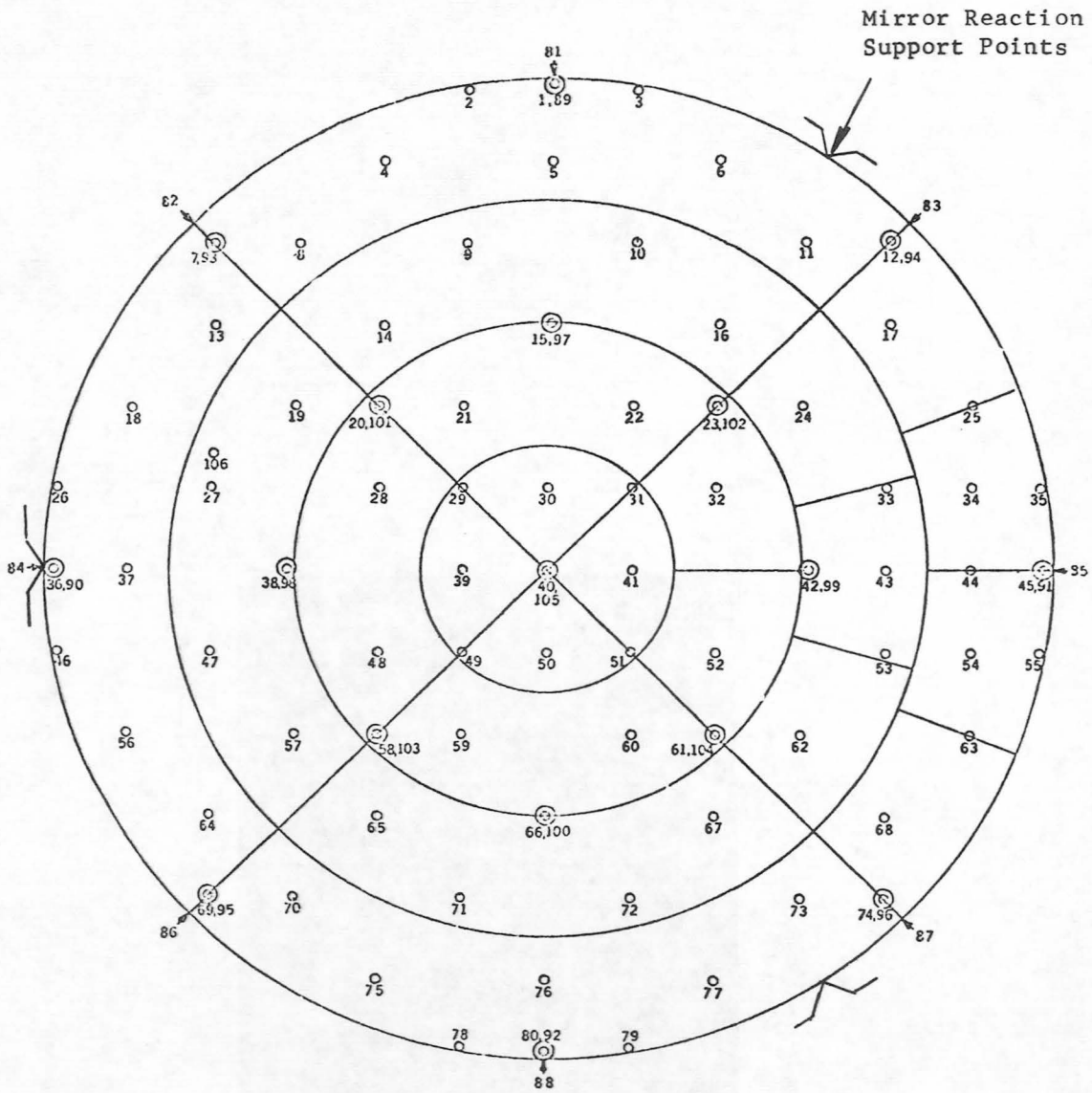


Figure 4-8. Thermocouple Arrangement as Seen from Back of Mirror

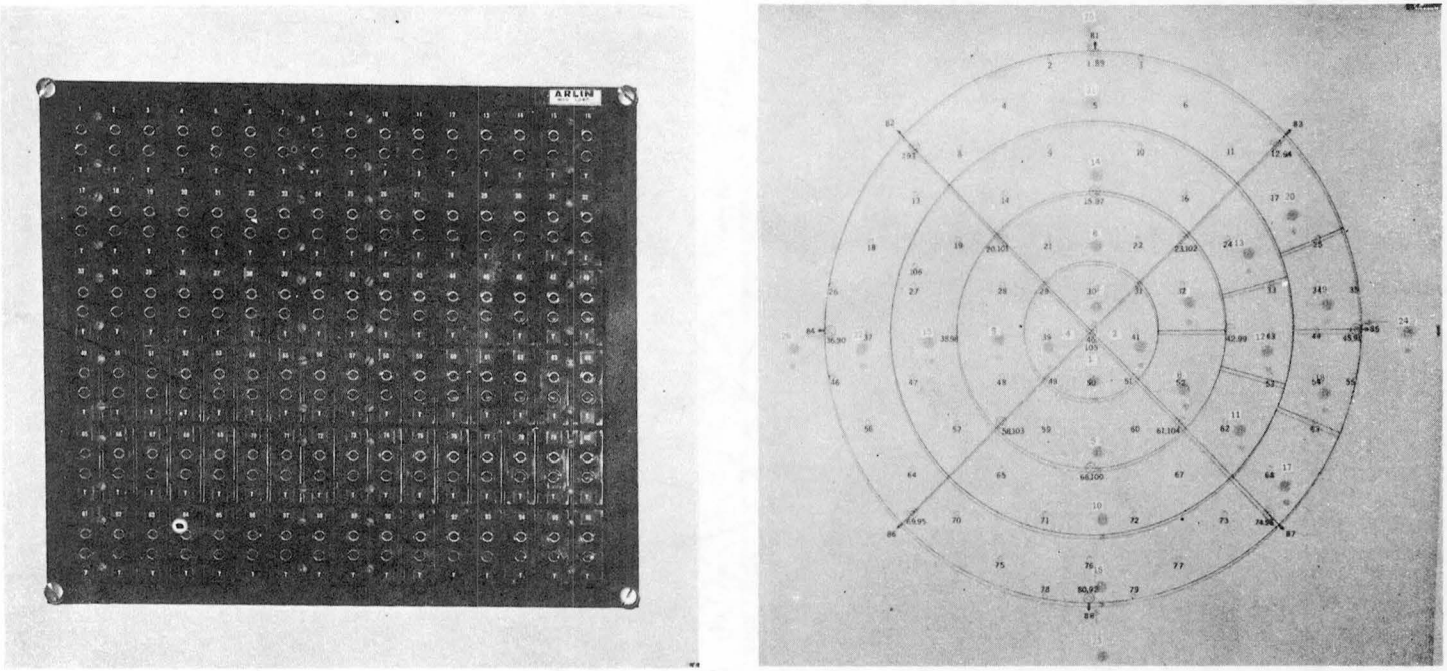


Figure 4-9. Thermal Control Panel and Thermocouple Jack Panel

Each of the 26 heaters was held at its set temperature by the control circuit as shown in figure 4-10. The arrangement features an A742 I.C., controlling an L2001M7 four quadrant triac and operates in zero crossing switching mode to avoid unnecessary EMI generation. A resistor bridge, comprised of the three 33K resistors plus an N.T.C. thermistor and series potentiometer, furnishes the necessary temperature error signal in electrical form.

The separation between the two temperatures at which the control circuit turns on or off at a given setting, which is a peak to peak measure of how close the controller can maintain a given temperature at the thermistor, is 0.06°F.

In practice, the effectiveness of the control circuit was modified by the fact that the thermistors were placed on the back of the heating blanket instead of between the heating blanket and the mirror, where the thermocouples are. This was done in order to make better contact between the mirror and the blanket; however, it does mean that the temperature being regulated is the temperature on the back of the blanket. The effects of this were minimized to reduce heat loss, but the effects were still noticeable in trying to achieve the distributed profiles desired and were the cause of most of the non-uniformities observed in these profiles.

4.2 TEST METHOD

Information concerning the effects of local gradients was obtained as follows:

(a) The mirror was aligned, the actuator positions and thermocouple readings were recorded and the servo control was then turned off.

(b) The heating elements were set for the desired gradient and the mirror was allowed to reach thermal equilibrium at the new gradient.

(c) The mirror deformation was photographed and thermocouple readings recorded.

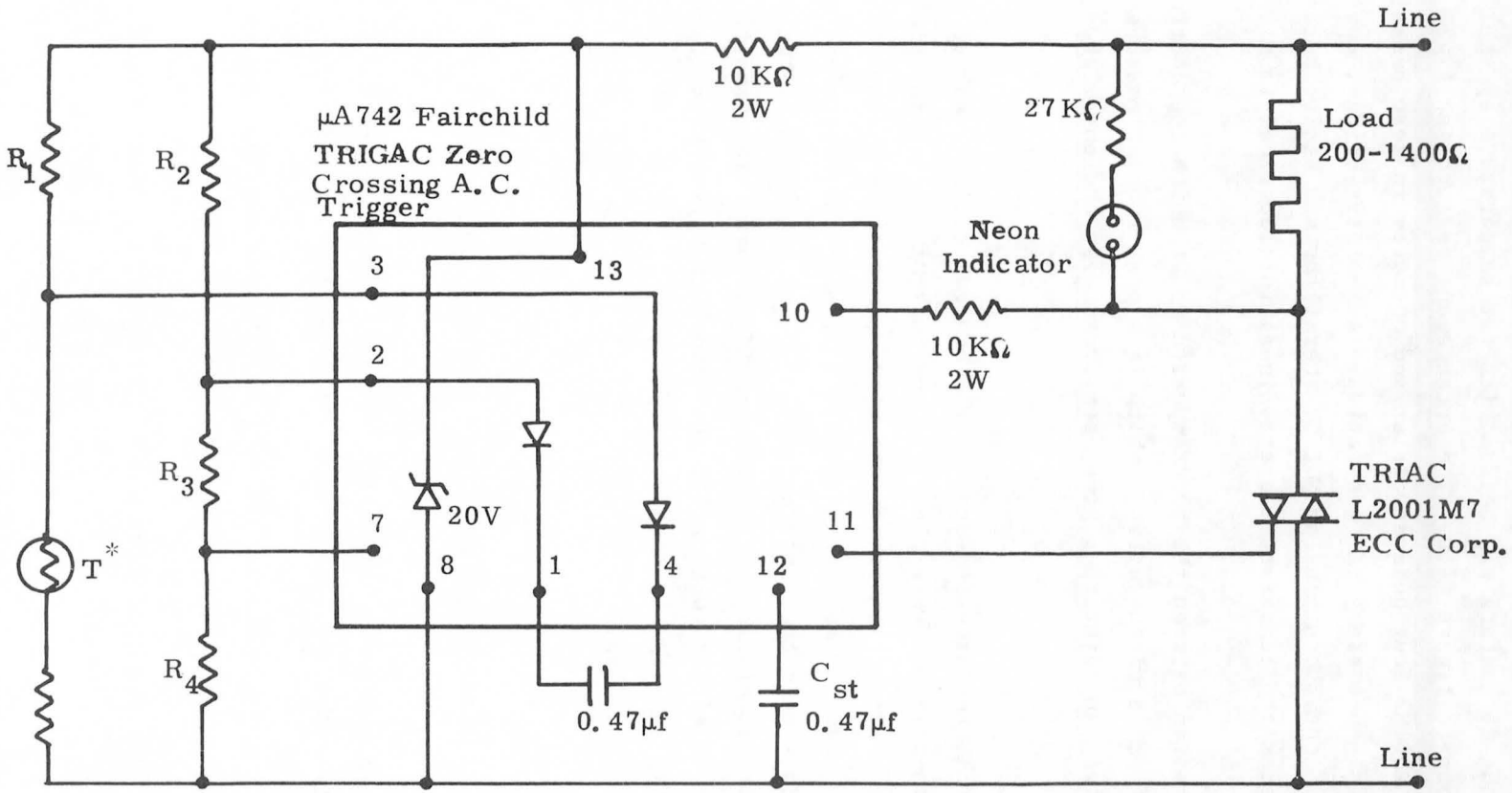


Figure 4-10. Automatic Heater Temperature Control

(d) The heating elements were turned off and the mirror allowed to reach stable equilibrium again at the initial thermal conditions.

(e) Step (a) was repeated without turning off the servo control.

(f) Step (b) was repeated with the servo control on to maintain alignment, and the actuator positions were recorded when thermal equilibrium had been reached.

(g) The applied thermal gradients were obtained by subtracting the thermocouple readings in step (a) from the thermocouple readings in step (c).

Information concerning the effects of distributed gradients was obtained in the following manner:

(a) The mirror was aligned and the actuator and thermocouple position were recorded.

(b) The heating elements were set for the desired gradient and the mirror was allowed to reach the desired thermal profile with the servo control on, to maintain alignment.

(c) The actuator and thermocouple temperatures were recorded.

(d) The servo control loops were opened and the heater elements turned off.

(e) After overnight normalization, the resulting interferogram was photographed.

4.3 RESULTS

In practice it was difficult to approximate some of the distributed profiles shown in figure 4-1. In particular the projected difference between front and back profiles (the axial gradient) actually obtained was much smaller than expected in comparison with the radial gradients.

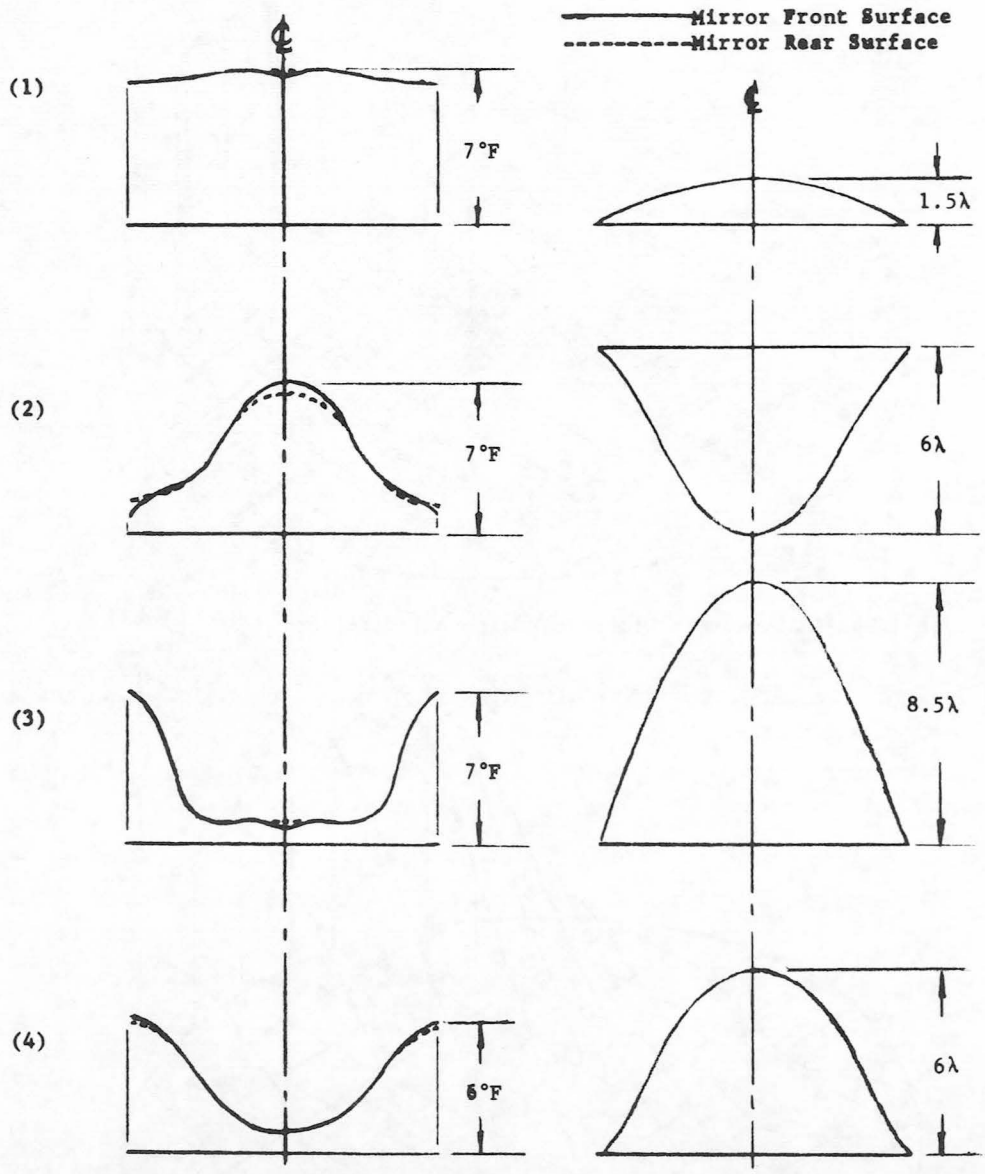
The actual temperature profiles obtained for the axisymmetric thermal distributions applied are shown in figure 4-11(a). The measured data was averaged to give the symmetrical radial component for each of the four distributions. The temperature profile obtained for the non-symmetrical thermal distribution is shown in figure 4-12(a).

The temperature profiles obtained for the localized thermal gradients applied are shown in figure 4-13.

The mirror deformations produced by the applied thermal gradients are obtained from the interferograms shown in figure 4-14 for the distributed gradients, and in figure 4-15 for the localized gradients. Figure 4-11(b) shows the averaged symmetrical radial component for the four axially symmetrical distributed gradients. Figure 4-12(b) shows the resultant deformation for the non-symmetrical distributed gradient of figure 4-12(a). Figure 4-16 shows a typical deformation profile for one of the localized external gradients.

The changes in temperature measured at each of the thermocouple locations, from which the changes in thermal gradient were plotted, are given in Table 4-1 for the profiles shown in figures 4-11(a) and 4-12(a), and in Table 4-2 for the profiles shown in figure 4-13. The mirror figure changes induced by the changes in thermal gradient are measured from the interferograms and are given in Table 4-3 for the errors caused by the profiles of figures 4-11(a) and 4-12(a) and in Table 4-4 for the errors caused by the profiles of figure 4-13. The forces applied by the actuators to remove the figure errors produced by the thermal profiles shown in figures 4-11(a) and 4-12(a) are given in Table 4-5.

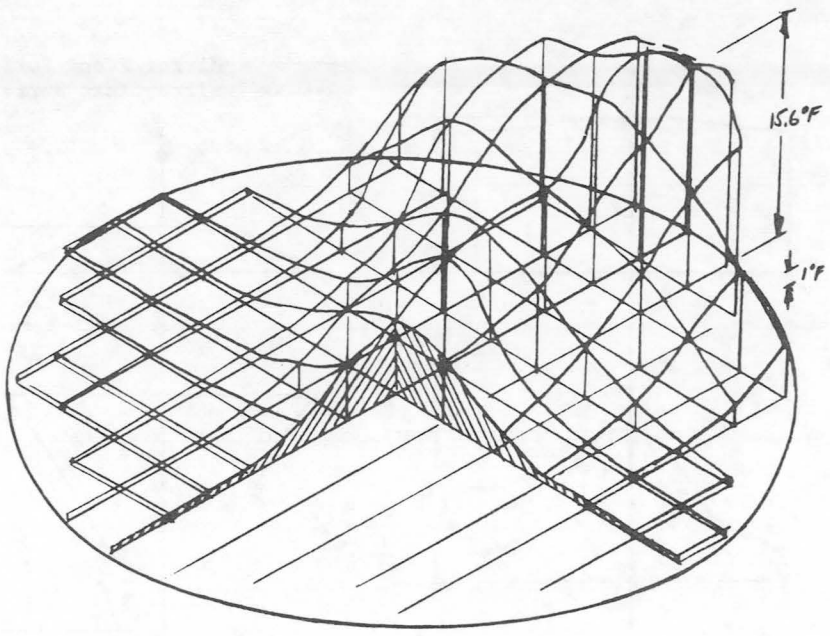
The flex actuators had sufficient range to maintain the mirror figure for the gradients applied; however, the rate of heat application had to be controlled since the actuators could not always keep pace with the change when the heat was applied at the full 1 watt per square inch capability of the heating blanket. In some cases the maximum rate of heat application had to be reduced by a factor of two.



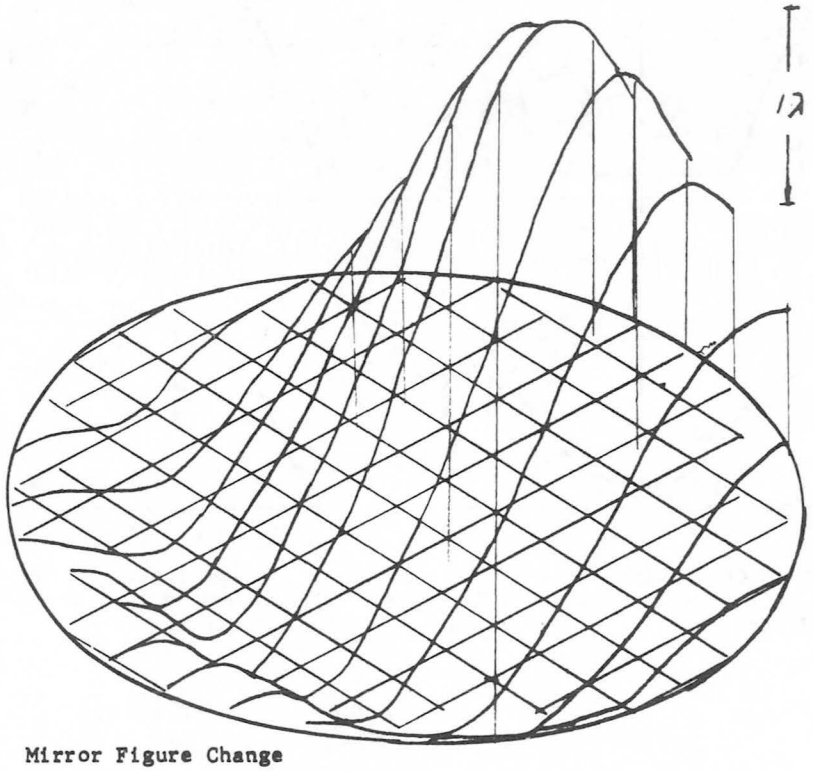
(a) Average Gradient Profiles for "Axially Symmetric" Thermal Profiles

(b) Mirror Figure Change Profiles caused by Applied Thermal Gradients

Figure 4-11. Mirror Deteriorations Due to Axi-Symmetric Distributed Thermal Gradients, Numbers 1 through 4.



(a) Non-Axisymmetric Distributed Thermal Gradient



(b) Mirror Figure Change

Figure 4-12. Distributed Thermal Gradient Number 5 and Resultant Mirror Deformation

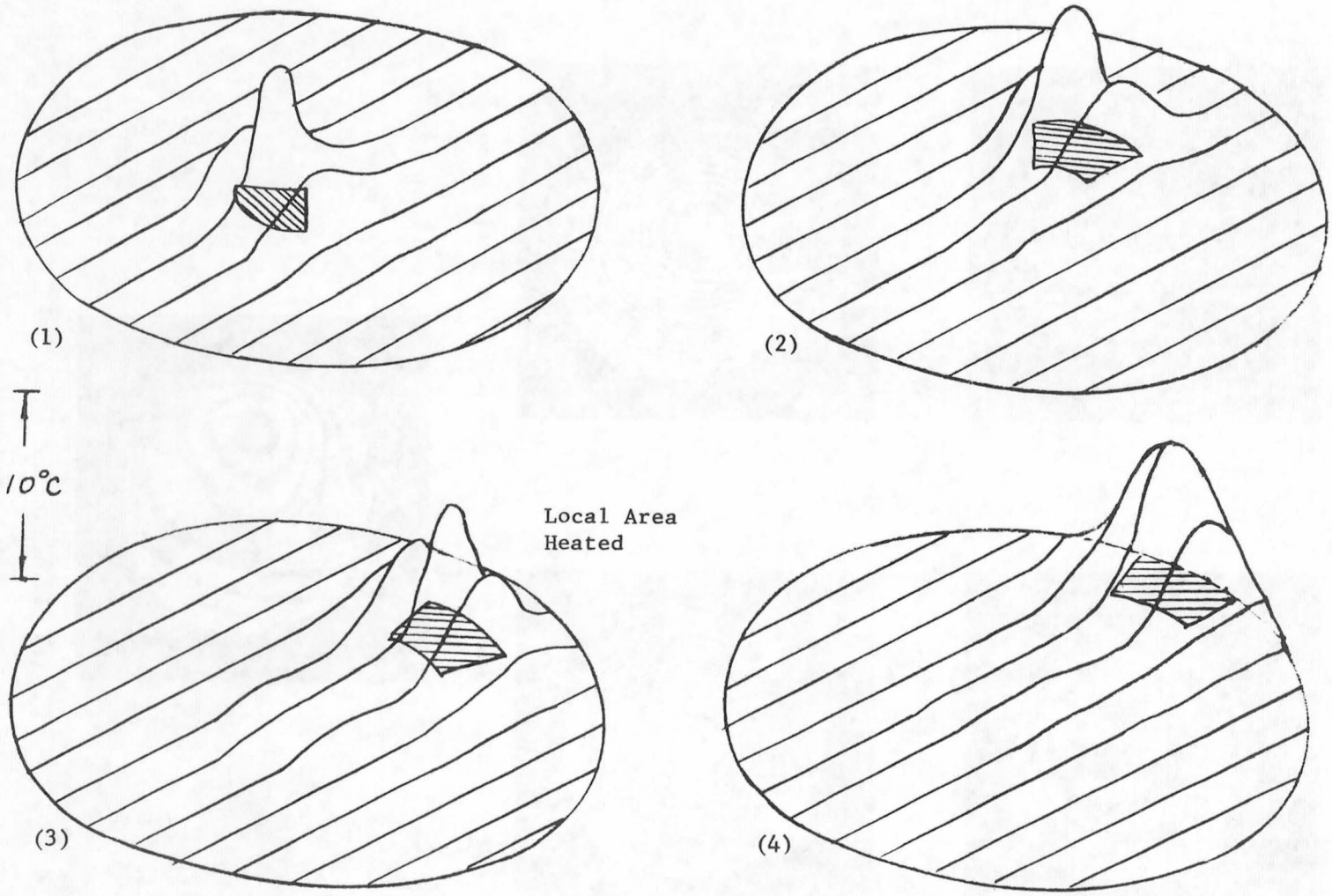
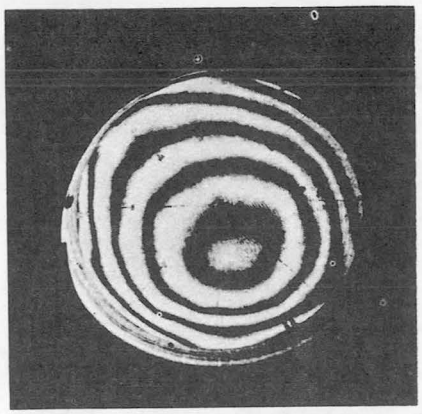
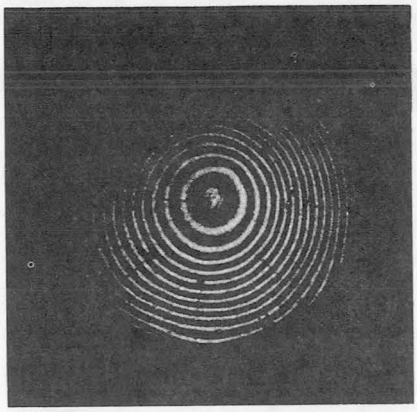


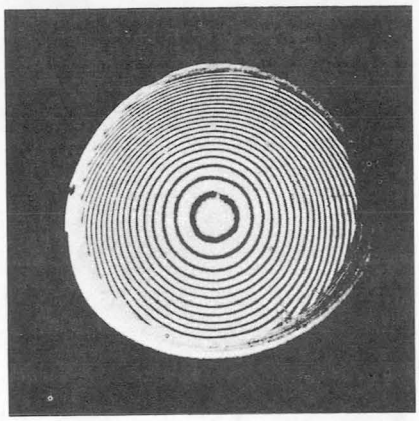
Figure 4-13. Localized Thermal Gradients Applied to Mirror



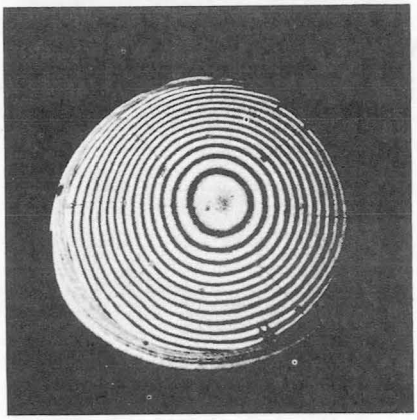
(a) From Profile No. 1



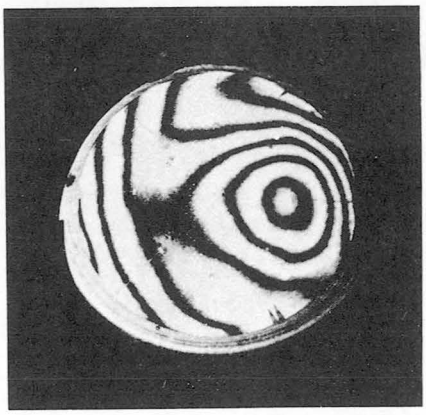
(b) From Profile No. 2



(c) From Profile No. 3

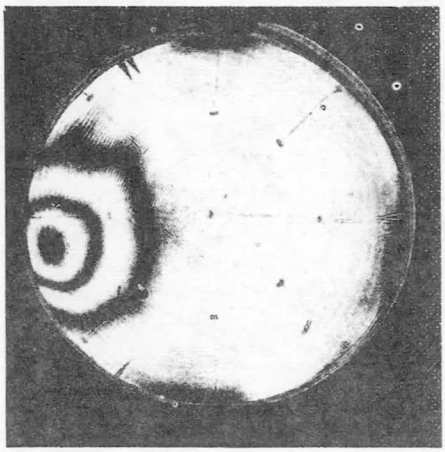


(d) From Profile No. 4

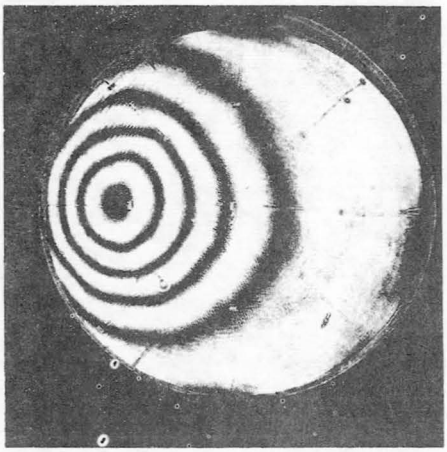


(e) From Profile No. 5

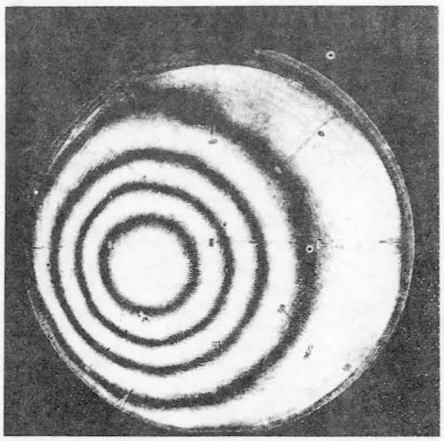
Figure 4-14. Interferograms Showing Mirror Deformations Due to Distributed Thermal Gradients of Figure 4-1(a)



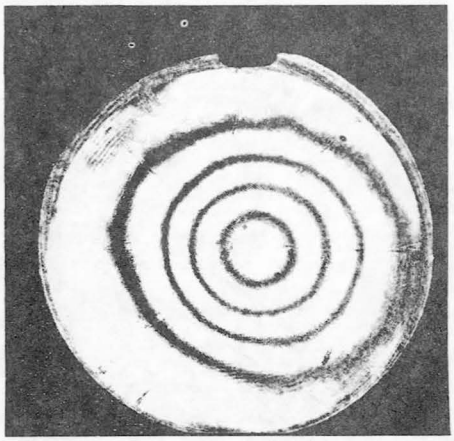
(a) From Profile No. 1



(b) From Profile No. 2



(c) From Profile No. 3



(d) From Profile No. 4

Figure 4-15. Interferograms Showing Mirror Deformations Caused By Local Thermal Gradients of Figure 4-13

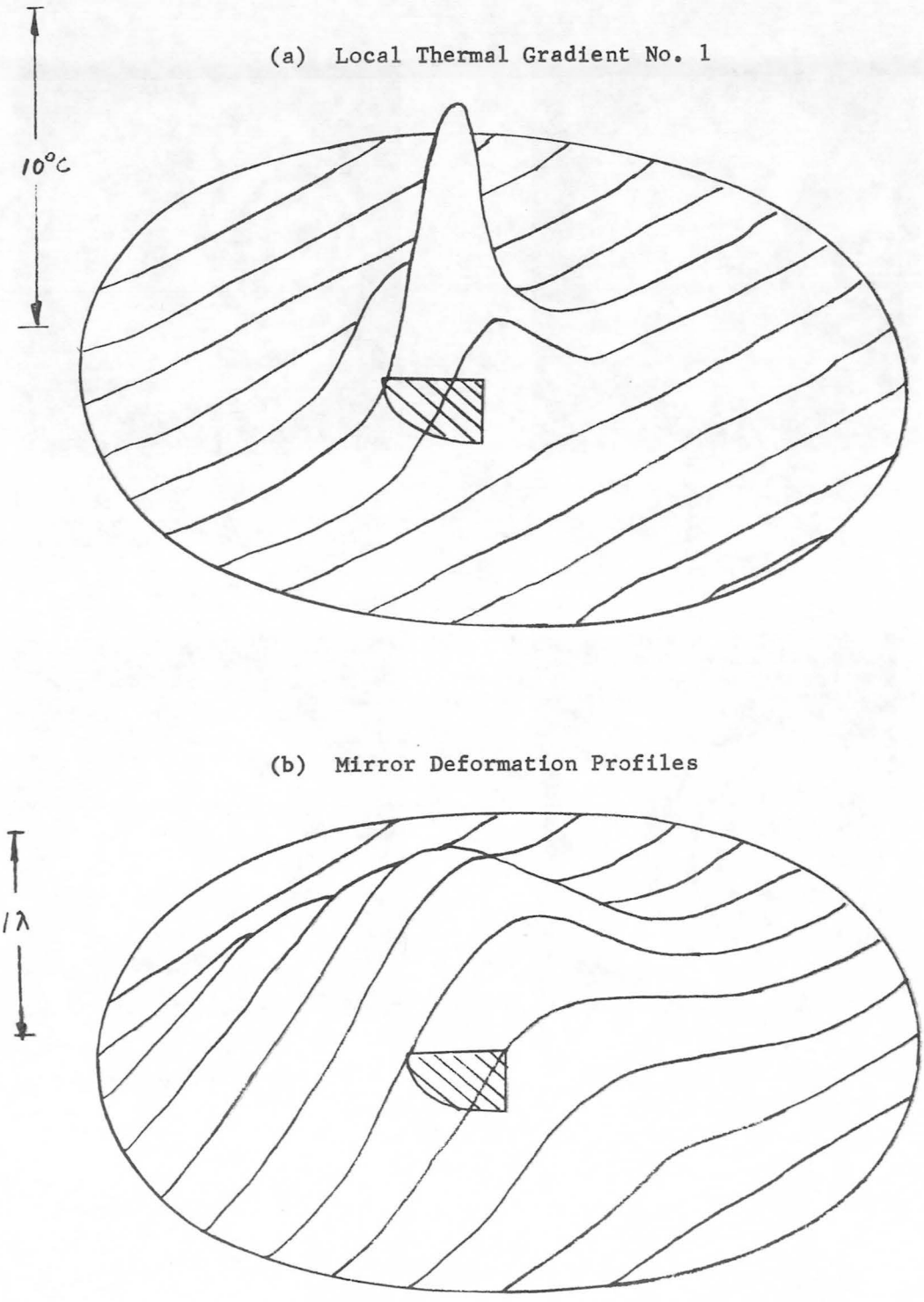


Figure 4-16. Localized Thermal Gradient No. 1 and Resultant Mirror Deformation

TABLE 4-1 CHANGES IN TEMPERATURE MEASURED AT THERMOCOUPLES FOR THERMAL GRADIENT PROFILES SHOWN IN FIGURES 4-11(a) AND 4-12(a)

Thermo-Couple Number	ΔT(°C) for Figure 4-11(a) Profiles				ΔT for Figure 4-12(a) Profile #5	Thermo-Couple Number	ΔT(°C) for Figure 4-11(a) Profiles				ΔT for Figure 4-12(a) Profile #5
	#1	#2	#3	#4			#1	#2	#3	#4	
1	3.2	0.6	3.5	3.0	0.3	27					0.1
2		0.2			0.2	28					0.4
3		0.1			0.3	29					1.2
4		0.2			0.1	30	3.2	3.3	0.6	0.7	2.2
5	3.3	0.2	3.7	3.0	0.1	31					3.2
6		1.4			0.1	32					4.1
7		0.2			0.1	33					7.2
8					0.1	34		0.8	3.4		0.2
9		0.6			0.1	35	3.2				6.4
10		0.6			0.1	36		0.2	4.1	3.4	0.2
11					0.1	37	3.2	0.1	3.6	3.7	0.2
12		0.6			2.7	38	2.8	0.8	0.1	1.4	0.2
13					0.1	39	3.5	0.6	0.8	0.7	2.6
14		1.0			0.1	40	3.2	3.9	0.5	0.5	3.1
15	2.8	1.9	0.2	0.6	0.2	41	3.5	4.1	0.8	0.6	4.5
16					1.0	42	3.0	2.1	0.3	0.6	5.0
17			3.3		5.6	43	3.3		1.2	1.4	7.9
18		0.1			0.2	44	3.0	0.8	3.3	2.9	8.6
19					0.1	45	2.5		3.4	2.8	6.7
20		1.9			0.2	46					0.2
21					0.4	47					0.1
22					1.1	48					0.5
23					2.5	49					1.4
24					5.5	50	4.2	4.2	0.8	0.8	2.2
25		1.1			6.7	51					2.8
26					0.2	52					3.4

TABLE 4-1. (Continued)

Thermo-Couple Number	ΔT(°C) for Figure 4-11(a) Profiles				ΔT for Figure 4-12(a) Profile #5	Thermo-Couple Number	ΔT(°C) for Figure 4-11(a) Profiles				ΔT for Figure 4-12(a) Profile #5
	#1	#2	#3	#4			#1	#2	#3	#4	
53					7.5	80	3.1		4.5	3.7	0.2
54		0.8	3.7		9.2	81	3.3	0.3	4.0	2.2	0.3
55					7.7	82					0.2
56					0.3	83		0.7			0.5
57		2.4			0.1	84	3.0	0.2	3.9	2.6	0.2
58					0.2	85	2.6		3.9	2.3	6.3
59					0.4	86					0.2
60					0.8	87		0.9			3.2
61		1.9			2.1	88	3.6	0.9	3.9	1.6	0.3
62					3.9	89	3.2	0.3	3.9	3.2	0.2
63					7.1	90	3.3		3.6	3.2	0.2
64					0.1	91	2.5		3.5	2.9	6.3
65		0.7			0.2	92	3.3	0.7	3.8	3.2	0.2
66	3.9	1.2	0.1	0.6	0.2	93					0.1
67					0.9	94					2.9
68			3.1		4.2	95					0.1
69					0.1	96		0.9			2.6
70					0.2	97	2.8		0.3	0.7	0.3
71		0.6			0.1	98	3.0	0.5	0.3	2.4	0.2
72		0.7			0.2	99	3.2	1.9		0.9	5.9
73					0.9	100	3.9	1.0	2.7		0.2
74		0.9			2.3	101					0.3
75					0.3	102					0.5
76	3.2	0.8	3.4	3.1	0.2	103		1.2			0.2
77		0.9				104					2.2
78						105	3.5	3.5	0.8	0.5	3.0
79											

TABLE 4-2. CHANGES IN TEMPERATURE MEASURED AT THERMOCOUPLES FOR THERMAL GRADIENT PROFILES SHOWN IN FIGURE 4-13.

Actuator Number	ΔT(°C) for Profiles				Actuator Number	ΔT(°C) for Profiles			
	#1	#2	#3	#4		#1	#2	#3	#4
1		0.4	0.2	0.4	29		1.2	0.4	3.4
2		0.3	0.1	0.3	30		1.9	1.2	2.3
3	-0.1	0.4	0.1	0.3	31	0.4	2.2	4.4	0.7
4		0.1	0	0.1	32	0.3	3.3	9.4	0.5
5		0.1	0	0.1	33	4.1	7.8	1.0	0.5
6	-0.3	0.3	0	0.1	34	10.0	4.8	0.5	0.6
7		0.2	0.1	0.2	35	7.6	3.2	0.4	0.5
8		0	0.1	0	36		0.3	0.1	0.2
9		-0.1	0	0.1	37		0.2	0.1	0.1
10	-0.1	0.1	0	0.1	38		0.2	0.1	0.4
11	0	0.6	0.1	0.1	39		1.9	0.9	9.7
12	0.2	1.1	0.2	0.3	40		2.1	1.0	3.8
13		0.1	0	0.1	41	0.8	2.9	2.9	1.4
14		0	0	0.1	42	0.5	6.8	4.3	0.4
15		0.3	0	0.1	43	2.7	10.8	1.0	0.6
16	0	0.8	0.3	0.1	44	6.3	5.6	0.5	0.5
17	0.9	2.2	0.4	0.5	45	4.7	3.3	0.3	0.4
18		0.2	0.1	0.1	46		0.3	0.1	0.2
19		0	0.1	0.1	47		0	0	0
20		0.2	0	0.2	48		0.5	0.2	1.4
21		0.5		0.5	49		1.3	0.6	3.6
22	0	1.0	0.2	0.2	50		2.0	1.1	2.4
23	0	1.9	3.4	0.3	51	0.4	2.0	0.9	0.8
24	0.8	3.1	1.6	0.4	52	0.5	3.3	1.3	0.7
25	6.5	3.1	0.4	0.5	53	0.9	7.8	0.6	0.5
26		0.3	0.2	0.2	54	1.6	4.4	0.5	0.5
27		0	0	0	55	1.6	2.8	0.4	0.5
28		0.3	0.1	1.0	56		0.3	0.1	0.1

TABLE 4-2. (Continued)

Actuator Number	ΔT(°C) for Profiles				Actuator Number	ΔT(°C) for Profiles			
	#1	#2	#3	#4		#1	#2	#3	#4
57		0.1	0.1	0.1	82		0.4	0.2	0.4
58		0.2	0.1	0.2	83	0.2	1.1	0.3	0.4
59		0.5	0.2	0.5	84		0.4	0.1	0.2
60	0.2	1.0	0.2	0.2	85	5.6	3.1	0.4	0.4
61	0.1	1.7	0.2	0.3	86		0.3	0.2	0.2
62	0.3	2.9	0.5	0.5	87	0.2	1.1	0.4	0.4
63	0.5	2.7	0.5	0.5	88		0.4	0.2	0.3
64		0.1	0	0.1	89		0.3	0.1	0.2
65		0	0	0	90		0.4	0.1	0.2
66		0.3	0.1	0.1	91	4.6	3.1	0.3	0.3
67	0	0.8	0.1	0.2	92		0.5	0.2	0.3
68	0.3	2.0	0.5	0.6	93		0.3	0.1	0.2
69		0.2	0.1	0.1	94	0.2	1.1	0.2	0.4
70		0.1	0.1	0	95		0.2	0.1	0.2
71		0.1	0.1	0.1	96	0.1	1.2	0.3	0.4
72	-0.2	0.2	0	0.1	97		0.3	0.1	0.2
73	-0.1	0.6	0.1	0.1	98		0.2	0.1	0.2
74	0	0	0.3	0.4	99	0.9	8.3	2.9	0.5
75		0.2	0.1	0.2	100		0.3	0.1	0.1
76		0.2	0.1	0.1	101		0.2	0.1	0.3
77	-0.1	0.3	0	0.2	102	0.1	1.9	2.4	0.3
78		0.4	0.2	0.3	103		0.2	0.2	0.2
79	0	0.4	0.2	0.2	104	0.2	1.8	0.4	0.4
80		0.3	0.2	0.2	105		2.1	1.0	4.0
81		0.4	0.2	0.3					

TABLE 4-3. FIGURE ERRORS INDUCED BY APPLIED THERMAL PROFILES OF FIGURES 4-11(a) AND 4-12(a) INFRINGES AT 6328Å (1 FRINGE = 12.46 MICRO INCHES).

Displacement away from center of curvature defined as positive. (Actuator numbering arrangement as shown in Figure 3-5.)

Actuator Number	Figure 4-11(a) #1 (1.8 rms)	#2 (5.7 rms)	#3 (8.6 rms)	#4 (5.8 rms)	Fig. 4-12(a) #5 (1.8 rms)	Actuator Number	Figure 4-11(a) #1	#2	#3	#4	Fig. 4-12(a) #5
2	-0.5	1.2	-2.2	-1.0	-0.1	25	-1.8	4.6	-7.5	-4.7	-0.6
3	-0.5	1.2	-2.2	-1.0	-0.1	26	-3.1	11.2	-15.5	-11	0.2
4	-0.7	1.5	-3.0	-1.5	-0.1	27	-3.1	11.2	-15.5	-11	0.2
5	-1.3	3.3	-5.8	-3.2	-0.2	28	-1.8	4.6	-7.5	-4.7	-0.6
6	-0.7	1.5	-3.0	-1.5	-0.1	29	-0.7	1.5	-3.0	-1.5	-0.1
7	-0.5	1.2	-2.2	-1.0	-0.1	30	-2.7	8.8	-13.0	-9.0	0
8	-1.8	4.6	-7.5	-4.7	-0.4	31	-3.3	12.3	-16.7	-12	1.3
9	-1.8	4.6	-7.5	-4.7	-0.4	32	-2.7	8.8	-13.0	-9.0	0
10	-0.5	1.2	-2.2	-1.0	-0.1	33	-0.7	1.5	-3.0	-1.5	-0.1
11	0	0	0	0	0	34	-1.8	4.6	-7.5	-4.7	-0.2
12	-1.8	4.6	-7.5	-4.7	-0.5	35	-3.1	11.2	-15.5	-11	1.5
13	-2.4	7.0	-11.5	-7.8	-0.8	36	-3.1	11.2	-15.5	-11	1.5
14	-1.8	4.6	-7.5	-4.7	-0.5	37	-1.8	4.6	-7.5	-4.7	-0.2
15	0	0	0	0	0	38	-0.5	1.2	-2.2	-1.0	0
16	-1.3	3.3	-5.8	-3.2	-0.3	39	-2.4	7.0	-11.5	-7.8	1.1
17	-2.7	8.8	-13.0	-9.0	-6.5	40	-3.1	11.2	-15.5	-11	3.0
18	-2.7	8.8	-13.0	-9.0	-6.5	41	-2.4	7.0	-11.5	-7.8	1.1
19	-1.3	3.3	-5.8	-3.2	-0.3	42	-0.5	1.2	-2.2	-1.0	0
20	-0.5	1.2	-2.2	-1.0	-0.1	43	-1.3	3.3	-5.8	-3.2	0.5
21	-2.4	7.0	-11.5	-7.8	-0.6	44	-2.7	8.8	-13.0	-9.0	3.0
22	-3.1	11.2	-15.5	-11	-0.1	45	-2.7	8.8	-13.0	-9.0	3.0
23	-2.4	7.0	-11.5	-7.8	-0.6	46	-1.3	3.3	-5.8	-3.2	0.5
24	-0.5	1.2	-2.2	-1.0	-0.1	48	-1.8	4.6	-7.5	-4.7	2.1

TABLE 4-3. (Continued)

Actuator Number	Figure 4-11(a) #1 (1.8 rms)	#2 (5.7 rms)	#3 (8.6 rms)	#4 (5.8 rms)	Fig. 4-12(a) #5 (1.8 rms)	Actuator Number	Figure 4-11(a) #1	#2	#3	#4	Fig. 4-12(a) #5
49	-2.4	7.0	-11.5	-7.8	4.1	56	-0.7	1.5	-3.0	-1.5	2.2
50	-1.8	4.6	-7.5	-4.7	2.1	57	-1.3	3.3	-5.8	-3.2	3.6
52	-0.5	1.2	-2.2	-1.0	1.0	58	-0.7	1.5	-3.0	-1.5	2.2
53	-1.8	4.6	-7.5	-4.7	3.5	59	-0.5	1.2	-2.2	-1.0	2.4
54	-1.8	4.6	-7.5	-4.7	3.5	60	-0.5	1.2	-2.2	-1.0	2.4
55	-0.5	1.2	-2.2	-1.0	1.0	61	0	0	0	0	2.1

TABLE 4-4. FIGURE ERRORS INDUCED BY APPLIED THERMAL PROFILES OF FIGURE 4-13 IN FRINGES AT 6328Å (1 FRINGE = 12.46 MICROINCHES).

Displacement away from center of curvature defined as positive. (Actuator numbering arrangement as shown in figure 3-5.)

Actuator Number	Profile #1 (0.6 rms)	Profile #2 (1.4 rms)	Profile #3 (1.5 rms)	Profile #4 (1.4 rms)	Actuator Number	Profile #1	Profile #2	Profile #3	Profile #4
2				0.4	31		1.4	2.7	3.2
3				0.4	32		0.8	1.2	1.6
4				0.5	33				
5				0.9	34		0.5	1.5	0.4
6				0.5	35	0.2	1.2	3.5	3.6
7				0.3	36	0.1	1.2	2.5	3.6
8			0.2	1.2	37		0.5	0.5	0.4
9			0.1	1.2	38			0.3	
10				0.3	39	0.3	1.5	3.0	1.0
11					40	0.4	2.5	3.8	2.5
12				1.1	41	0.1	1.5	1.6	1.0
13		0.1		2.3	42				
14				1.1	43	0.2	0.8	1.5	0.1
15					44	0.6	2.4	3.8	1.2
16			0.3	0.5	45	0.5	2.4	3.0	1.2
17		0.2	0.8	2.5	46		0.8	0.6	0.1
18		0.2	0.6	2.5	48	0.7	2.0	2.5	0.3
19				0.5	49	1.0	4.2	3.7	0.9
20			0.1		50	0.4	2.0	1.6	0.3
21		0.3	1.0	1.7	52	0.3	0.8	0.8	
22		0.5	1.4	3.2	53	1.5	3.5	2.9	0.2
23		0.3	0.6	1.7	54	0.9	3.5	2.3	0.2
24					55	0.1	0.8	0.4	
25		0.2	1.0	0.5	56	1.2	1.7	1.2	
26		0.8	2.0	3.3	57	1.8	3.6	2.0	0.1
27		0.8	1.5	3.3	58	0.4	1.7	0.6	
28		0.2	0.3	0.5	59	2.6	2.0	1.0	
29			0.3		60	0.8	2.0	0.8	
30		0.8	2.1	1.6	61	1.3	1.4	0.4	

TABLE 4-5. FORCES APPLIED BY ACTUATORS TO REMOVE FIGURE ERRORS PRODUCED BY THE THERMAL PROFILES SHOWN IN FIGURES 4-11(a) AND 4-12(a).

Forces given in pounds x 10^{-3}. (Actuator numbering arrangement as shown in Figure 3-5.)

Actuator Number	Δ Force for Figure 4-11(a) Profiles				Δ Force for Fig. 4-12(a) Profile
	#1	#2	#3	#4	#5
2	-15x 10^{-3} lbs	224x 10^{-3} lbs	-39x 10^{-3} lbs	-71x 10^{-3} lbs	-19x 10^{-3} lbs
3	61	73	-322	12	-13
4	64	157	-404	-74	-20
5	-175	-29	-239	-405	1
6	65	145	-399	-461	-25
7	26	12	-395	-175	-26
8	-116	251	146	-463	20
9	-122	126	120	-382	0
10	152	73	-323	17	-30
11	63	-4	-93	22	-23
12	-94	260	165	-153	-9
13	46	-115	440	121	76
14	132	14	124	-304	59
15	151	98	-91	-45	-12
16	-187	130	-223	-214	-22
17	159	-134	540	376	94
18	39	107	496	294	83
19	-134	17	-401	-434	-16
20	102	80	-314	-136	-43
21	90	-66	444	354	154
22	-12	362	286	258	-90
23	69	-52	478	191	102
24	246	326	-223	80	-48
25	-132	249	-13	-54	76
26	-25	-465	342	295	9
27	21	-250	395	566	37
28	-407	-179	-69	-910	65
29	90	154	-266	-223	-48
30	147	-394	548	530	204
31	-163	-565	995	-387	-306
32	-45	-282	455	403	230
33	198	237	-290	-47	-46
34	-74	230	-25	-32	163
35	39	-702	368	306	-104
36	-24	-274	300	-24	-18
37	-175	121	123	-322	157
38	-7	45	-368	-229	-56
39	44	109	302	221	313
40	-85	-442	265	411	-384
41	-103	-171	438	254	204
42	161	130	-320	40	-38
43	-106	264	-186	-278	98
44	6	-415	408	242	-249
45	10	-333	462	490	10
46	-179	37	-352	-430	107
48	-59	-179	-81	-69	-399
49	-94	21	269	253	-331
50	-170	67	84	-169	-100
52	3	279	-311	156	250

TABLE 4-5. (Continued)

Actuator Number	Δ Force for Figure 4-11(a) Profiles #1	#2	#3	#4	Δ Force for Fig. 4-12(a) Profile #5	Actuator Number	Δ Force for Figure 4-11(a) Profiles #1	#2	#3	#4	Δ Force for Fig. 4-12(a) Profile #5
53	-148	42	278	80	-510	58	112	298	-346	-169	103
54	-154	-50	67	-72	-527	59	160	169	-234	-126	398
55	82	154	-322	24	87	60	175	167	-288	-133	287
56	57	102	-376	-254	109	61	140	171	-36	16	314
57	-117	-30	-312	-288	-525						

4.4 CONCLUSIONS

The results show that the gradients produced by heat applied to small areas of the back of the thin deformable mirror are quite localized for pressures of one torr or less and the deformations produced by these localized gradients are also fairly localized. The effect of a distributed gradient appears to be equivalent to that which could be obtained by linear superposition of the effects of a set of local gradients whose linear superposition adds up to the distributed gradient. Since, for the 30-inch diameter thin mirror, the effects of a local gradient produced by heat applied to the back of the mirror consistently displaces the corresponding area of the mirror surface away from the center of curvature, it should be possible to predict the effect of distributed gradients of low spatial frequency from the observed results. The deformation due to the distributed gradients appear consistent with the above conclusion.

5.0 MODAL CONTROL

5.1 INTRODUCTION

It has been established that feedforward compensation can be used to decouple each of the control actuator channels while maintaining stability*. There are many possible approaches to optimization of the control system; however, a specific control law which takes advantage of the mirror's natural bending modes was selected for further investigation.

The method of control, referred to as modal control, was suggested by J.F. Creedon and A.G. Lindgren** and they demonstrated the possibility of determining the minimum number of actuators placed in an optimum configuration so as to obtain a minimum rms displacement error, for a flat, freely supported plate subjected to a "white" spatial force distribution. Their results show that 36 actuators could be employed for a 1/50 of a wavelength ($\lambda = 0.6328\text{Å}$) rms error instead of 58 actuators as used in the initial phase of the thin deformable mirror project.

One of the objects of the present phase of study was to determine similar information for the thin spherical mirror on a three point support. The bending mode shapes and their associated natural frequencies of vibration were analytically and experimentally determined (see appendix A) since this information is required to obtain the optimum actuator placement. These results yielded mode shapes and their associated frequencies for the three point support system.

To determine actuator locations the strategy used is to control the dominant low frequency modes by placing control actuators at or near nodal contours of higher order modes which, if unexcited, do not contribute to the total rms error after control. Creedon and Lindgren found the square flat plate amenable to application of this strategy because the nodal contours fol-

*Reference No. 1

**Reference No. 2

a relatively simple pattern. It was discovered from the resulting modal wave-shapes for the thin spherical mirror, however, that the nodal contours of the various modes did not follow a simple pattern when more than eight modes were considered. Further, it was also discovered that by including the 15 dominant modes, which comprised 99% of the specified mirror figure error of one wavelength rms amplitude, it is not possible at this time to determine their placement to obtain anywhere near $\lambda/50$ error with control because of the very large number of possible actuator configurations. It became obvious at this point that a somewhat less ambitious approach would have to suffice to demonstrated that the modal control approach performed as predicted when applied to the actual active optics mirror and mounting system.

The next phase of the study was to assume a limited number of actuator and sensor points to enable a design procedure using modal control. The approach taken was to select four control points and three additional uncontrolled points. Thus, seven sensed points, including the actuator points, would feed data into a modal controller yielding four outputs which would drive their corresponding actuators with the desired result that:

(a) The four controlled mode amplitudes should go from non-zero before control to zero after control

(b) The three uncontrolled mode amplitudes should not change significantly.

The former result would be obtained due to the presence of an integrating servomechanism if the actuators are not located exactly on the nodal contours of the first four modes. The latter result would only be obtained if the actuator placements were chosen at or near the nodal contours of the next higher order modes 5, 6, and 7. Experimental measurements verified that this approach gives the predicted results, thereby validating the modal control approach and furthermore establishing the design procedure as a workable one.

The next section deals with the details of the modal control approach in achieving the cited results.

5.2 SYSTEM ANALYSIS

A model of the system to be analyzed is shown in figure 5-1 of this report. A partitioned model is shown in figure 5-2. The model of figure 5-2 will be used to show that the error vectors, $\bar{e}_N$ and $\bar{e}_R$, are identical to the mode vectors $\bar{C}_N$ and $\bar{C}_R$. Then the simpler model of figure 5-1 will be used to calculate the mode vector, $\bar{c}$, and the mirror figure vector, $\bar{w}$, when modal control is being applied.

From figure 5-2, the mirror acts as a mode analyzer which yields the mirror figure vector

$$\bar{W} = \begin{pmatrix} \bar{W}_N \\ \hdashline \bar{W}_R \end{pmatrix} = \underline{U_M}\,\bar{C} = \left[\begin{array}{c:c} \underline{U_{NN}} & \underline{U_{NR}} \\ \hdashline \underline{U_{RN}} & \underline{U_{RR}} \end{array}\right] \left[\begin{array}{c} \bar{C}_N \\ \hdashline \bar{C}_R \end{array}\right]$$

Likewise, the controller contains a synthesizer which yields the control vector,

$$\bar{\epsilon} = \left[\begin{array}{c} \bar{\epsilon}_N \\ \hdashline \bar{\epsilon}_R \end{array}\right] = -\underline{U_M}\,\bar{W} = -\left[\begin{array}{c:c} (\underline{U_M})^{-1}_{NN} & (\underline{U_M})^{-1}_{NR} \\ \hdashline (\underline{U_M})^{-1}_{RN} & (\underline{U_M})^{-1}_{RR} \end{array}\right] \left[\begin{array}{c} \bar{W}_N \\ \hdashline \bar{W}_R \end{array}\right]$$

Thus, it appears that $\bar{\epsilon} = -\underline{U_M}^{-1}\,\underline{U_M}\,\bar{C} = -\bar{C}$

so that $\bar{\epsilon}_N = -\bar{C}_N$, $\bar{\epsilon}_R = -\bar{C}_R$

Consequently,

$$\bar{W}_{N'} = +\frac{k}{s}\,\underline{\Lambda_N}\,\underline{H_{NN}}\,\underline{H_{NN}}^{-1}\,\bar{\epsilon}_N = -\bar{q}_N + \bar{C}_N = \frac{-K}{s}\,\underline{\Lambda_N}\,\bar{C}_N$$

since $\bar{C}_N = -\bar{\epsilon}_N$. Then

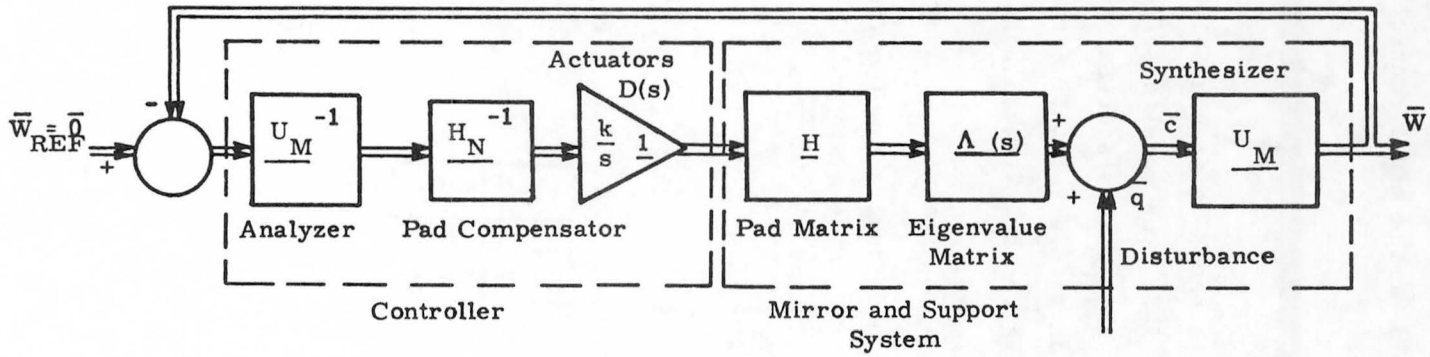


Figure 5-1. Model of Modal Control System

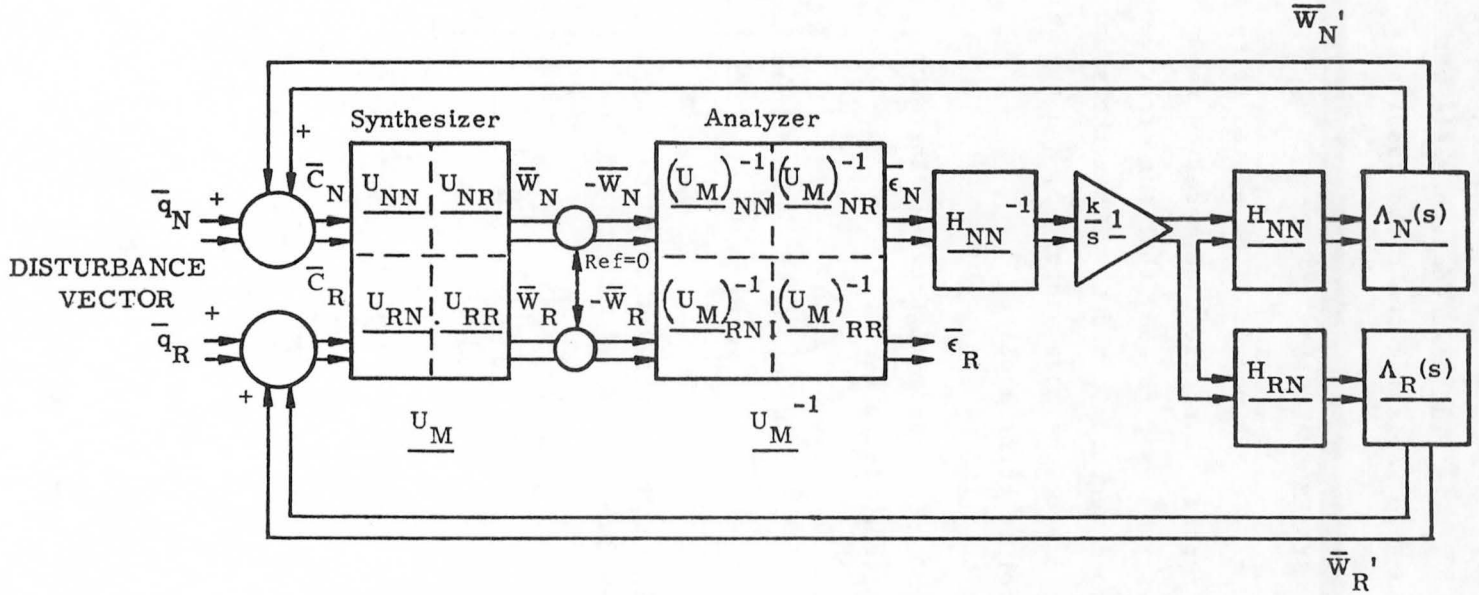


Figure 5-2. Partitioned Model of Modal Control System

$$\bar{C}_N = \left[\underline{1} + \frac{k}{s}\underline{\Lambda_N}\right]^{-1} \bar{q}_N$$

Similarly

$$\bar{W}_{R'} = \frac{k}{s}\underline{\Lambda_R}\,\underline{H_{RN}}\,\underline{H_{NN}}^{-1}\bar{e}_N = -\frac{K}{s}\underline{\Lambda_R}\,\underline{H_{RN}}\,\underline{H_{NN}}^{-1}(1+\frac{k}{s}\Lambda_N)^{-1}\bar{q}_N$$

so that

$$\bar{C}_R = \bar{q}_R - \frac{k}{s}\underline{\Lambda_R}\,\underline{H_{RN}}\,\underline{H_{NN}}^{-1}\,(1 + \frac{k}{s}\underline{\Lambda_N})^{-1}\,\bar{q}_N$$

and since $\bar{W} = U_M \bar{C}$

$$\bar{W}_N = \underline{U_{NN}}\,\bar{C}_N + \underline{U_{NR}}\,\bar{C}_R$$

$$\bar{W}_R = \underline{U_{RN}}\,\bar{C}_N + \underline{U_{RR}}\,\bar{C}_R$$

The resulting steady state vectors for step disturbances will then be

$$\bar{C}_{N_{SS}} = \lim_{S\to 0} S\,(\underline{1} + \frac{K}{s}\underline{\Lambda_N})^{-1}\,\frac{\bar{q}_N}{s} = 0$$

$$\bar{C}_{R_{SS}} = \lim_{S\to 0}\frac{S\bar{q}_R}{s} - \lim_{S\to 0} S\frac{K}{s}\,\underline{\Lambda_R}(s)\,\underline{H_{RN}H_{NN}}^{-1}(1+\frac{K}{s}\underline{\Lambda_N}(s))^{-1}\,\frac{\bar{q}_N}{s}$$

$$= \bar{q}_R - \underline{\Lambda_R}(o)\,\underline{H_{RN}}\,\underline{H_{NN}}^{-1}\,\underline{\Lambda_N}(o)^{-1}\,\bar{q}_N$$

so that

$$\bar{W}_{N_{SS}} = \underline{U_{NR}}\,\bar{C}_{R_{SS}}$$

$$\bar{W}_{R_{SS}} = \underline{U_{RR}}\,\bar{C}_{R_{SS}}$$

Summarizing the analysis, the following resulting matrix equations are:

(1) Controlled Modal Amplitude Vector:

$$\bar{C}_N = \left[\underline{1} + \frac{k}{s}\underline{\Lambda_N}(s)\right]^{-1} \bar{q}_N \quad ; \quad (Nx)$$

where $\bar{q}_N$ is the disturbance vector for the N controlled modes.

(2) Uncontrolled Modal Amplitude Vector:

$$\bar{C}_R = \bar{q}_R - \frac{k}{s}\underline{\Lambda_R}(s)\underline{H_{RN}}\,\underline{H_{NN}}^{-1}\left[\underline{1} + \frac{k}{s}\underline{\Lambda_N}(s)\right]^{-1}\bar{q}_N \quad ; \quad (Rx)$$

where $\bar{q}_R$ is the disturbance vector for the R uncontrolled modes.

(3) Actuator Displacement Amplitude Vector:

$$\bar{W}_N = \underline{U_{NN}}\bar{C}_N + \underline{U_{NR}}\,\bar{C}_R$$

(4) Uncontrolled Displacement Amplitude Vector:

$$\bar{W}_R = \underline{U_{RN}}\,\bar{C}_N + \underline{U_{RR}}\,\bar{C}_R$$

where $\underline{U_{NN}}$, $\underline{U_{NR}}$, $\underline{U_{RN}}$, and $\underline{U_{RR}}$ are partitions of the modal matrix U_M; N represents the number of actuators being controlled out of M possible points and R = M - N.

The above results assume simple integrating actuators of equal gain k.

If the disturbance vectors $\bar{q}_N$ and $\bar{q}_R$ are step functions, the resulting steady state mode amplitude vectors can be calculated from (1) thru (4) as:

(5) $$\bar{C}_{N_{ss}} = 0$$

(6) $$\bar{C}_{R_{ss}} = \bar{q}_R - \underline{\Lambda_R}(o)\,\underline{H_{RN}}\,\underline{H_{NN}}^{-1}\,\Lambda_N(o)\,\bar{q}_N$$

$$(7) \quad \bar{W}_{N_{ss}} = \underline{U_{NR}}\, \bar{C}_{R_{ss}}$$

$$(8) \quad \bar{W}_{R_{ss}} = \underline{U_{RR}}\, \bar{C}_{R_{ss}}$$

The rms mode amplitude in steady state will then be

$$(9) \quad C_{RMS} = \frac{1}{M} \sqrt{\left(\bar{C}_{R_{ss}}\right)^T \bar{C}_{R_{ss}}}$$

(M = the number of sensor points)

Likewise, the rms figure error will be

$$(10) \quad W_{RMS} = \frac{1}{M} \sqrt{\left(\bar{W}_{ss}\right)^T \bar{W}_{ss}} = \frac{1}{M} \sqrt{\left((\underline{U_{NR}} + \underline{U_{RR}})\bar{C}_{R_{ss}}\right)^T (\underline{U_{NR}} + \underline{U_{RR}})\bar{C}_{R_{ss}}}$$

5.3 VERIFICATION OF MODAL CONTROL APPROACH

Having established the validity of the mirror's natural modes and characteristic frequencies it was decided to perform a design for a test case on a limited number of actuators, with experimental verification. The work performed herein gives the analysis leading to the design of a four-actuator system. Seven sensing points that include the four actuator points were chosen. It is the design objective to diminish the four most dominant modes by modal control, without simultaneously exciting the three next most dominant modes.

5.3.1 Selected Configuration

Figure 5-3 shows sketches of the nodal contours (locus of zero deformation) of the seven most dominant modes, 1 through 7. As the mode number increases, characteristic frequency increases and the corresponding amplitude tends to decrease monotonically. Figure 5-4 shows a composite or superposition of modes 5, 6, and 7, which are not to be excited while controlling

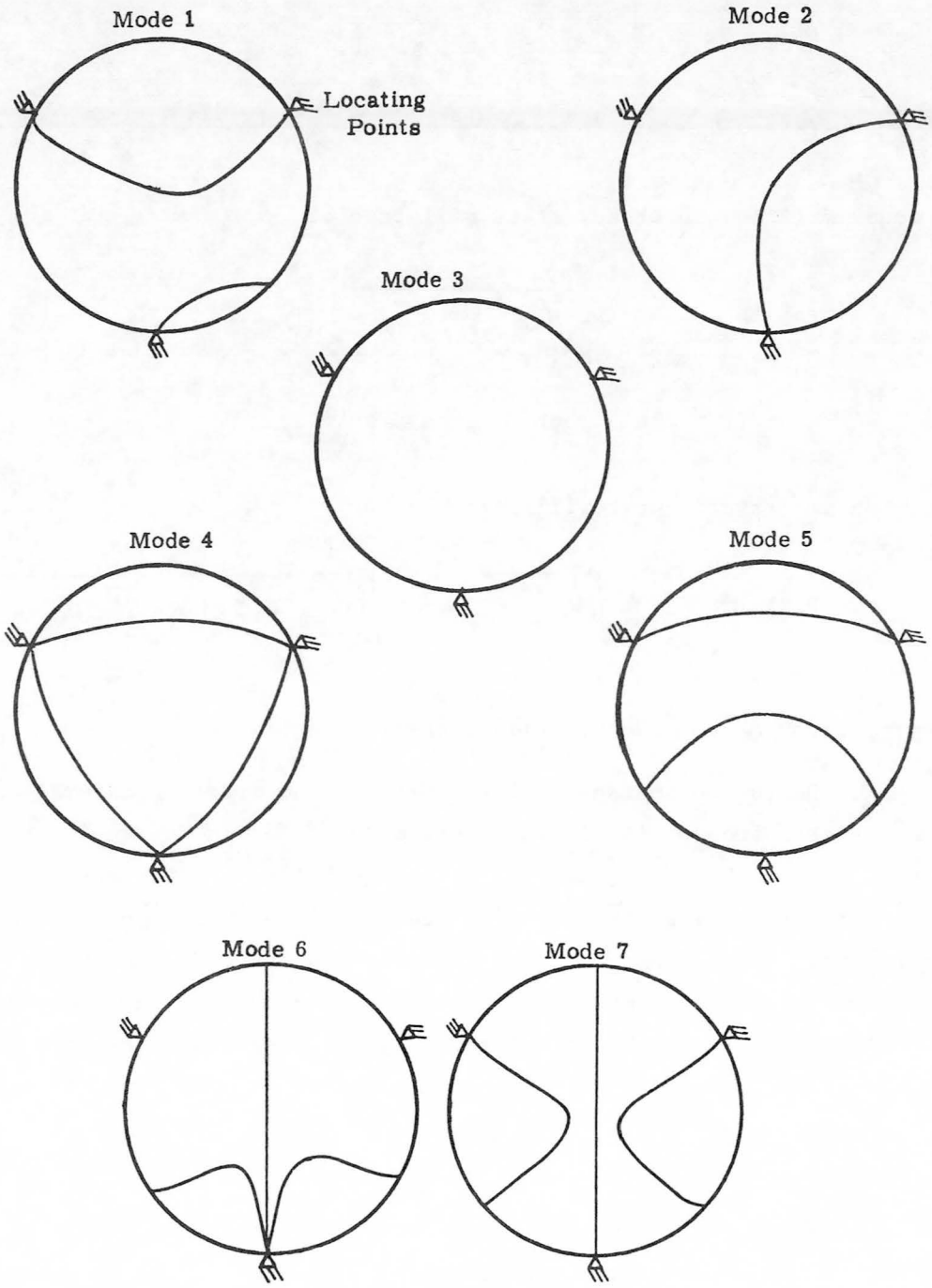


Figure 5-3. Nodal Contours of First Seven Dominant Modes

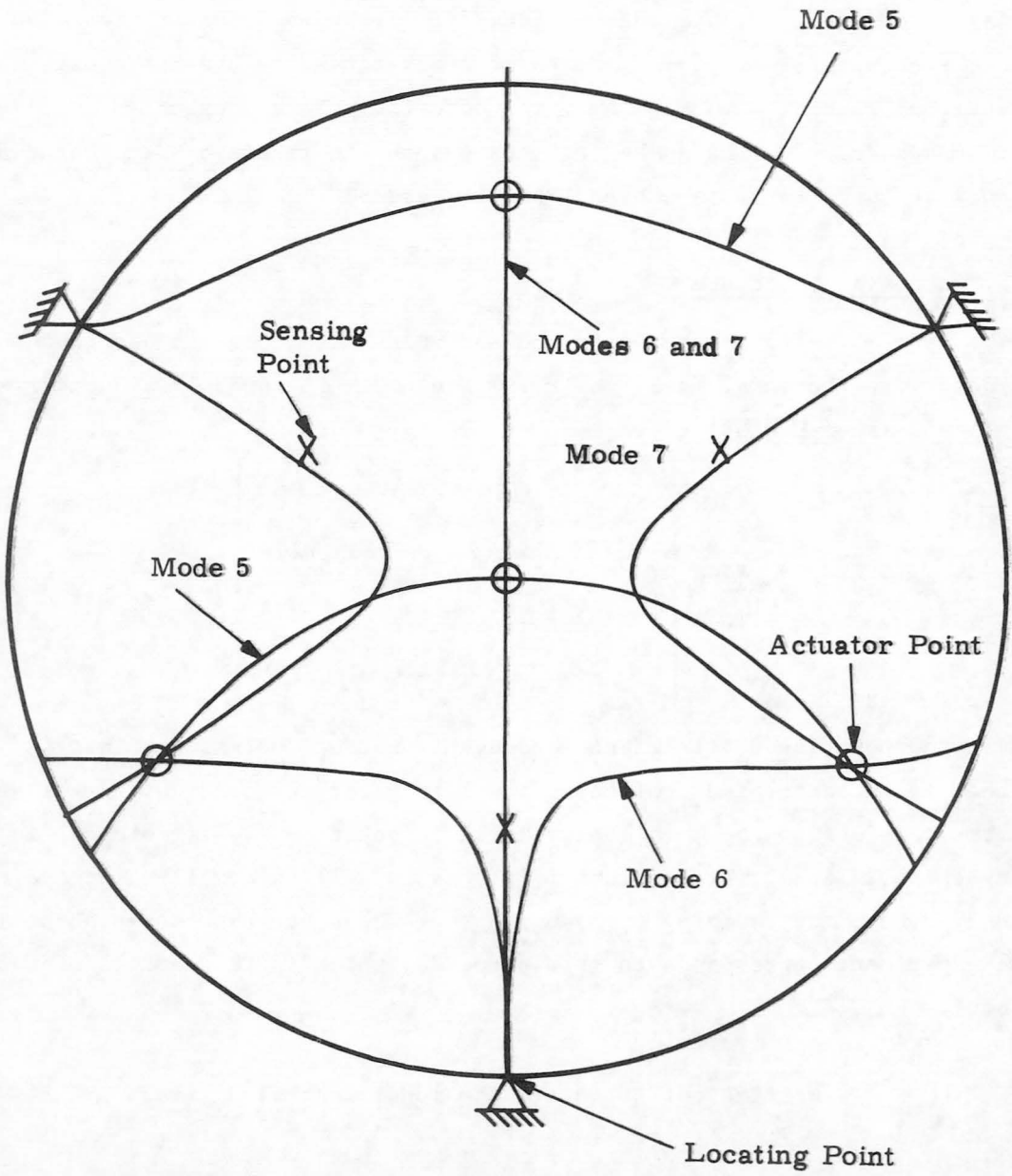


Figure 5-4. Superposition of Nodal Contours for Modes 5, 6, and 7

modes 1 through 4. It is then obvious from figure 5-4 that the circled points are the actuator locations. The three cross-marked points are chosen as additional sensing points. Thus, the actuator points chosen are 20, 17, 23, and 47 according to the numbering scheme shown in figure 5-5 and three additional sensor points are chosen at 6, 41, and 37.

5.3.2 Design Procedure

With the actuator and sensor points chosen it was then possible to determine the modal matrix U_N, (7x7 since N = 7) which is a submatrix of U_M (58x58 since M = 58) given as

$$U_M = \begin{bmatrix} u_1(1) & u_2(1) & \cdots & u_{58}(1) \\ u_1(2) & u_2(2) & \cdots & u_{58}(2) \\ \vdots & \vdots & & \vdots \\ u_1(58) & u_2(58) & \cdots & u_{58}(58) \end{bmatrix} \qquad (1)$$

where the notation $u_j(i)$ refers to conventional u_{ij} notation. That is, the number is in parentheses refers to the i-th point in question and the subscript number j refers to the j-th mode. Row 1 in equation (1) is column 1 in the conventional sense, while column 1 in equation (1) is row 1 in the conventional sense. Thus, for example, $u_{12} = u_{20,2} = u_2(20)$ since the chosen point 1 for the experiment corresponds to grid point 20, which is the center point of the mirror.

Written out in detail the modal matrix, U_M, is

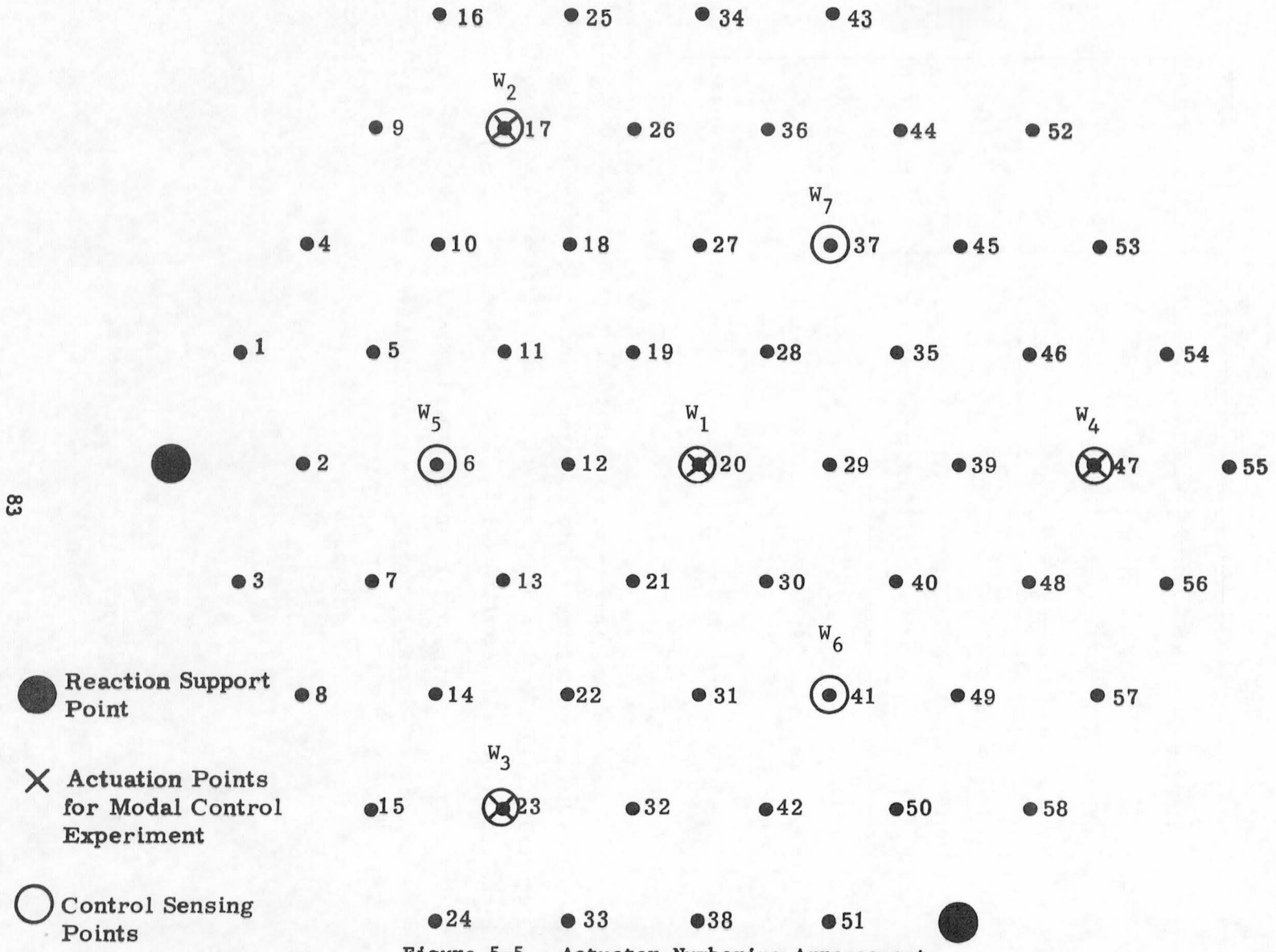


Figure 5-5. Actuator Numbering Arrangement

$$
U_M = \left[\begin{array}{cccc|ccc|c}
\multicolumn{4}{c|}{U_{NN}} & \multicolumn{4}{c}{U_{NR}} \\
u_1(20) & u_2(20) & u_3(20) & u_4(20) & u_5(20) & u_6(20) & u_7(20) & u_8(20)\ldots u_{58}(20) \\
u_1(17) & u_2(17) & u_3(17) & u_4(17) & u_5(17) & & & \\
u_1(23) & u_2(23) & u_3(23) & u_4(23) & u_5(23) & & & \\
u_1(47) & u_2(47) & u_3(47) & u_4(47) & u_5(47) & u_6(47) & u_7(47) & u_8(47)\ldots u_{58}(47) \\
\hline
u_1(6) & u_2(6) & u_3(6) & u_4(6) & u_5(6) & u_6(6) & u_7(6) & u_8(6)\ldots u_{58}(6) \\
u_1(41) & u_2(41) & u_3(41) & u_4(41) & u_5(41) & & & \\
u_1(37) & u_2(37) & u_3(37) & u_4(37) & u_5(37) & u_6(37) & u_7(37) & u_8(37)\ldots u_{58}(37) \\
\hline
u_1(1) & u_2(1) & u_3(1) & u_4(1) & u_5(1) & u_6(1) & u_7(1) & u_8(1)\ldots u_{58}(1) \\
u_1(2) & u_2(2) & u_3(2) & u_4(2) & u_5(2) & \vdots & \vdots & \vdots \quad \vdots \\
\vdots & \vdots & \vdots & \vdots & \vdots & \vdots & \vdots & \vdots \quad \vdots \\
u_1(58) & u_2(58) & u_3(58) & u_4(58) & u_5(58) & u_6(58) & u_7(58) & u_8(58)\ldots u_{58}(58) \\
\multicolumn{4}{c|}{U_{RN}} & \multicolumn{4}{c}{U_{RR}}
\end{array}\right] \qquad (2)
$$

The dotted lines refer to partitions that define, respectively, from top to bottom or left to right, actuator points. Comparing equation (1) and equation (2) yields a relation between the natural order in equation (1) and the actual order in equation (2) as shown in Table 5-1.

TABLE 5-1. POINT CORRESPONDENCE

Natural Order	Actual Order
1	20
2	17
3	23
4	47
5	6
6	41
7	37
etc.	etc.

The displacement vector $\bar{w}$ is related to the mode amplitude vector $\bar{c}$ by

$$\text{(a)} \quad \bar{w} = \underline{U}\,\bar{c} \quad \text{or}$$

$$\text{(b)} \quad \bar{c} = \underline{U}^{-1}\,\bar{w} = \underline{V}\,w \quad ; \quad \underline{V} = \underline{U}^{-1} \ (58 \times 58) \tag{3}$$

In accordance with the partition mode

$$\begin{aligned} \bar{C}_N &= V_{\underline{NN}}\,\bar{W}_N + V_{\underline{NS}}\,\bar{W}_s \\ \bar{C}_s &= V_{\underline{SN}}\,\bar{W}_N + V_{\underline{SS}}\,\bar{W}_s \end{aligned} \tag{4}$$

where $\bar{C}_N$ and $\bar{C}_s$ refer to the mode amplitude vectors for the actuator points and sensor (non-actuator) points, respectively. $\bar{W}_N$ and $\bar{W}_s$ refer to the actuator and sensor points, respectively. The $\underline{V}$ partition matrices are obtained from $\underline{V} = \underline{U}^{-1}$. By referring to Table 5-1 this establishes the submatrix V_{N+S} as

(5)

$$\underline{V_{N+S}} = \begin{bmatrix} & \underline{V_{NN}} & & & \underline{V_{NS}} & & \\ v_{1,20} & v_{1,17} & v_{1,23} & v_{1,47} & v_{1,6} & v_{1,41} & v_{1,37} \\ v_{2,20} & v_{2,17} & v_{2,23} & v_{2,47} & v_{2,6} & v_{2,41} & v_{2,37} \\ v_{3,20} & v_{3,17} & v_{3,23} & v_{3,47} & v_{3,6} & v_{3,41} & v_{3,37} \\ v_{4,20} & v_{4,17} & v_{4,23} & v_{4,47} & v_{4,6} & v_{4,41} & v_{4,37} \\ \hline v_{5,20} & v_{5,17} & v_{5,23} & v_{5,47} & v_{5,6} & v_{5,41} & v_{5,37} \\ v_{6,20} & v_{6,17} & v_{6,23} & v_{6,47} & v_{6,6} & v_{6,41} & v_{6,37} \\ v_{7,20} & v_{7,17} & v_{7,23} & v_{7,47} & v_{7,6} & v_{7,41} & v_{7,37} \\ & \underline{V_{SN}} & & & \underline{V_{SS}} & & \end{bmatrix}$$

From numerical data,

$$(a)\quad V_{\underline{NN}} = \begin{bmatrix} -4.3155E\text{-}3 & -7.9662E\text{-}1 & -8.0690E\text{-}2 & 8.6487E\text{-}1 \\ 2,1392E\text{-}3 & -5.4387E\text{-}1 & 9.6133E\text{-}1 & -4.1127E\text{-}1 \\ -5.7397E\text{-}1 & -5.4445E\text{-}1 & -5.4421E\text{-}1 & -5.5683E\text{-}1 \\ -7.8007E\text{-}1 & 4.6961E\text{-}1 & 4.6960E\text{-}1 & 4.6991E\text{-}1 \end{bmatrix}$$

$$(b)\quad V_{\underline{NS}} = \begin{bmatrix} -1.8454E\text{-}1 & 1.6137E\text{-}1 & 1.2446E\text{-}2 \\ 8.7841E\text{-}2 & 1.1592E\text{-}1 & -1.9782E\text{-}1 \\ -4.5913E\text{-}1 & -4.6118E\text{-}1 & -4.6122E\text{-}1 \\ -4.2135E\text{-}1 & -4.2454E\text{-}1 & -4.2460E\text{-}1 \end{bmatrix} \qquad (6)$$

$$(c)\quad V_{\underline{SN}} = \begin{bmatrix} -1.4855E\text{-}3 & -4.3910E\text{-}4 & -4.3316E\text{-}4 & 6.8879E\text{-}3 \\ -1.1527E\text{-}5 & -1.2895E\text{-}3 & -1.2521E\text{-}3 & -9.0923E\text{-}6 \\ -2.5437E\text{-}5 & 4.8284E\text{-}3 & -4.7930E\text{-}3 & 2.4387E\text{-}5 \end{bmatrix}$$

$$(d)\quad V_{\underline{SS}} = \begin{bmatrix} -7.7551E\text{-}1 & 3.8640E\text{-}1 & 3.8551E\text{-}1 \\ 1.61898E\text{-}3 & -1.8611E\text{-}1 & 1.84474E\text{-}1 \\ -1.02063E\text{-}3 & -6.4466E\text{-}1 & 6.4564E\text{-}1 \end{bmatrix}$$

The physical realization of a coefficient set can be obtained by the op-amp resistor network configuration shown in figure 5-6. From figure 5-6, the output voltage obtained is

$$\left[V_i = -R_F \sum_j \left(\frac{a_{ij}}{R_F} \right) w_j^- + \frac{V_1}{R_F} \right] \qquad (7)$$

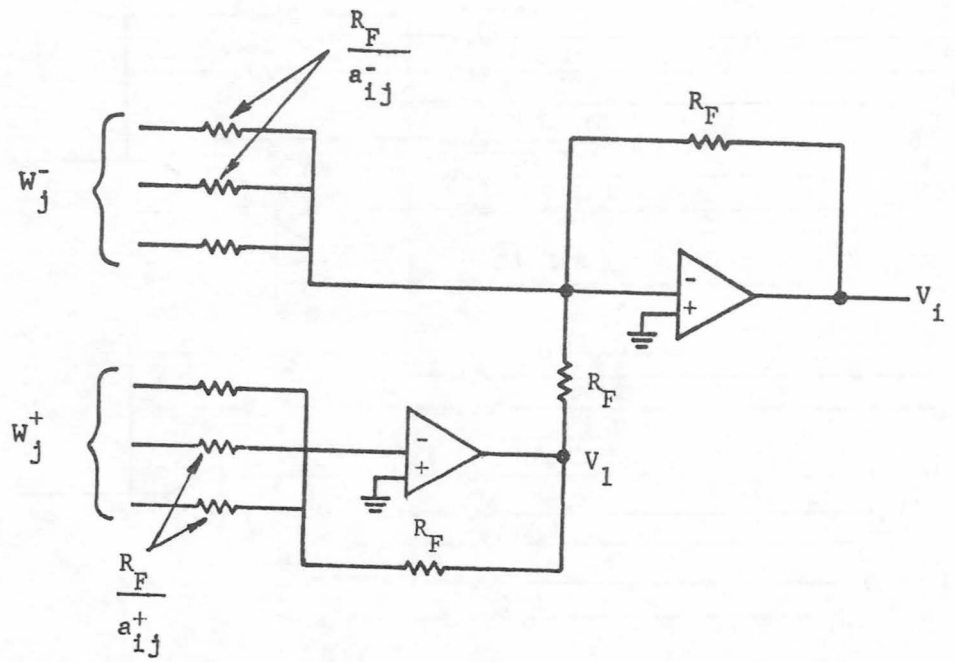


Figure 5-6. OP-AMP Resistor Network Realization of Controller

where the minus and plus superscripts refer to the negative and positive coefficients, respectively. The displacement inputs w_j really are proportional phase detector output voltages. Since.

$$V_1 = -R_F \sum_j \left(\frac{a_{ij}^+}{R_F} \right) w_j^+ \tag{8}$$

then

$$V_i = -\Sigma a_{ij}^- w_j^- + \Sigma a_{ij}^+ w_j^+ \tag{9}$$

or

$$V_i = \sum_{j=1}^{M} a_{ij} w_j \tag{10}$$

thus, for a suitably scaled feedback resistor, R_F, the input resistor values are essentially proportional to the reciprocal of coefficients of the $\underline{V}$ matrices of equation (6). The resulting mode analyzer realization is shown in figures 5-7 and 5-8.

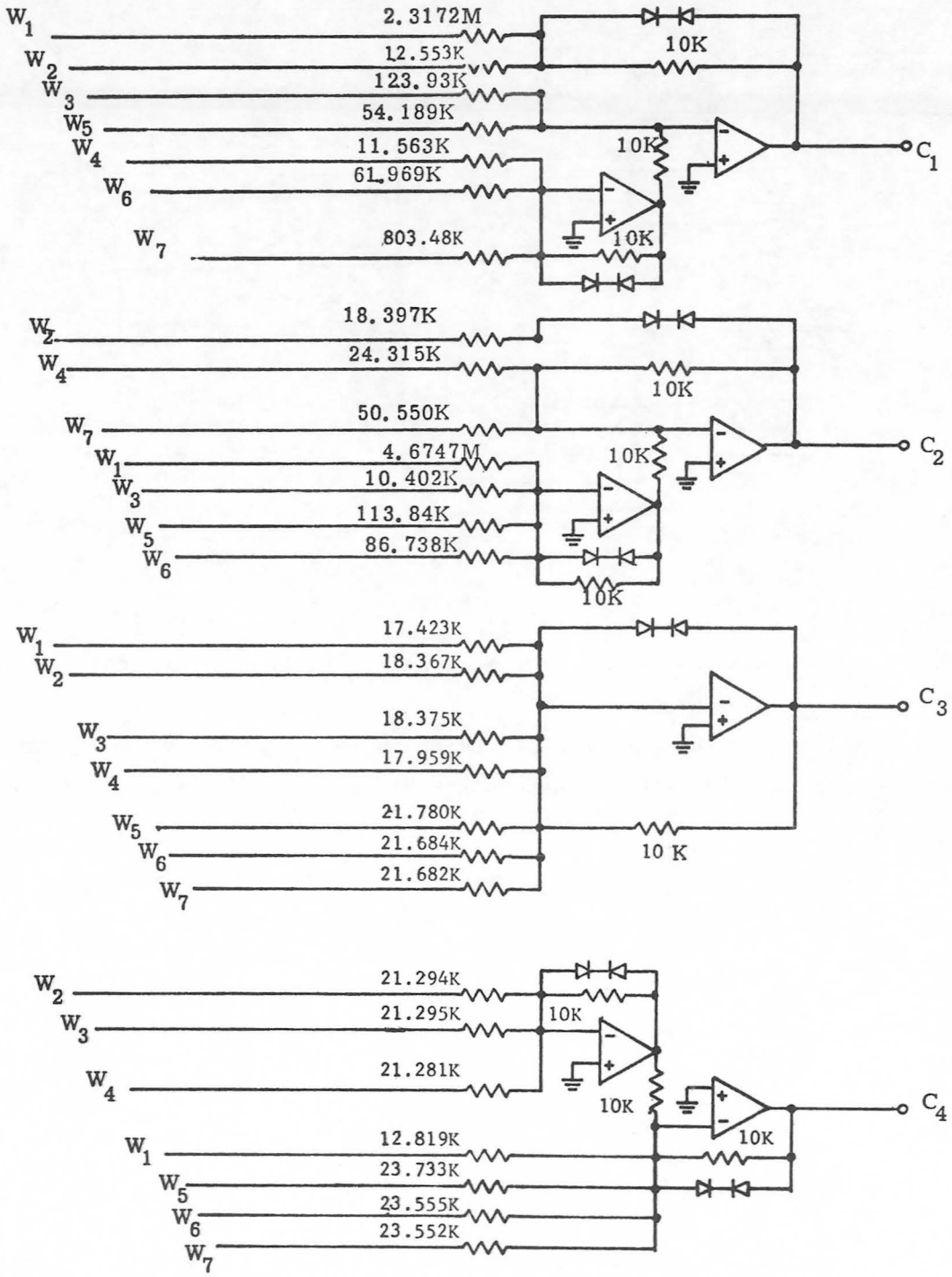


Figure 5-7. Mode Analyzer, $\underline{U_N}^{-1}$ (Controlled Modes, $\overline{C}_N = V_{\underline{NN}}\,\overline{W}_N + V_{\underline{NS}}\,\overline{W}_S$)

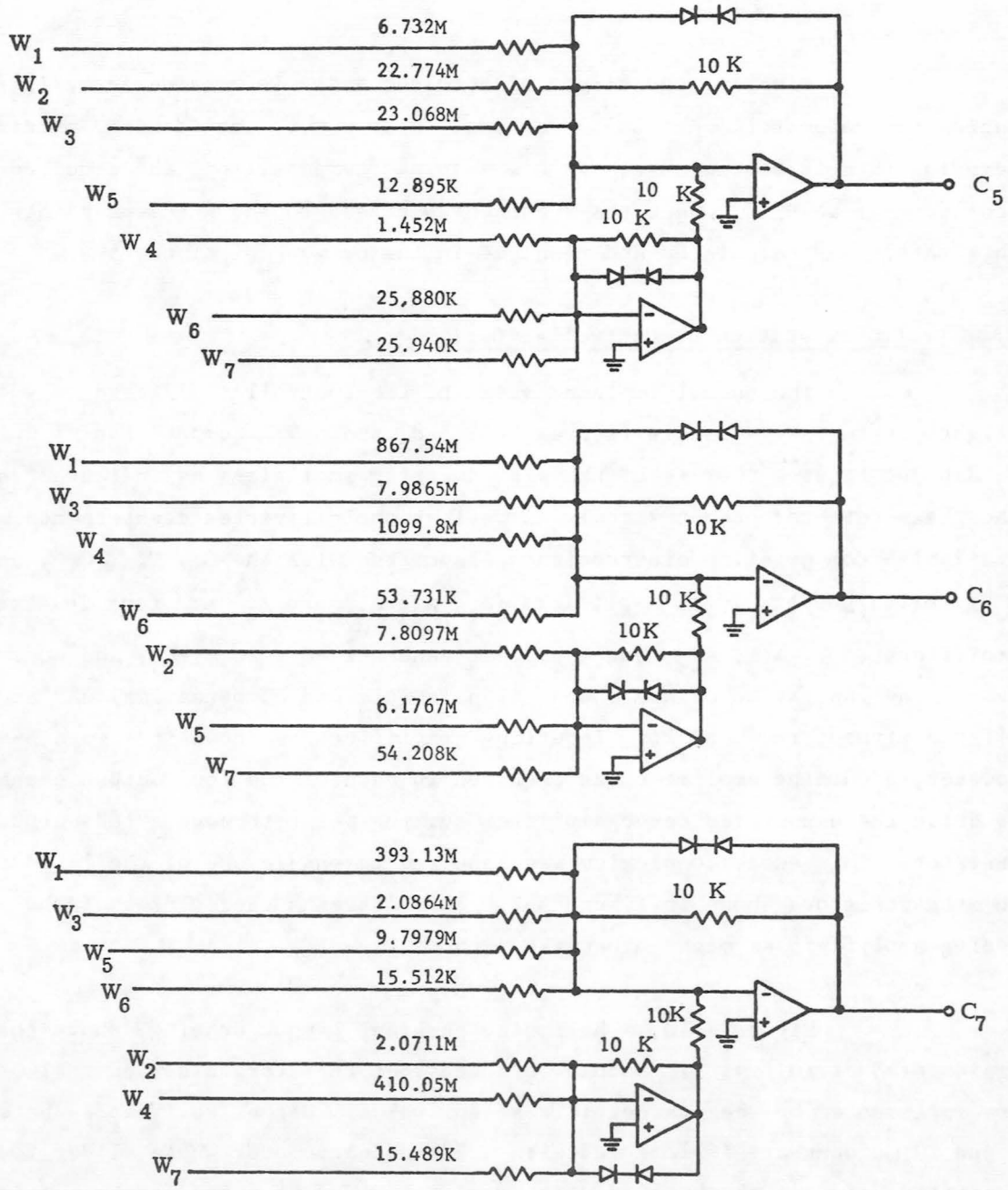


Figure 5-8. Mode Analyzer (Uncontrolled Modes, $\overline{C}_S = V_{\underline{SN}}\,\overline{W}_N + V_{\underline{SS}}\,\overline{W}_S$)

Finally, the effect of actuator pads* is considered by introducing the pad matrix, $\underline{H} = \underline{G}\underline{U}^T$. For small pads $\underline{G} = 1$, the identity matrix. Assuming this to be the case, $\underline{H} = U^T$. For pad compensation, the required controller must be H_N^{-1}, where the subscript N refers to the actuator points only. This matrix was calculated and resulted in the network of figure 5-9.

5.3.3 Implementation of Controller Design

The actual implementation of the controller differed only slightly from that shown in figures 5-7, 5-8, and 5-9. Computation of C_1 thru C_7 did not require the use of the six inverting amplifiers as indicated, since the phase detector output signals as well as their inverted counterparts were available from existing electronics. Associated with the C_1, C_2, C_3, and C_4 generating operational amplifiers (A_1, A_2, A_3, and A_4) are four inverting amplifiers (A_{-1}, A_{-2}, A_{-3}, and A_{-4}) that generate $-C_1$, $-C_2$, $-C_3$, and $-C_4$. Hence, the generation of subsequent signals (via pad compensation) was accomplished without the need for "inverting" amplifiers as shown in figure 5-9. However, a summing amplifier was required in each of the four output channels to drive the associated servo amplifier summing point through a 10K output resistor. This added complexity was required to enable use of the large value summing resistors shown in figure 5-2. This prevents overloading of the preceding amplifiers as might otherwise occur.

Figure 5-10, a half size phusical layout drawing, shows the implemented circuitry. It should be noted that resistor values up to 140K are implemented by the nearest 1% resistor value. Higher resistances between 1 and 10 megohms are implemented with a 50K potentiometer whose slider feeds a portion, 1/x, of the applied voltage signal, $\pm W_i$, to a one megohm summing resistor. This implements an equivalent summing resistor value of X megohms. The same approach is used to obtain the equivalent of summing resistors between 10 and 100 megohms; however, here a 10 megohm fixed resistor is used with a 500K potentiometer. Even higher equivalent summing resistors (>100M) are

*J.F. Creedon and A.G. Lindgren, Op. Cit.

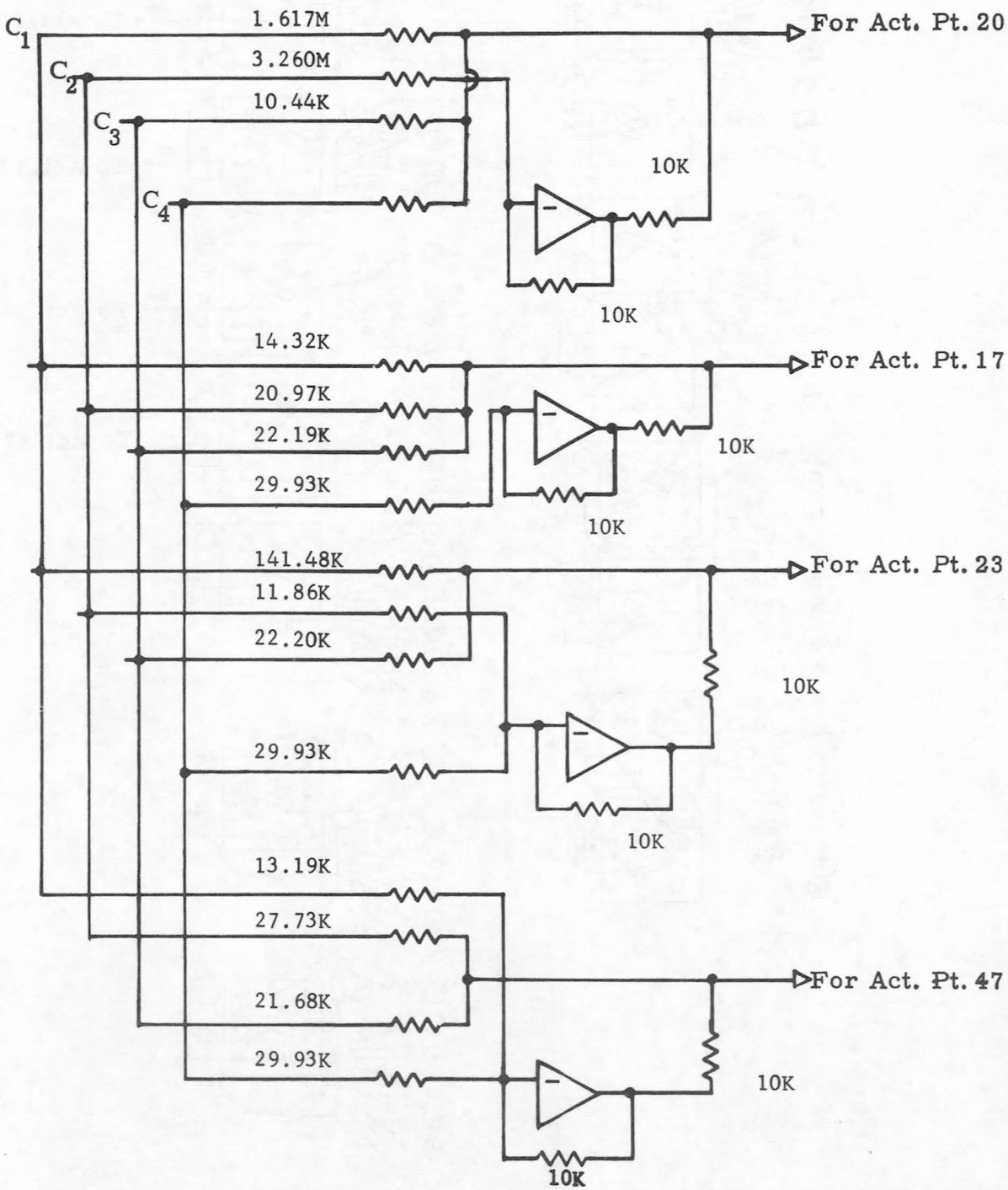


Figure 5-9. Pad Compensator, H_N^{-1}

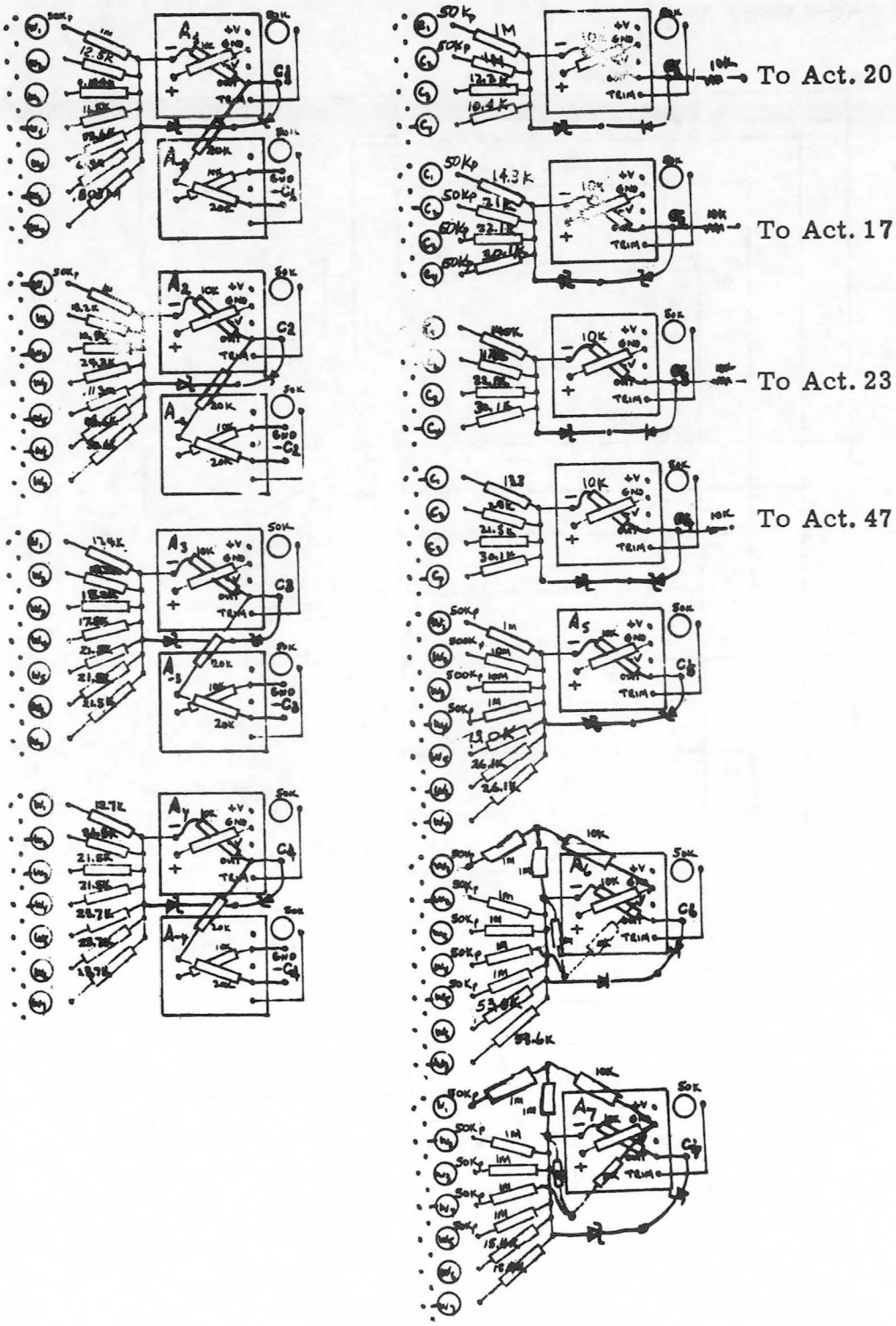


Figure 5-10. **Layout of Modal Controller**

obtained in essentially the same manner. There a 50K potentiometer feeds a 100:1 divider whose output voltage drives a one megohm fixed resistor. Cermet potentiometers capable of 1% adjustment are used for compatibility with the 1% fixed resistor covering the <140K range.

It should be noted that the small circles labelled $\pm W_i$ and $\pm C_i$ represent possible locations for the potentiometers associated with summing resistors. A value (either $50K_p$ or $500\ K_p$) adjacent to the location indicates that a (50 or 500K) potentiometer was included to drive the resistor located to the right. In cases where no value is shown adjacent to the small circle location, a potentiometer mounting hole but no potentiometer was provided. In these cases, the input signals were applied directly to the summing resistor to the right. All amplifiers except those used for signal inversion feature two zener diodes paralleling the feedback resistor, to provide clipping action in all cases at about 9 volts.

The controller as finally breadboarded for experimental testing is shown in figure 5-11. The input and output wires were cabled to connectors that mate with the existing connectors at the phase detector outputs and servo amplifier inputs so that the unit can be inserted into or removed from the system quickly and conveniently.

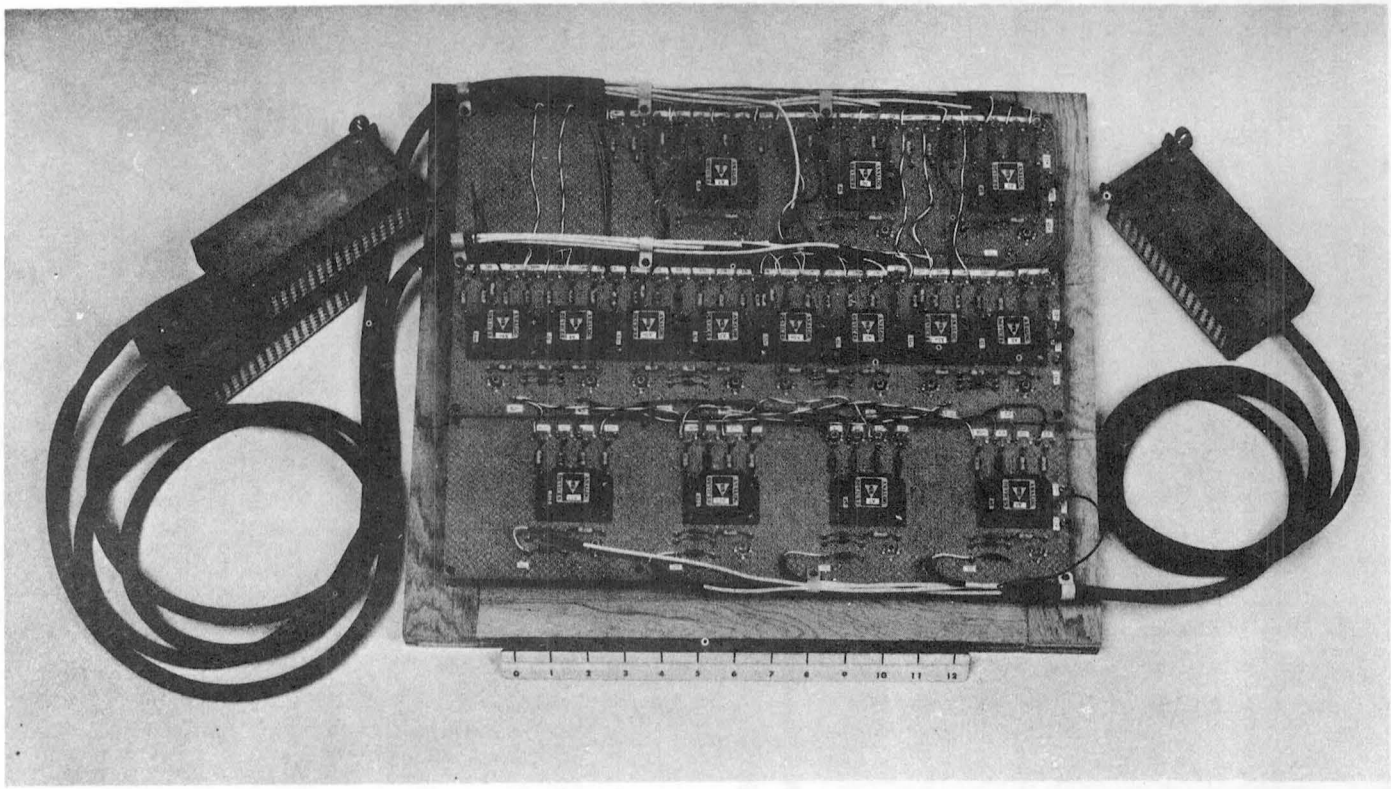


Figure 5-11.Four Actuator Modal Controller Breadboard Unit

5.3.4 Experimental Results with Modal Controller

The modal controller was tested by introducing errors into the previously aligned, 30-inch mirror and then removing as much as possible of the error introduced, with the modal controller. The relative amplitudes of the modal error signals produced by the uncontrolled error were observed and compared with the modal amplitudes predicted analytically for the specific error introduced. The modal amplitudes remaining after closed loop correction were measured. The time responses of the system were observed and the change in forces required to effect correction were recorded. The remanent error after correction was also compared with the remanent error produced by the same four actuators in parallel closed loop operation without the modal controller.

The results of the measurements are described in the following pages for two different error disturbances: one, a point force error introduced by a single actuator applying a force against the mirror to distort it; and two, a spherical error introduced by changing the axial distance between the mirror and the figure sensor.

The point force was exerted at actuator number 28 (see figure 5-5). This is an uncontrolled point halfway between a controlled point (actuator number 20) and sensor point (actuator number 37).

The errors developed as a function of the force applied, without correction, are shown in figure 5-12. The phase detector outputs are numbered W_1 through W_7 corresponding to the seven sensor points. The modal controller outputs, which should be proportional to the amplitude of the first seven natural modes contained in the mirror deformation are numbered C_1 through C_7. The relative slopes of C_1 through C_7 are compared in Table 5-2 for the measured values and the predicted values and show good correlation.

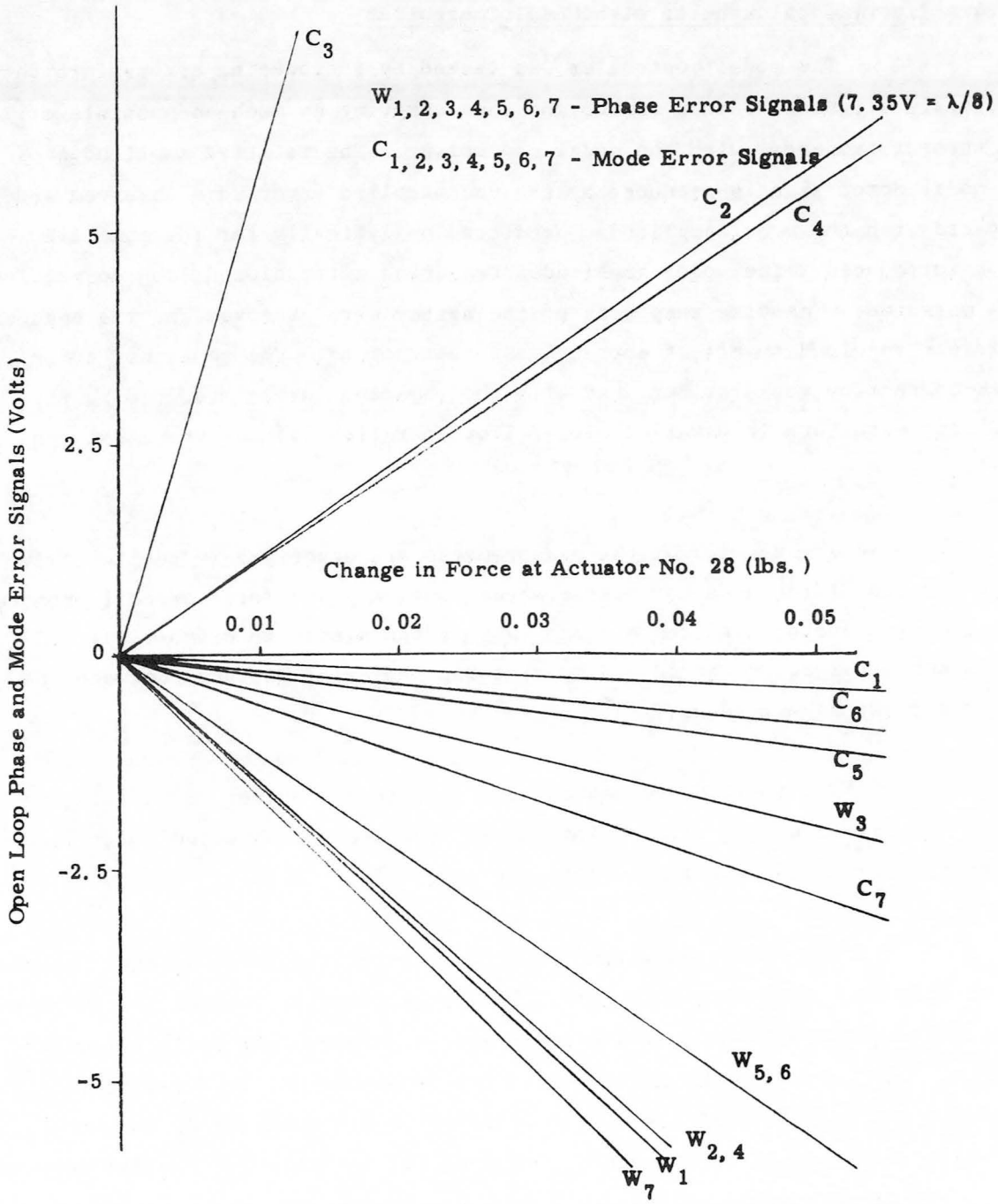


Figure 5-12. Open Loop Phase and Mode Errors as a Function of Force Applied at Uncontrolled Actuator No. 28

TABLE 5-2

	Measured	Calculated
C_1	1.0	1.0
C_2	-10.5	-16.4
C_3	-52.0	-52.6
C_4	-10.0	- 6.12
C_5	2.0	1.73
C_6	1.5	0.83
C_7	5.2	2.89

The phase detector outputs and the modal controller outputs after closed loop correction for the point force at actuator 28 are shown in figure 5-13. Since the phase detector outputs are only linear up to errors of 1/8 wavelength, the system can only be expected to operate properly within this limit. It is interesting to note, however, as shown in figure 5-13, that the system operates stably, if not accurately, for errors greater than 1/8 wavelength up to 3/8 wavelength amplitude. As expected, modal controller outputs C_1 through C_4 are nulled identically. The change in forces generated in the four actuators to maintain alignment are also shown in figure 5-13.

The mirror deformation introduced without closed loop control for an applied force of 0.175 pounds at actuator number 28 is shown in figure 5-14(a). Figure 5-14(b) shows the residual error after nulling C_1 through C_4 with the modal controller. For comparison, figure 5-14(c) shows the residual error after nulling the four actuators using the straight parallel control loops.

The errors developed without active correction as a function of change in axial spacing between figure sensor and mirror are shown in figure 5-15.

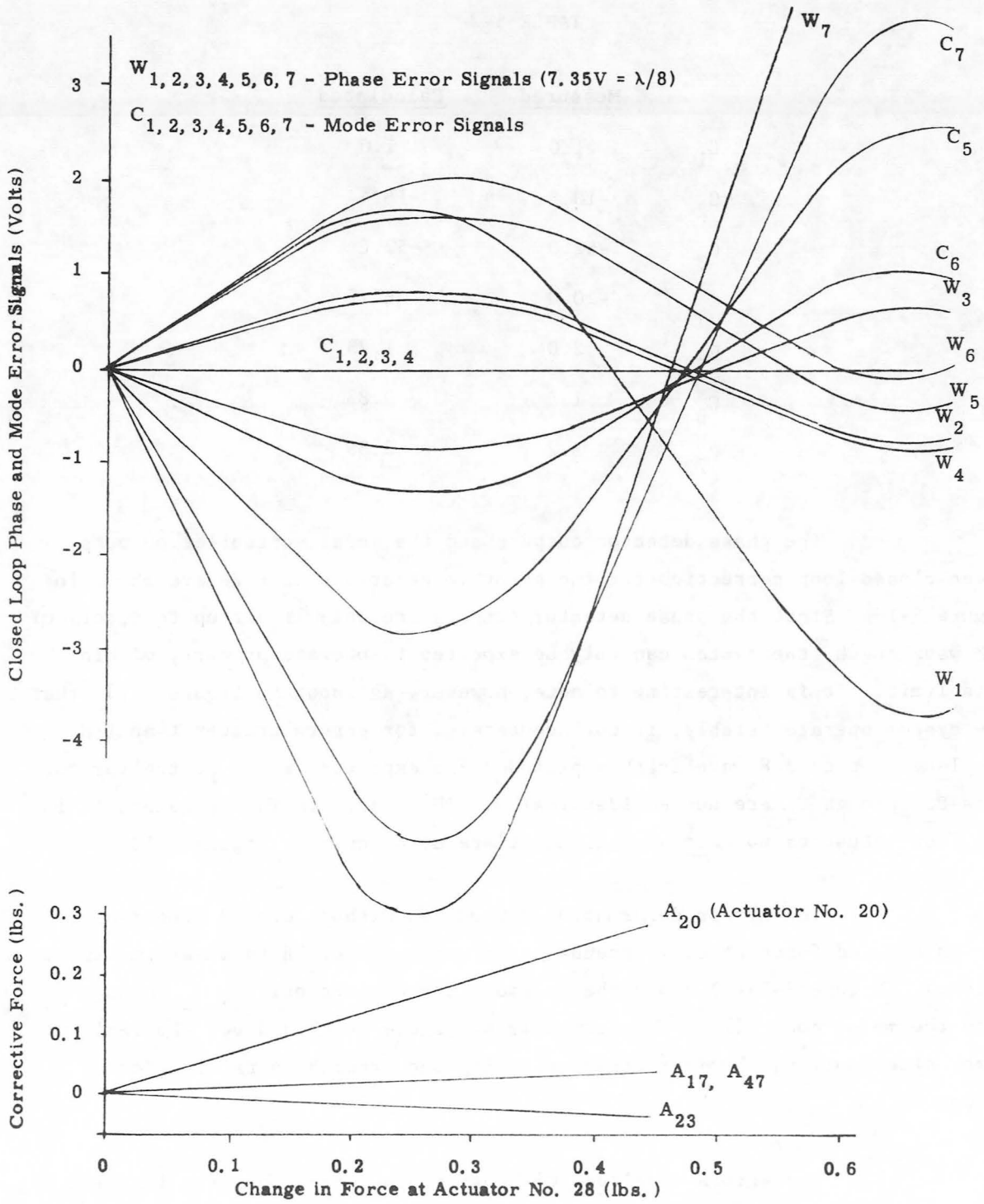
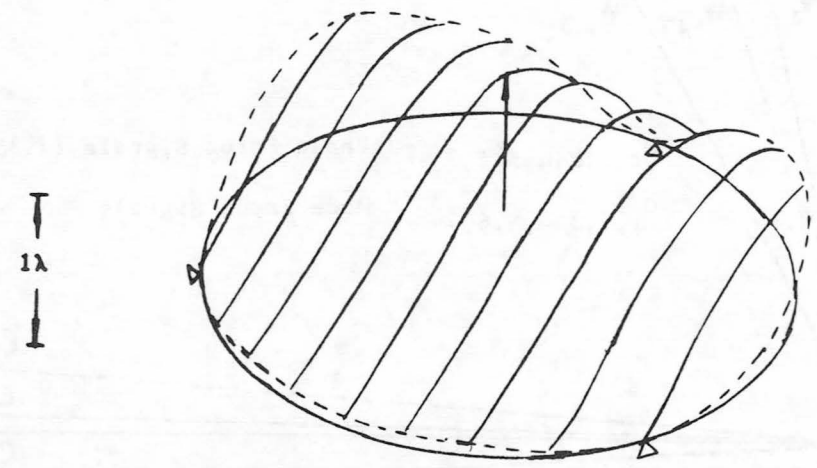
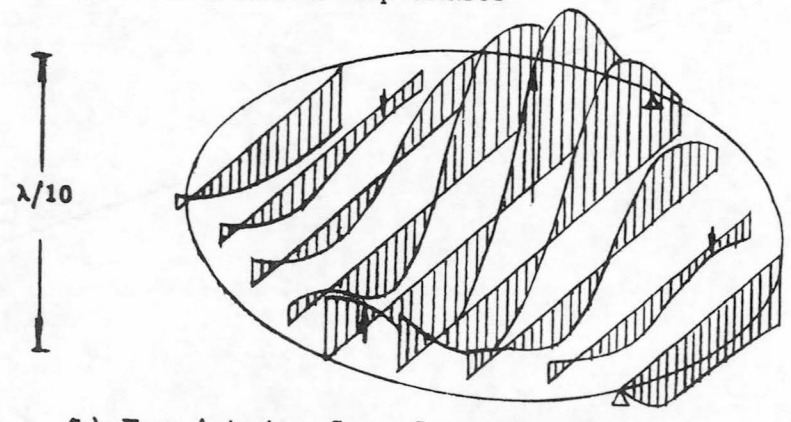


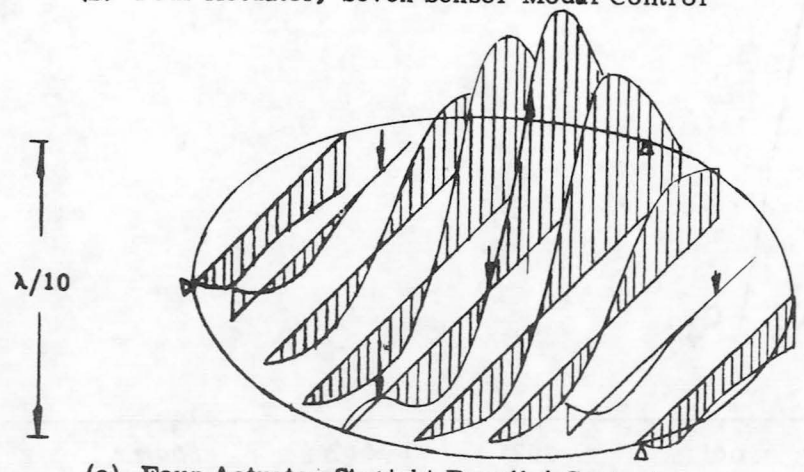
Figure 5-13. Phase and Mode Errors and Corrective Forces with Closed Loop Corrections for Point Force Error



(a) Without Closed Loop Control



(b) Four Actuator, Seven Sensor Modal Control



(c) Four Actuator Straight Parallel Control

Figure 5-14. Mirror Deformation Produced by 0.175 lb. Force Applied by Actuator No. 28.

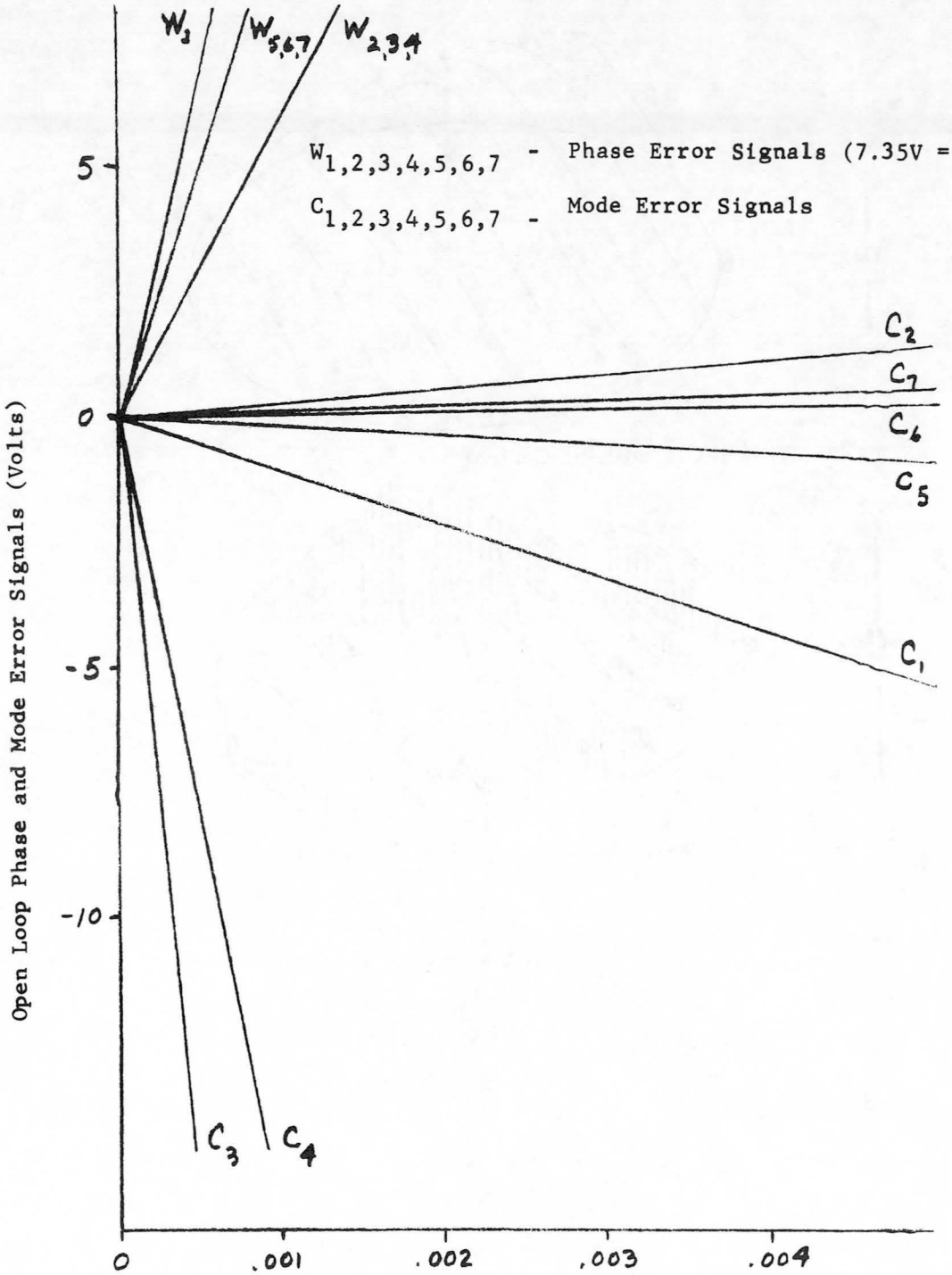


Figure 5-15. Open Loop Phase and Mode Errors as a Function of Axial Spacing Between Mirror and Figure Sensor.

The phase detector outputs, the modal controller outputs, and the actuator forces developed after closed loop correction are shown in figure 5-16.

The mirror deformation introduced without closed loop correction for a change of 0.003-inch in axial spacing between the mirror and figure sensor is shown in figure 5-17(a). Since the error is axially symmetrical, a single diameter profile is shown. Figure 5-17(b) shows the residual error with modal control and for comparison figure 5-17(c) shows the residual error for the straight parallel closed loop control.

Both cases shown exhibit improvement in RMS figure for the modal controller with four control actuators and seven sensing points, over the straight parallel control with four actuators and four sensing points. The larger the number of sensing points used, the better the fit should be to the reference wavefront, for any given number of actuators.

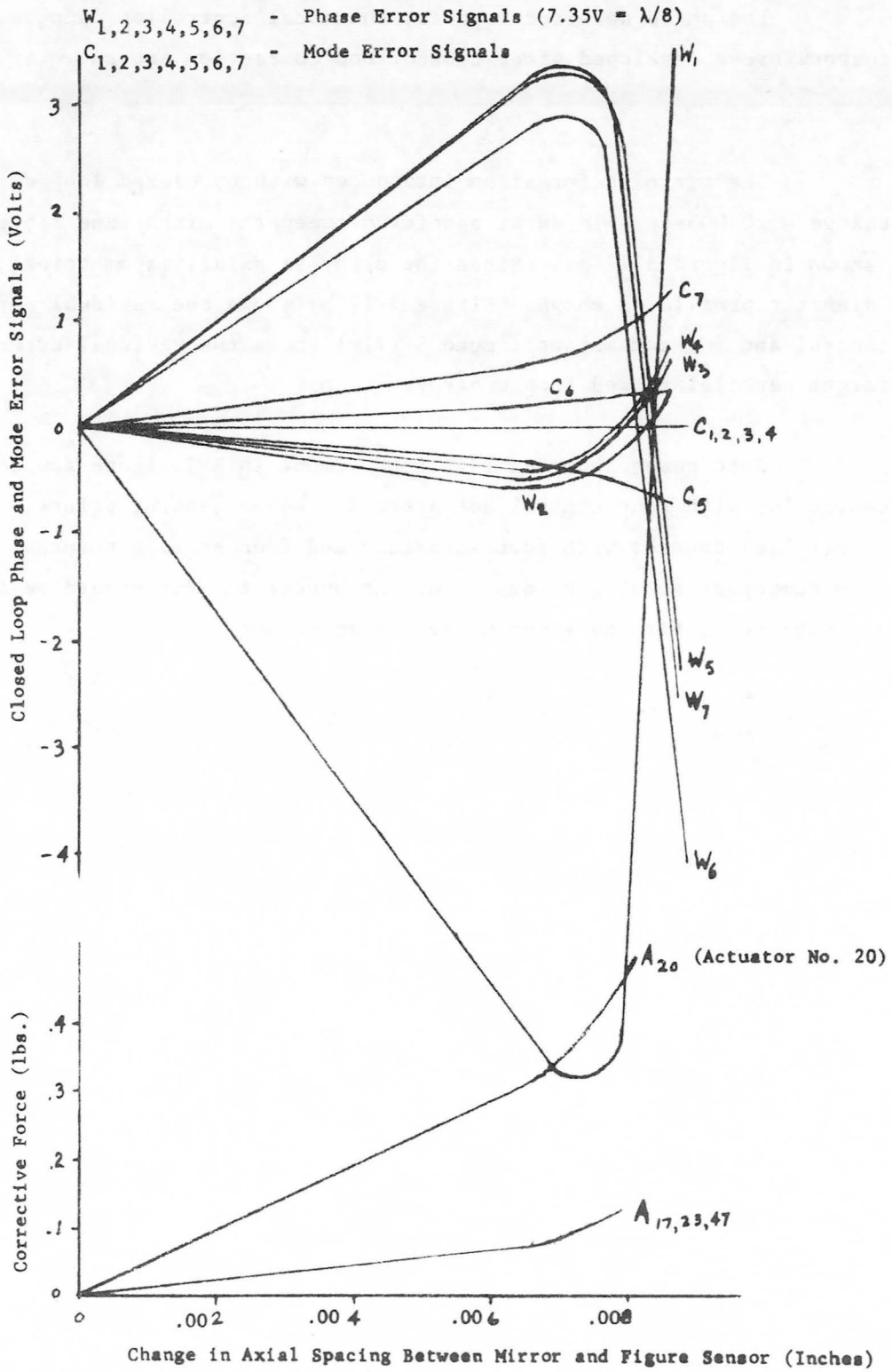
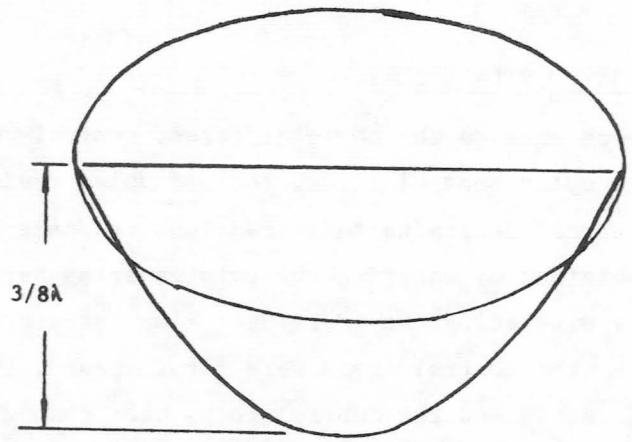
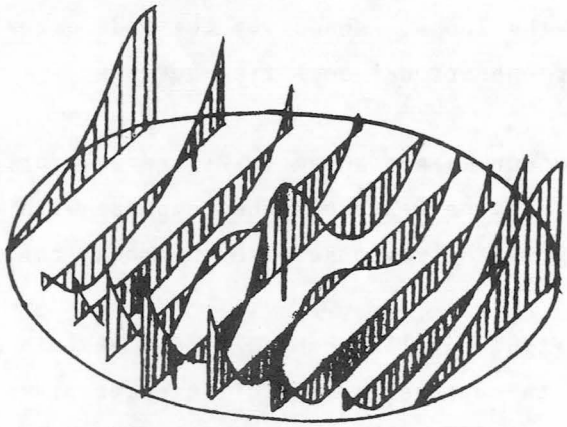


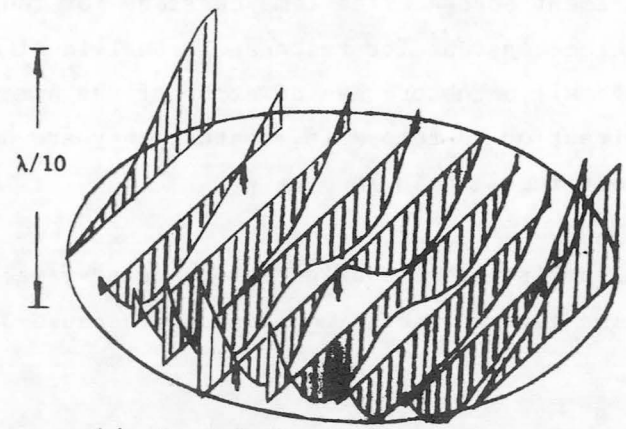
Figure 5-16. Phase and Mode Errors and Corrective Forces with Closed Loop Correction for Axial Error.



(a) Without Closed Loop Control



(b) Modal Control with Four Actuators



(c) Straight-Parallel Control with Four Actuators

Figure 5-17. Mirror Figure Error Produced by 0.003" Change in Axial Spacing Between Mirror and Figure Sensor

6.0 TRANSIENT RESPONSE TO STEP ERRORS

Tests were made on the three different control configurations; the straight-parallel coupled control loops, the uncoupled feedforward network, and the modal controller, to determine their transient response to step errors. The step errors were obtained by changing the axial spacing between the mirror and figure sensor or by displacing the individual flex actuators by various amounts. When possible, the control loops were first opened, the step displacement errors were created and the control loops were then closed. The responses were measured and recorded at the output of the phase detectors from the time of closure of the loops, except for the mode errors which were read at the modal controller operational amplifier outputs.

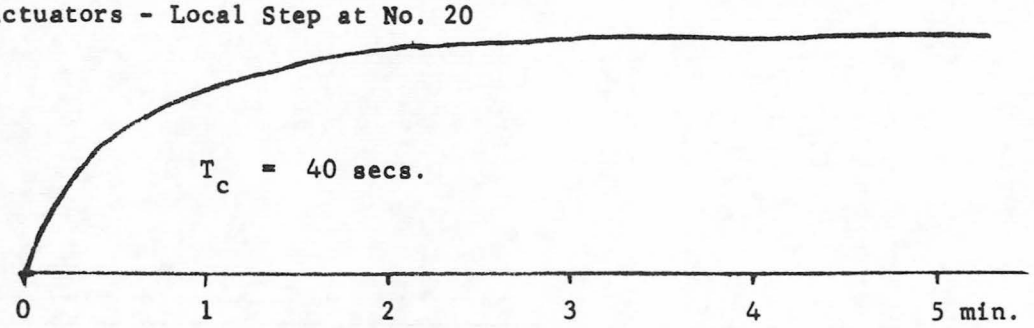
Response curves are shown in Figure 6-1 for the straight-parallel coupled control loops. Figure 6-2 shows the response with the feedforward network, and Figure 6-3 shows the response with the modal controller.

The straight-parallel control loops exhibit a uniform response to an axial step error in contrast to the differences observed between the responses of actuators at different locations when the error was due to individual actuator displacement errors. The time constant for the axial step is much shorter than the time constant for response to individual actuator displacement errors because all actuators see an error of the same sign and move together in the same direction to remove it, so that they are helping each other, giving an apparent increase in loop gain.

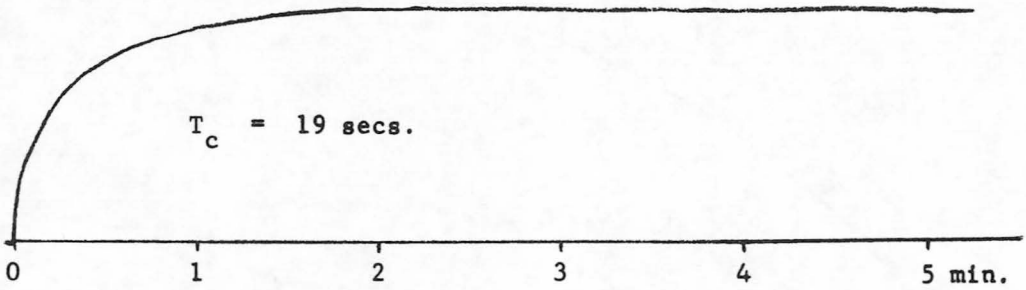
Parallel control loop configurations using fewer actuators spaced further apart also give shorter time constants because of higher effective loop gains.

In contrast, the response of the feedforward network is not only uniform from one actuator to another for individual actuator errors, but it is essentially the same for axial errors. This is because the gain has been normalized and decoupled and the actuators are in effect unaware of whether the adjacent actuators are aiding or opposing them.

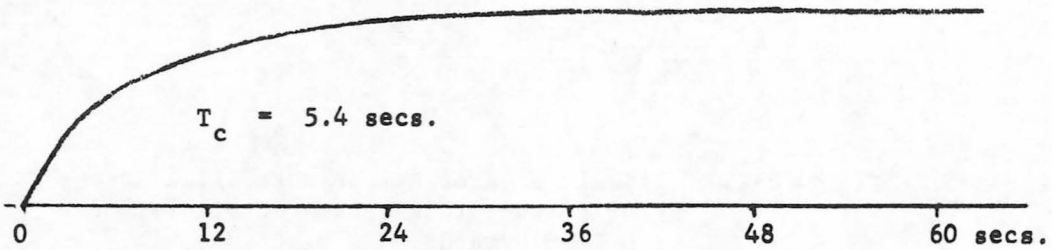
58 Actuators - Local Step at No. 20



58 Actuators - Local Step at No. 16



58 Actuators - Axial Step (Typical)



4 Actuators - Axial Step (Typical)

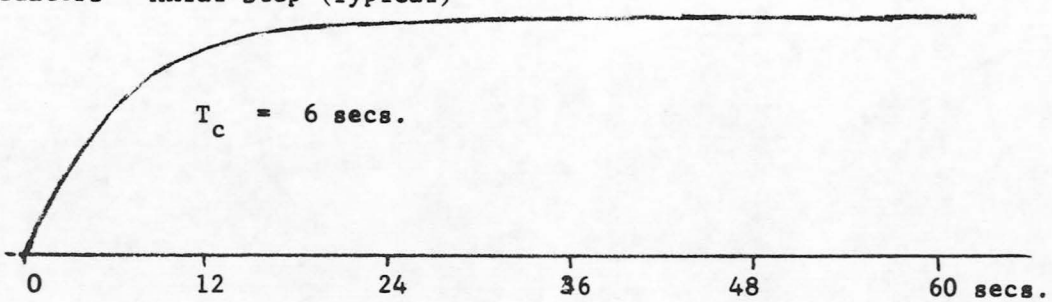


Figure 6-1. Actuator Response to Step Errors with Straight-Parallel Coupled Loops

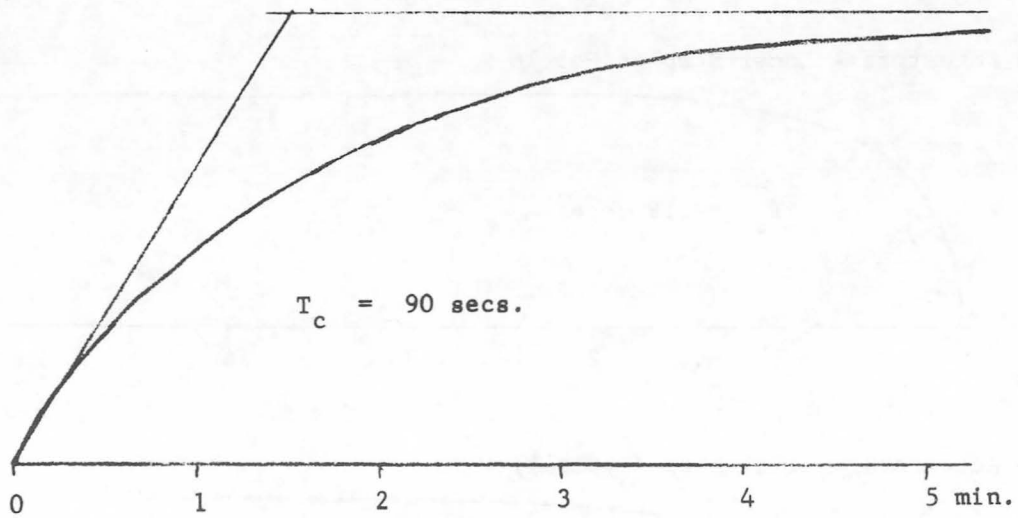


Figure 6-2. Typical Actuator Response to Axial Step Error or Individual Actuator Displacement with Feedforwards.

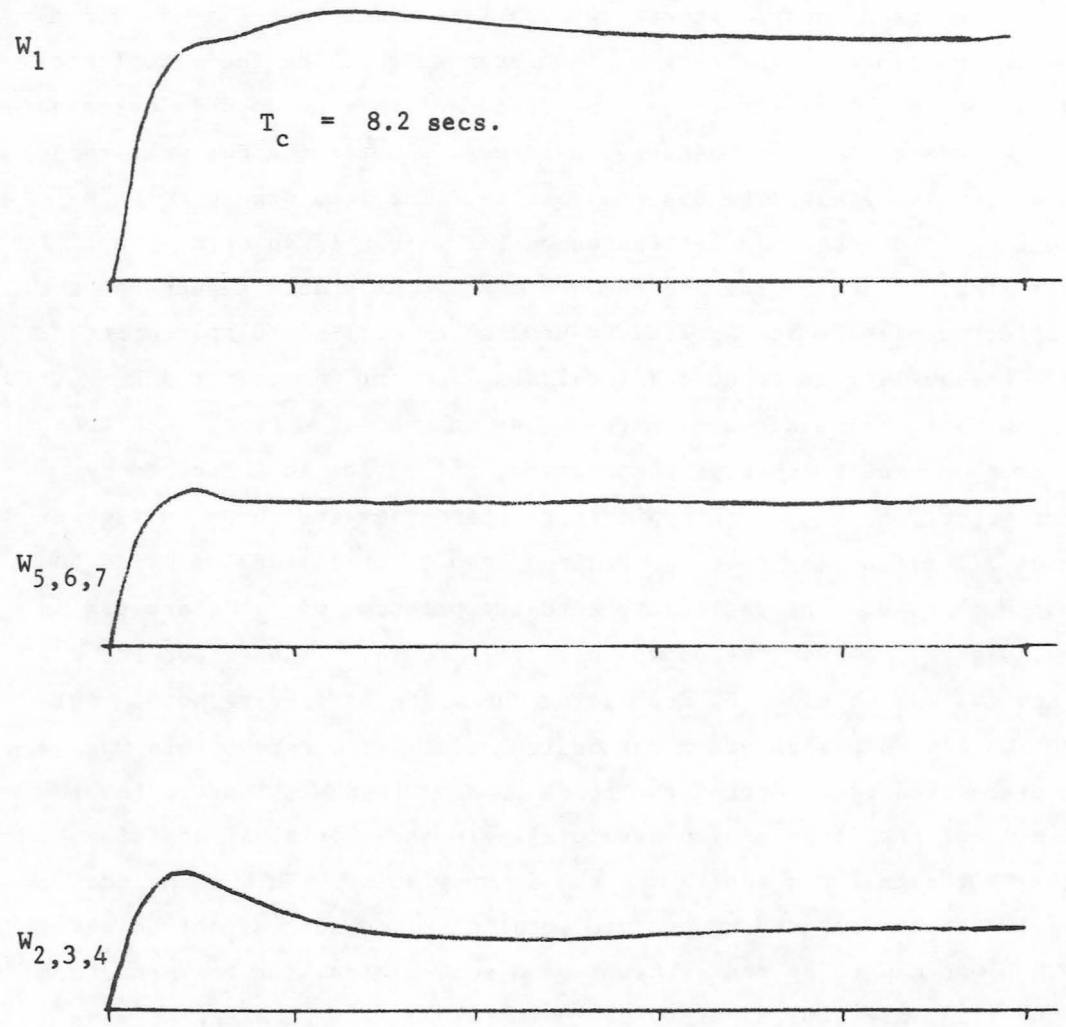
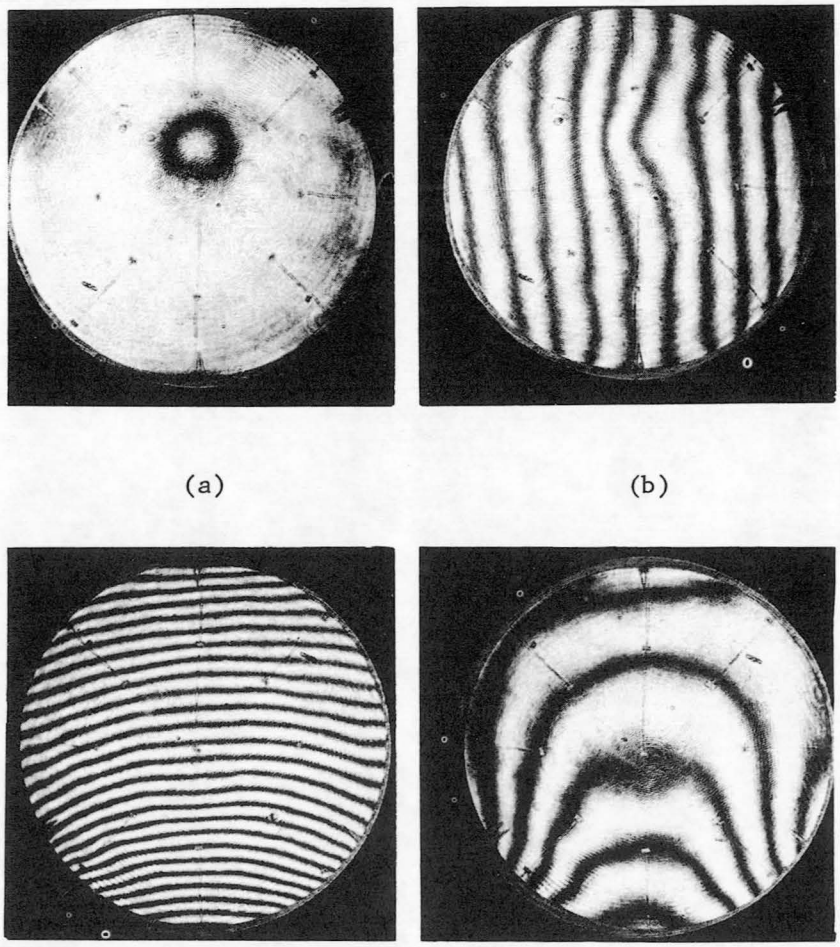


Figure 6-3. Actuator Response to Axial Step Error with Modal Controller

7.0 LOCALIZATION OF FEEDFORWARDS

The feedforward network is a resistive matrix designed to compensate for interactions in the deformable mirror so that the individual control loops can operate independently. The design of this network is described in detail in Reference 1. The objective here was to determine how well the design values come to giving the desired results. The feedforward network is designed to give a localized deflection on the mirror if an error signal is applied to a single input of the feedforward matrix, so that a measure of the network's effectiveness is its ability to produce a localized displacement. The test for the ability to produce a local displacement was to put a DC voltage at the input of the feedforward matrix, one channel at a time, with the control loops open, and to observe the resultant deflection as indicated by the interferometer output. Some typical interferograms are shown in figure 7-1. Figures 7-1(a) and (b) show the desired result for a signal applied to control loop number 40. The deflection actually produced with the network as originally designed, however, is shown in 7-1(c) and (d). The effect shown in 7-1(a) and (b) was obtained by decreasing the value of driving point resistance approximately 30 percent from the design value. The reason this was necessary was discovered by observing the force changes in the actuators involved. The second ring of actuators stayed essentially in their original positions even though a six volt signal was applied to the driving point. This means that the full set of 19 forces designed to produce local displacement was not being applied. This was caused by the actuator dead zones which, for the actuators in the second ring, are equivalent to approximately ±1/200 wavelength. The driving point resistance correction made to obtain 7-1(a) and (b) gives essentially a single ring (7 actuators) constellation of forces for each control loop instead of the 19 point group originally designed. The localization obtained with this more limited compensation is, however, very good as can be seen in figure 7-1(a) and (b), and in the light of hindsight it is evident that the 10 point arrangement was overcompensation even if the dead zone phenomenon did not exist.

The dead zones are approximately twice as large with the feedforward network as with the straight parallel control because the minimum driv-



(a) (b)

(c) (d)

Figure 7-1. Interferograms Showing Localized Deflections Produced By Feedforward Network (a) and (b) After Decreasing Driving Point Resistance to Produce a Seven Point Configuration of Forces (c) and (d) With Original Design Values for 19 Point Force Configuration

ing point resistances are at least twice as large. The dead zones for the straight parallel control loops are equivalent to ±1/400 wavelength or less. Some dead zone is usually desireable to prevent overworking the actuator motors. If friction did not provide a dead zone it might be necessary to provide a threshold control.

An attempt was made to measure the stiffness matrix values by displacing a single actuator and measuring the change in actuator forces required to maintain all the other points aligned. A typical set of forces is shown in figure 3-2. The dead zones here again make it difficult to obtain a set of readings that would be accurate enough to improve on the analytical determination.

8.0 REFERENCES

1. H.J. Robertson: Development of an Active Optics Concept Using a Thin Deformable Mirror, Perkin-Elmer Corp., Norwalk, Conn., NAS CR-1593.

2. J.F. Creedon and A.G. Lindgren: Control of the Optical Surface of a Thin Deformable Primary Mirror with Application to an Orbiting Astronomical Observatory, 3rd IFAC Symposium on Automatic Control in Space, held in Toulouse, France, March 2 through 6, 1970.

3. Evaluation of Multipoint Interaction in the Design of a Thin Diffraction-Limited Active Mirror, IEEE Transactions on Aerospace and Electronics Systems; Vol. AES-5, No. 2, March 1960.

APPENDIX A - DERIVATION OF MIRROR SUPPORT SYSTEM EIGENFUNCTIONS

In order to develop a controller design using the modal control approach, it was necessary first to determine the eigenfunctions for the spherical mirror and its three point support system. This was accomplished by three different methods which are:

1. Analytical solution of the beam equation for a thin flat circular plate subject to boundary conditions. This is an approximate solution since the actual mirror is a thin shallow shell.

2. Finite difference approximation to the continuous medium and solution obtained using the SAMIS computer program.

3. Experimental verification of 1 and/or 2 using time-lapse holography upon the physical system set into vibration.

The results of these three studies was presented recently at the April, 1971 meeting of the Optical Society in Tucson, Arizona. The presentation given, which is contained herein, establishes excellent agreement between the three approaches.

A.1 ANALYTICAL APPROACH

There are four types of vibrational modes when a homogeneous, isotropic, thin circular plate is simply supported at three points on the circumference.*

The type I is,

$$w_{Ii}^{(e)} = \sum_{m=0}^{\infty} \left[\frac{1+G_i \cos\left(\frac{2\pi}{3}m\right)}{F_m(k_i a)} \right] [J_m(k_i\rho) + B_m I_m(k_i\rho)] \cos m\varphi \qquad \text{(A-1)}$$

where k_i is the i^{th} solution from

$$\left[\sum_{m=0,3,6,9\ldots}^{\infty} \alpha_m(ka) \right] = 0$$

The type II is,

$$w_{IIi}^{(e)} = \sum_{m=0}^{\infty} \left[\frac{1+G_i \cos\left(\frac{2\pi}{3}m\right)}{F_m(k_i a)} \right] [J_m(k_i\rho) + B_m I_m(k_i\rho)] \cos m\varphi$$

where k_i is the i-th solution from (A-2)

$$\left[\sum_{\substack{m=1,2,4,5,7,8\ldots \\ m\neq 0,3,6,9,12\ldots}}^{\infty} \alpha_m(ka) \right] = 0$$

The type III is,

$$w_{IIIi}^{(o)} = \sum_{m=0}^{\infty} \frac{\sin\left(\frac{2\pi}{3}m\right)}{F_m(k_i a)} [J_m(k_i\rho) + B_m I_m(k_i\rho)] \sin m\varphi \qquad \text{(A-3)}$$

---

*The derivation of these results can be found in Perkin-Elmer Report No. 10299, Evaluation of the Thin, Deformable Active Optics Mirror Concept, No. 2, Sept. 15, 1970.

where k_i is the i-th solution from

$$\left[\sum_{\substack{m=1,2,4,5,7,8\ldots \\ m=/0,3,6,9\ldots}}^{\infty} \alpha_m(ka) \right] = 0 \qquad \text{(A-4)}$$

The type IV is,

$$w^{(o)}_{IVi,m} = [J_m(k_i\rho) + D_m I_m(k_i\rho)] \sin m\varphi$$

where $m = 3,6,9,12\ldots$ (A-5)

and where k is i-th solution from

$$F_m(ka) = 0$$

The resulting mode shapes are shown in Figures A-1 to A-12

One notes that types I and II are the even modes and types III and IV are the odd modes with respect to the x-axis. One notes also that the types I, II and III exert forces on the support points, whereas the type IV does not exert forces on the support points. Therefore, the types I, II and III require the support points in order for them to exist, and they are the modes which are unique to the plate with the simple support points on the circumference. The type IV is the group of modes which are also members of vibrational modes of the free plate without support points. These modes do not require the support points in order for them to exist.

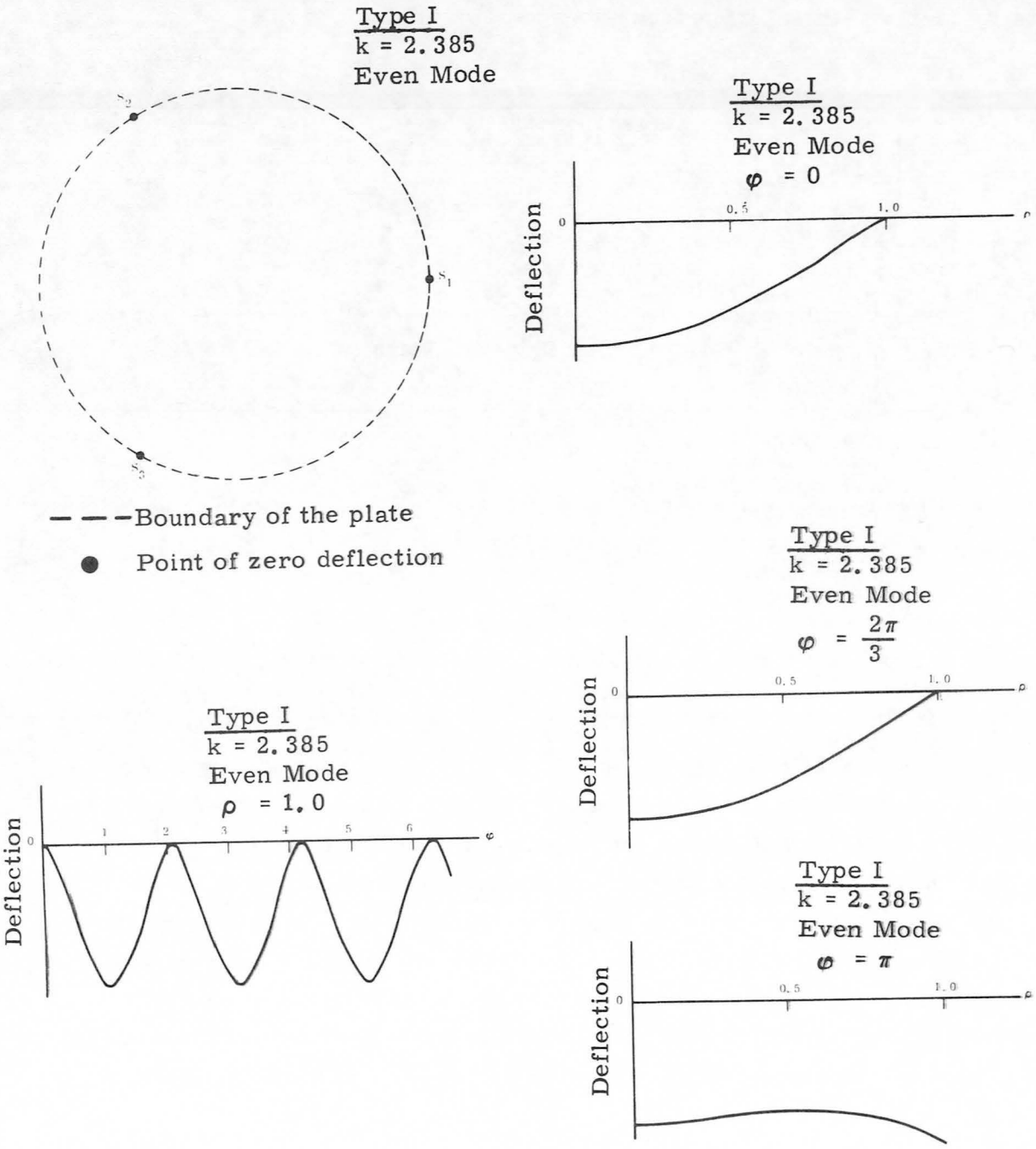


Figure A-1 Deflection Mode, Type I, k = 2.385, Even Mode

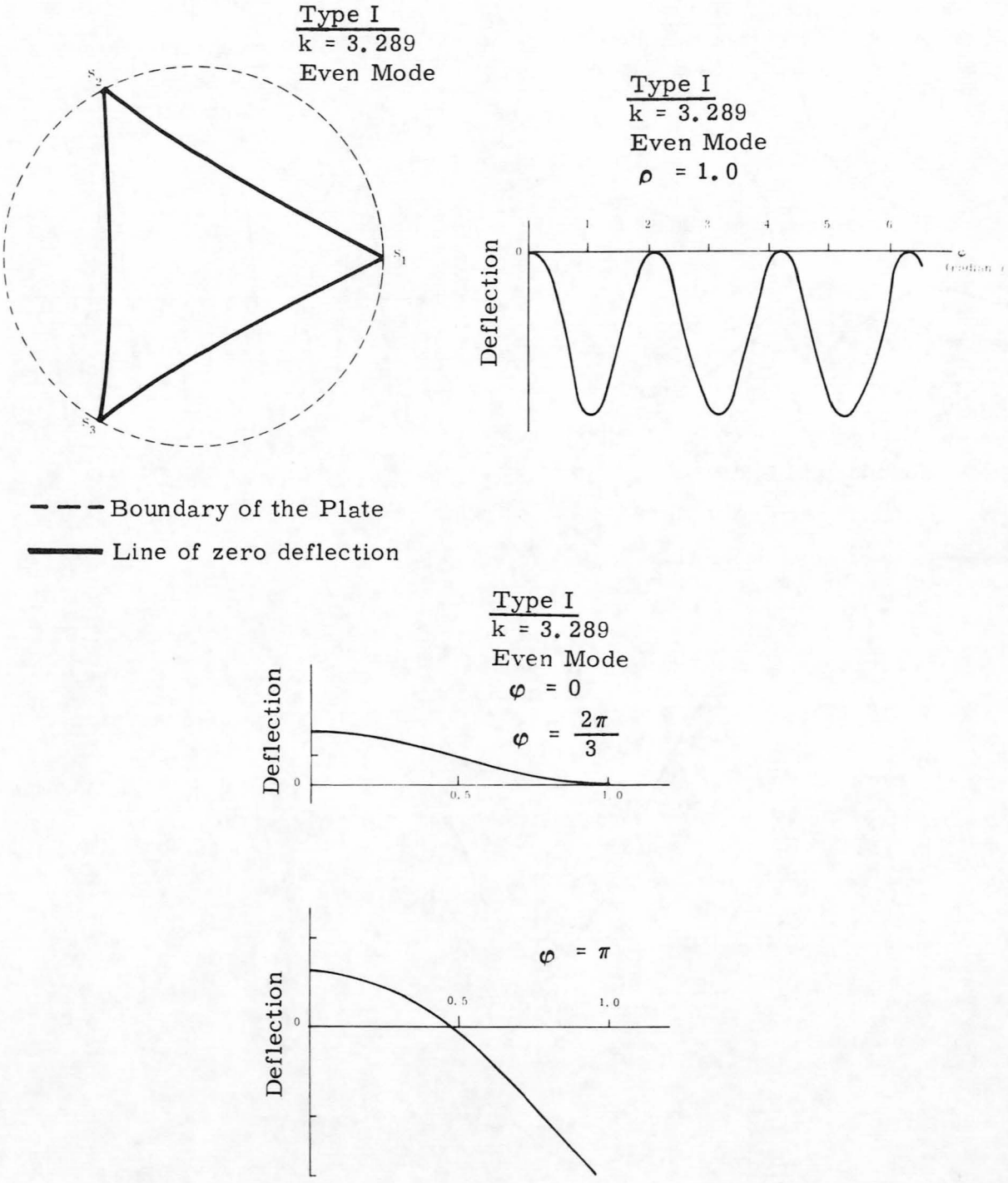


Figure A-2 Deflection Mode, Type I, k = 3.289, Even Mode

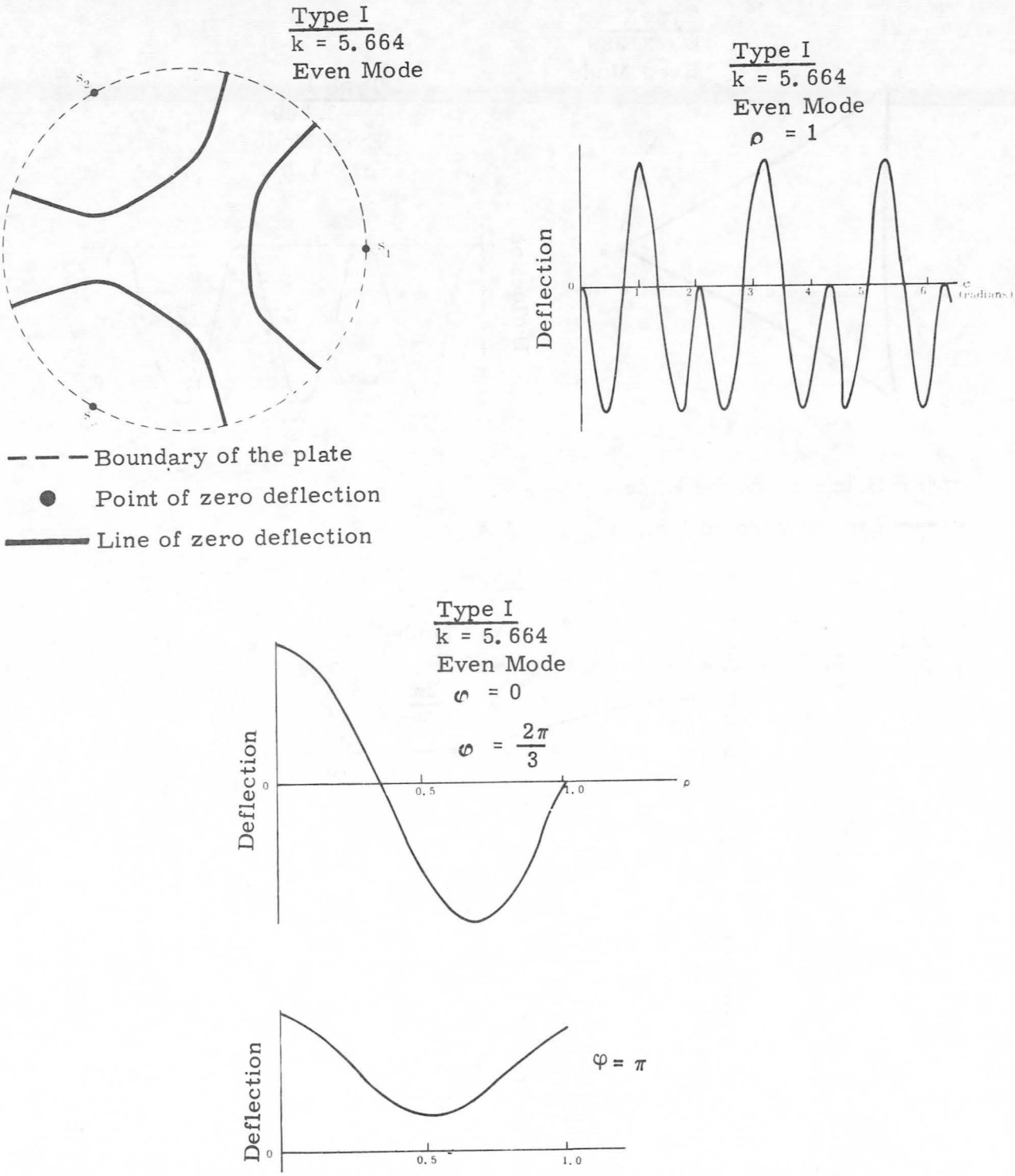


Figure A-3 Deflection Mode, Type I, k = 5.664, Even Mode

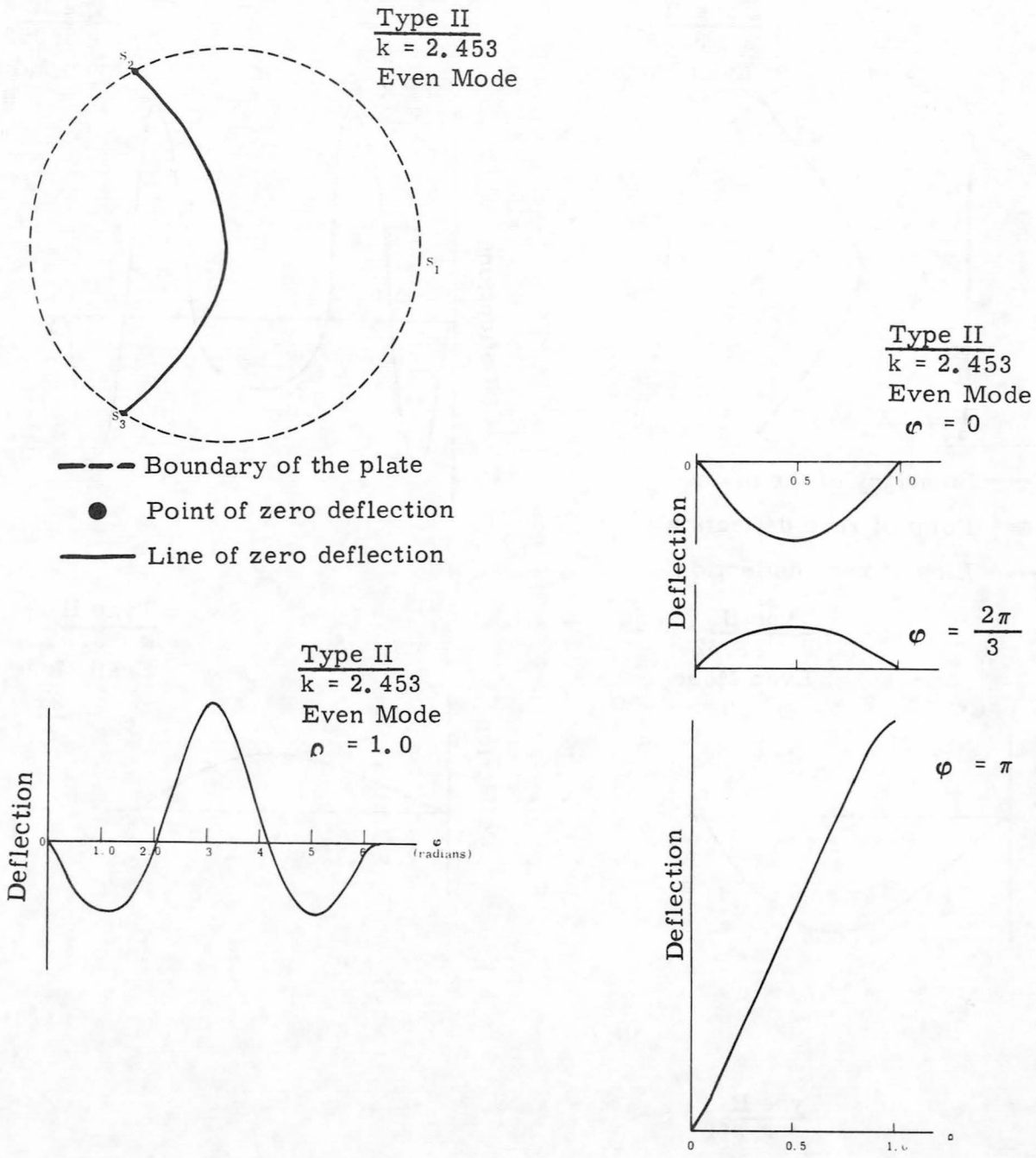


Figure A-4 Deflection Mode, Type II, k = 2.453, Even Mode

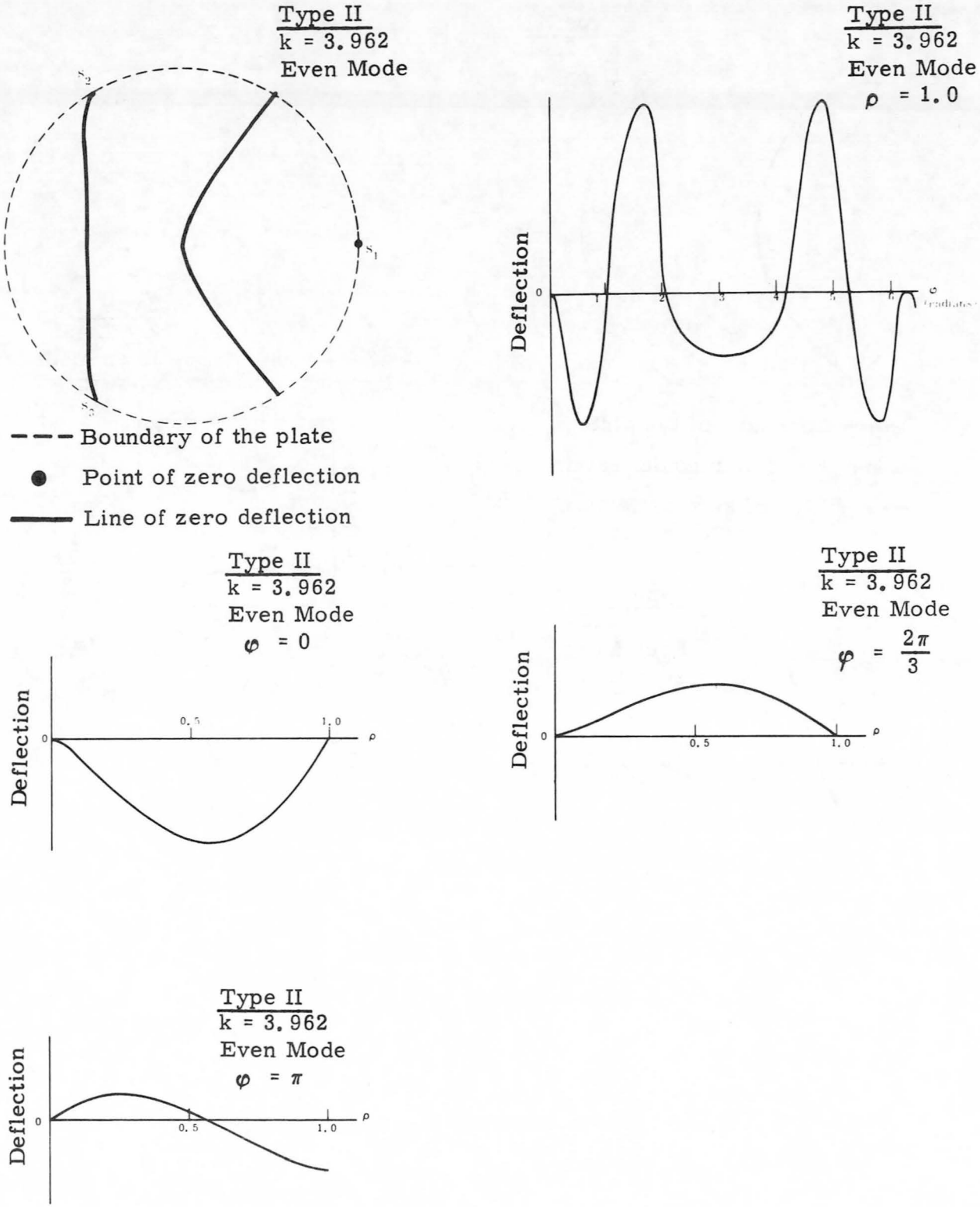


Figure A-5 Deflection Mode, Type II, k = 3.962, Even Mode

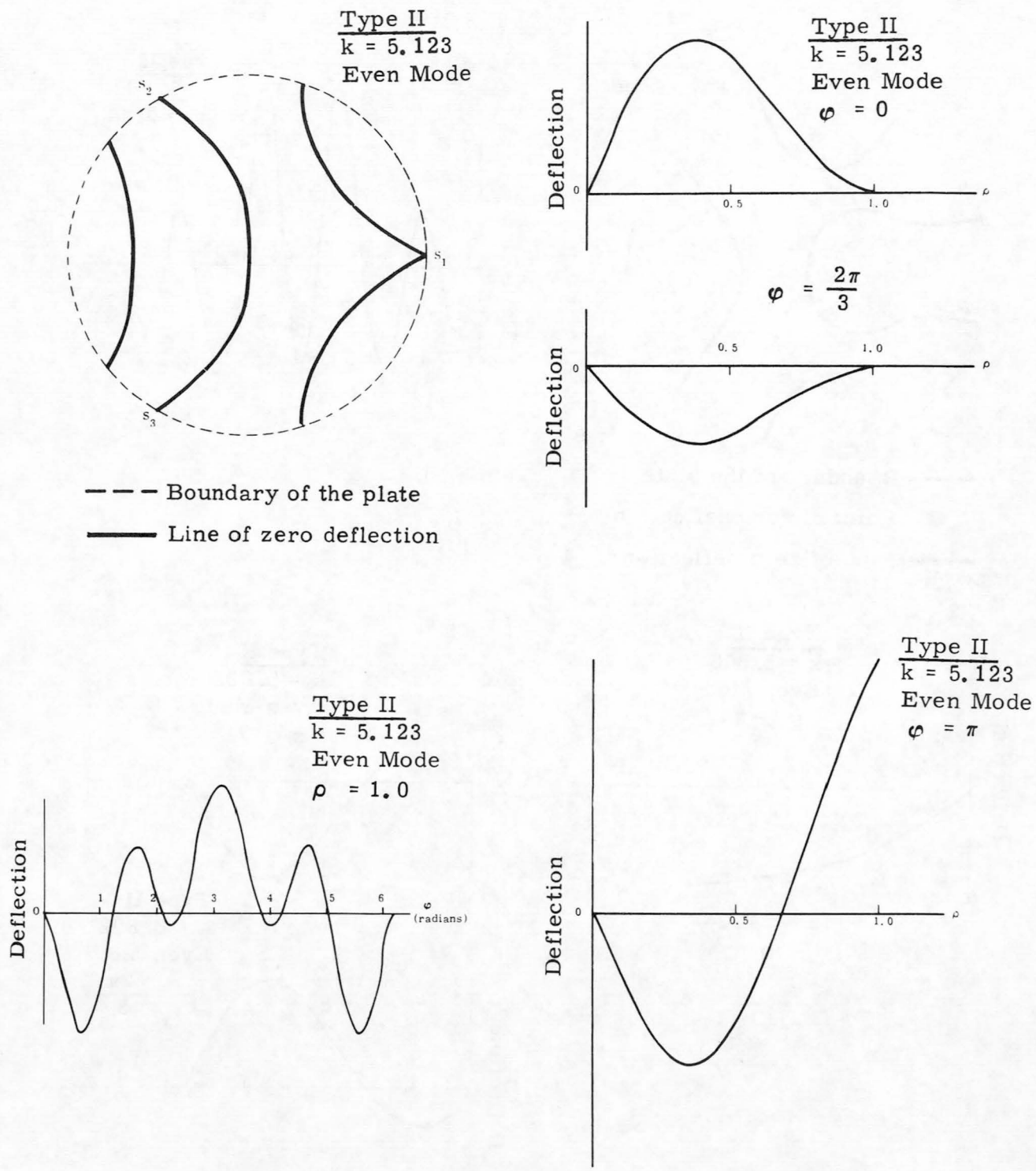
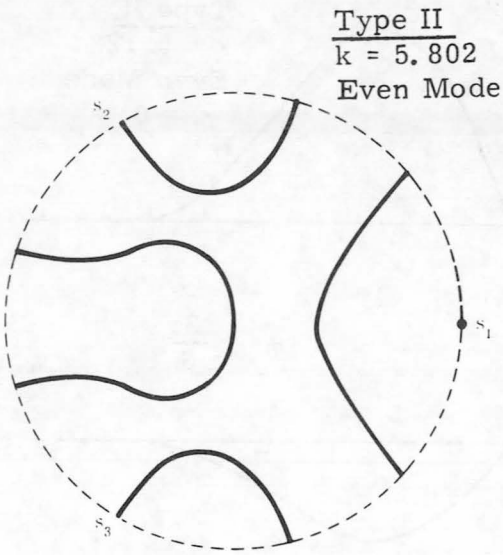
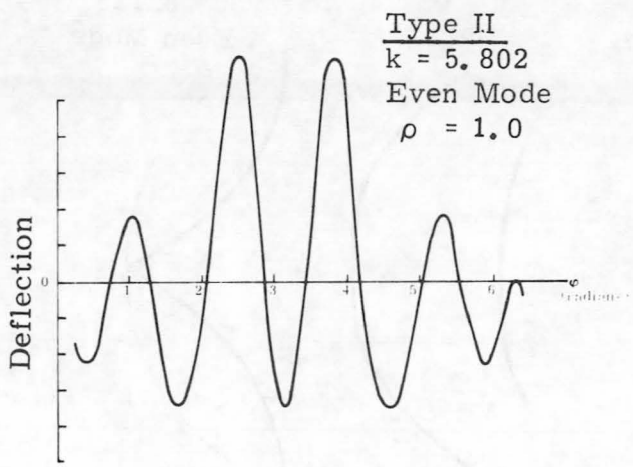


Figure A-6 Deflection Mode, Type II, k = 5.123, Even Mode

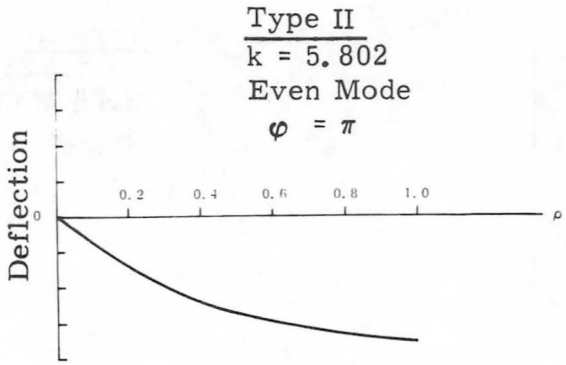


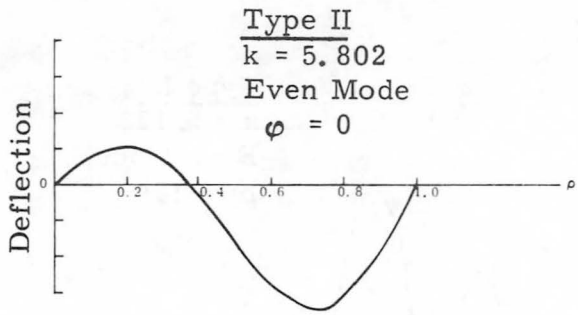


---Boundary of the plate

● Point of zero deflection

——— Line of zero deflection





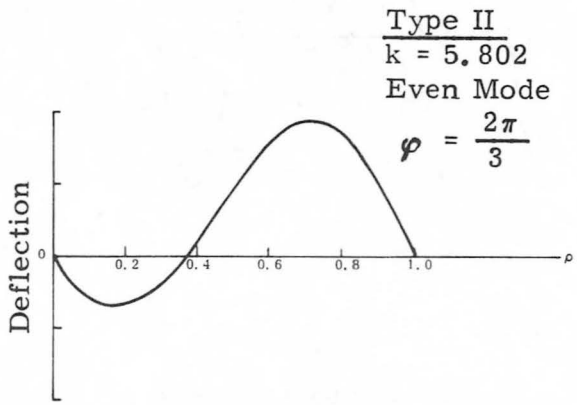


Figure A-7 Deflection Mode, Type II, k = 5.802, Even Mode

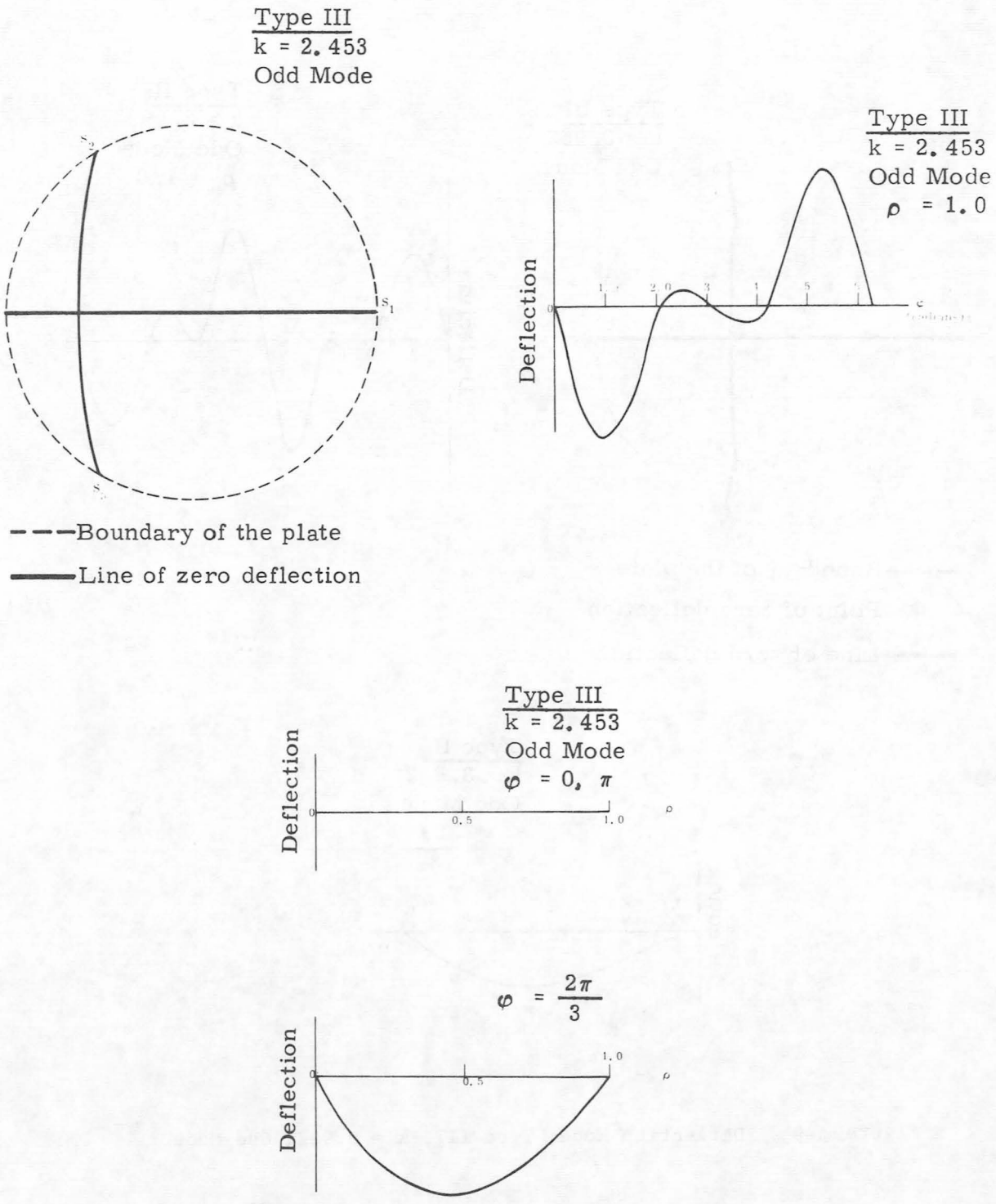


Figure A-8 Deflection Mode, Type III, k = 2.453, Odd Mode

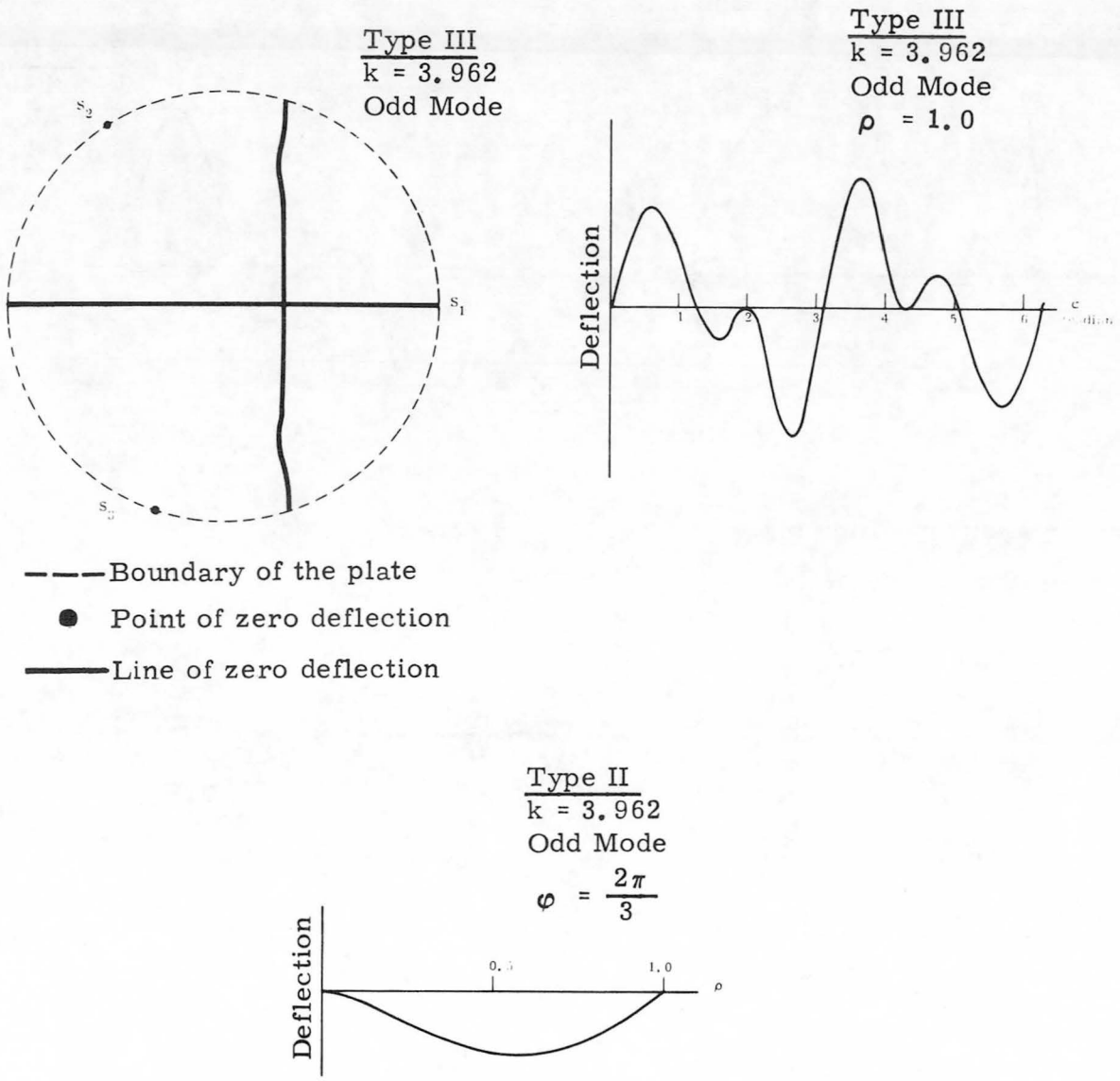


Figure A-9 Deflection Mode, Type III, k = 3.962, Odd Mode

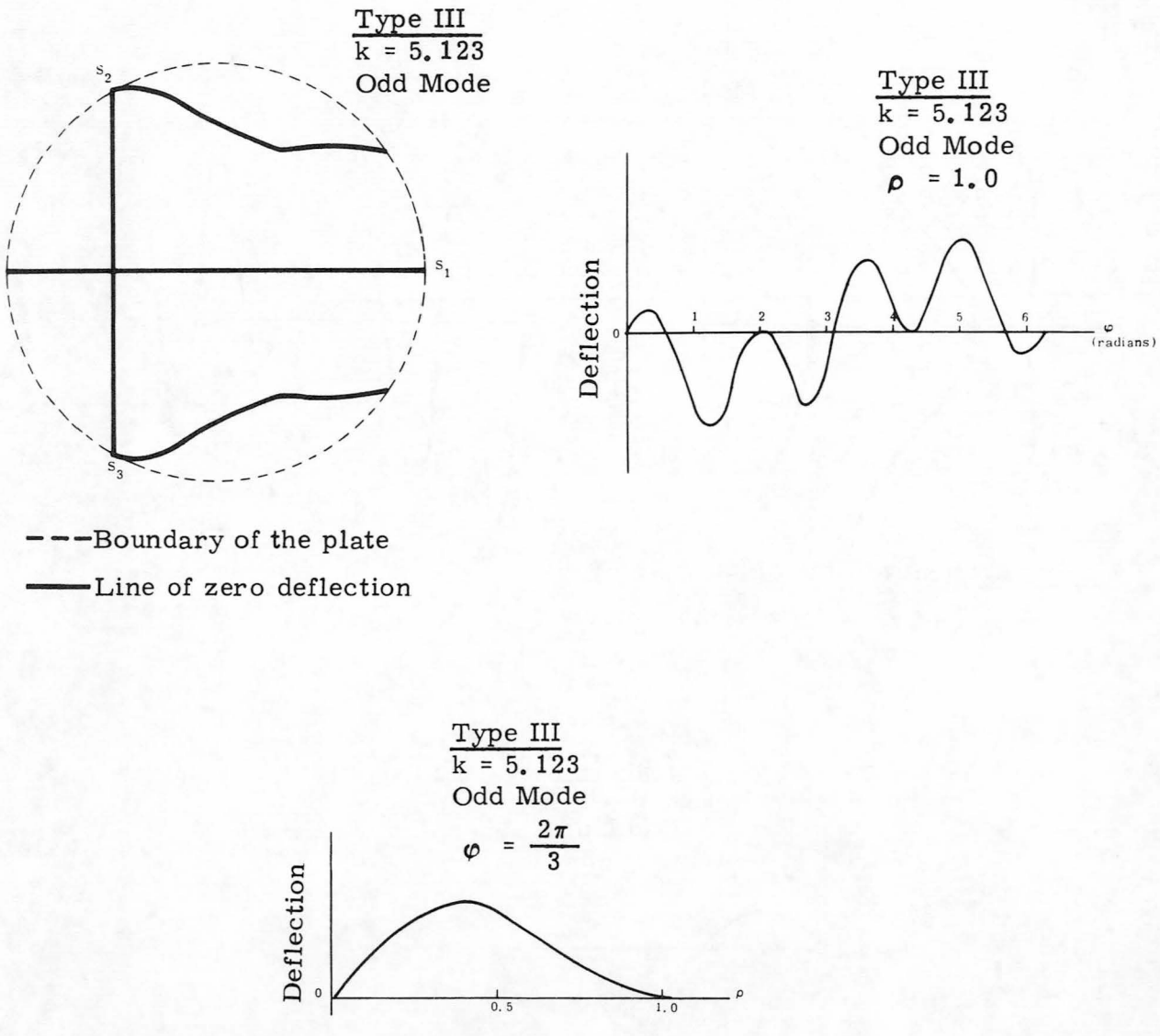


Figure A-10 Deflection Mode, Type III, k = 5.123, Odd Mode

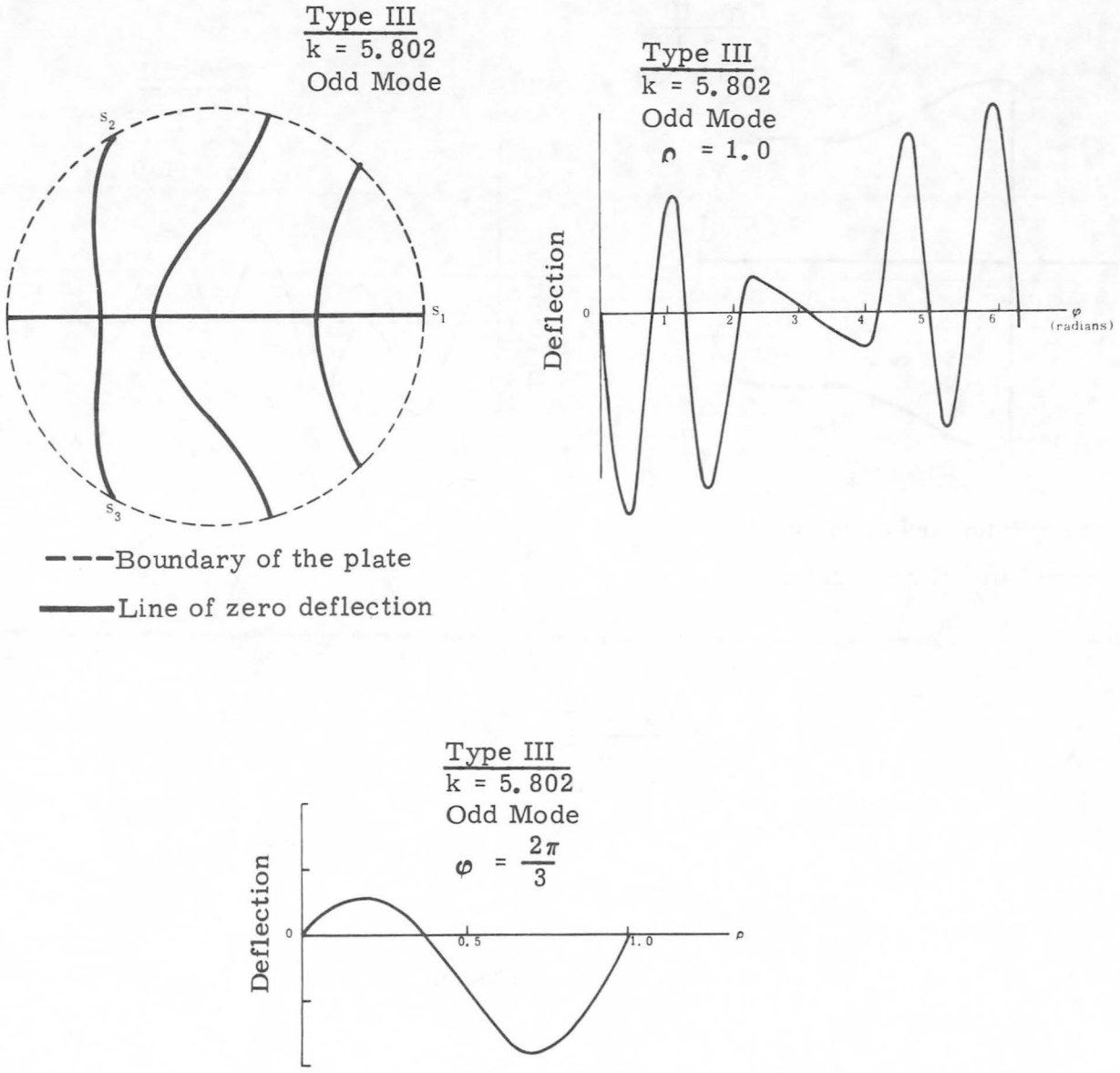


Figure A-11 Deflection Mode, Type III, k = 5.802, Odd Mode

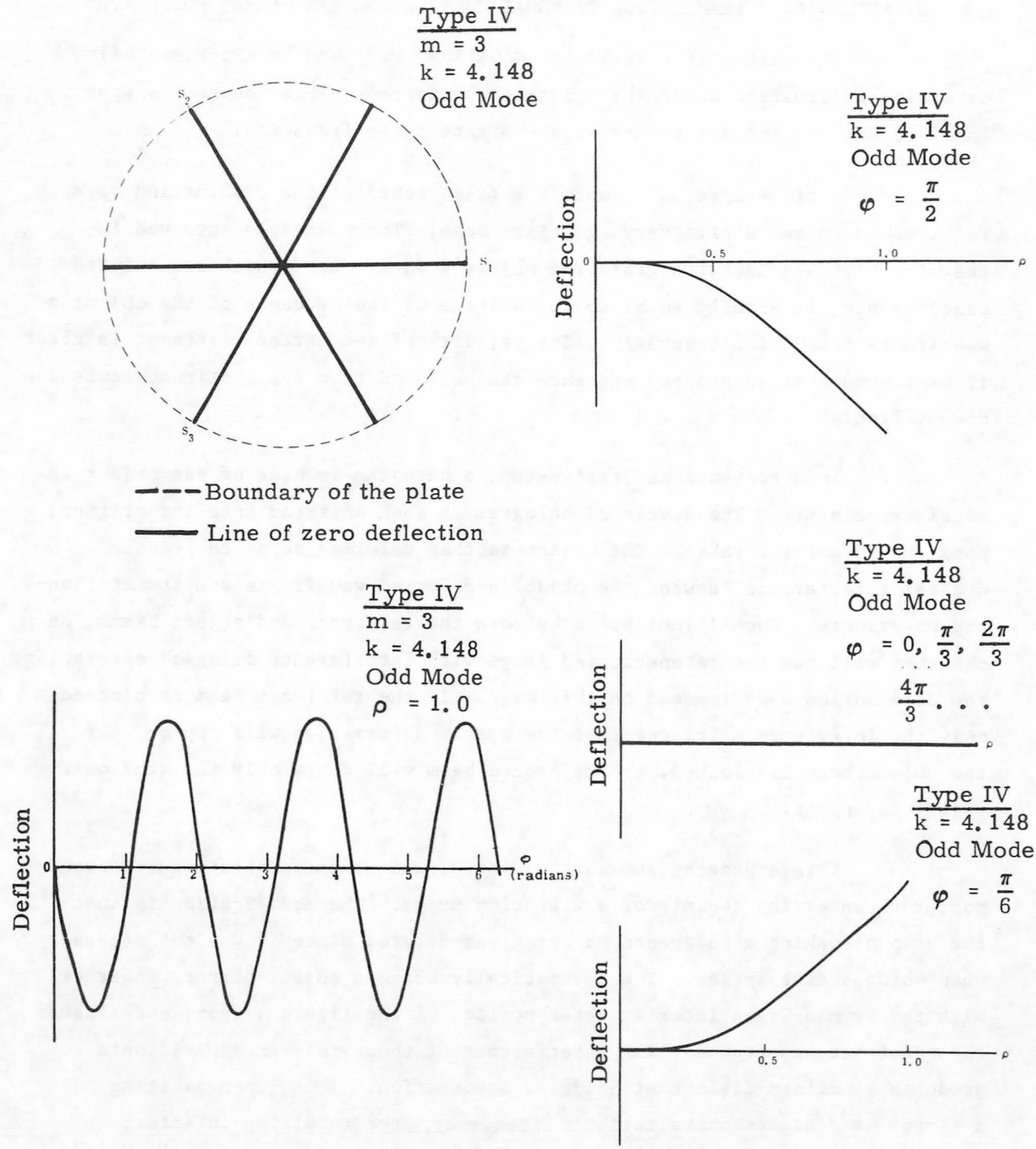


Figure A-12 Deflection Mode, Type IV, k = 4.148, Odd Mode

A.2 EXPERIMENTAL DETERMINATION OF MODAL CONTOURS BY TIME-LAPSE HOLOGRAPHY

The method of time-lapse holography was used to experimentally determine information about the thirty-inch mirror's vibration mode shapes. Ideally, each mode shape occurs at a characteristic frequency.

A time-lapse holograph is a film record of the combination of a reference beam and a time varying object beam. The principle involved is that the time average of a vibrating object's wavefronts, which are emitted continuously, is exactly equal to the average of the sequence of the object's wavefronts taken simultaneously. The validity of the latter statement is clear if we assume that an ordered sequence can be found from the continuous emission of wavefronts.

In a conventional test setup, a hologram is made of the object in a reference state. The developed hologram is then inserted into its original position when first taken. The object is then deformed so as to produce optical interference between the object's deformed wavefronts and its stationary wavefronts. Upon illumination by both the reference and object beams, an observer will see the reconstructed image with interference fringes representing the deformation superimposed on the image. If the reference beam is blocked, only the interference fringes that are due to deformation will appear. If the object beam is blocked, the reference beam will cause only the stationary object to appear.

This approach, somewhat modified, was taken to obtain interference patterns concerning the mirror's vibration modes. The modification is that the step of making a reference hologram was deleted since it was not necessary when using active optics. The automatically aligned object mirror, together with the Twyman-Green interferometer portion of the figure sensor, establishes the reference wavefronts. The interference of these reference wavefronts produces a uniform field that holds no information. Thus, upon exciting a mirror mode at its characteristic frequency, the resulting interference pattern contains the information necessary to determine the mode shape. A

contour plot of the mode shape is taken from the interference pattern because of the relationship between displacement amplitude and recorded light intensity. This relationship is fundamental in all fringe analyses, and its derivation is included in the appendix. The relationship is that the film exposure (intensity x time) E, is related to the amplitude of a sinusoidal vibration A, by

$$E = E_o \left(1 + mJ_o \left(\frac{4\pi A}{\lambda} \right) \right) \qquad \text{(A-6)}$$

where E_o (1 + m) is the average exposure with no vibration (A=0); m is a non-negative modulation factor less than unity (see appendix); and J_o is the zero order Bessel function. A sketch of the exposure as a function of vibration amplitude is shown in Figure A-13.

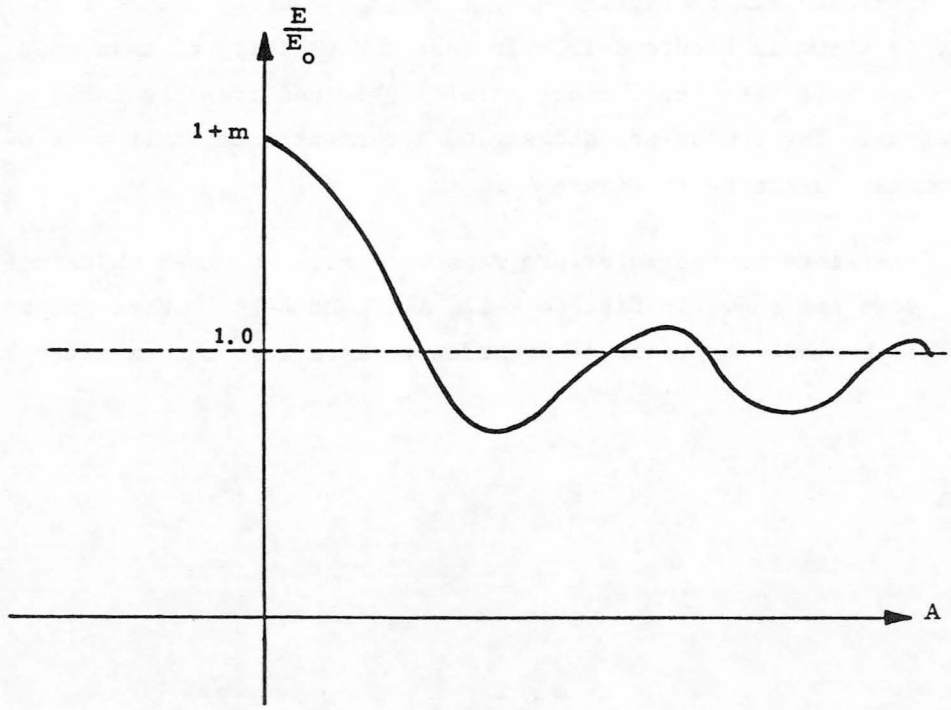


Figure A-13 Normalized Exposure as a Function of Vibration Amplitude for a Time Lapse Hologram

Figure A-14 shows a positive interferogram* taken at an excitation frequency of 272 Hz. This picture verifies the exposure relationship given by Eq.(A-6)in Figure A-13

It is first noted that the brightest triangular contour corresponds to the three known support points of zero axial diaplacement. As we move radially inward, the fringes appear with diminishing brightness, thereby indicating monotonically increasing amplitude. This fact is explained physically by considering that points of motion move from the stationary, bright, uniform field to a dark field and then back to light, and so on. Upon averaging light intensity at each point, a gray level will result depending upon the time spent in bright fringes and dark fringes. Points of little motion spend most of their time in the original bright field, while points of increasing displacement average out to decreasing modulation.

From analysis of Figure A-14, a contour plot of the mode shape was made and is shown in Figure A-15. To test the validity of this mode shape, a comparison was made with preliminary results obtained from the SAMIS computer program. The comparison shows good agreement with SAMIS mode 04 (radial-azimuthal) sketches in Figure A-16

Other interesting interferograms were made at other characteristic frequencies; some are shown in Figures A-17, A-18, and A-19 (More comparisons and checks will be made for these other modes to ascertain the validity of this data.)

*The word interferogram is used here interchangeably with hologram since an interferogram is a special case (on-axis parallel beam) of a hologram.

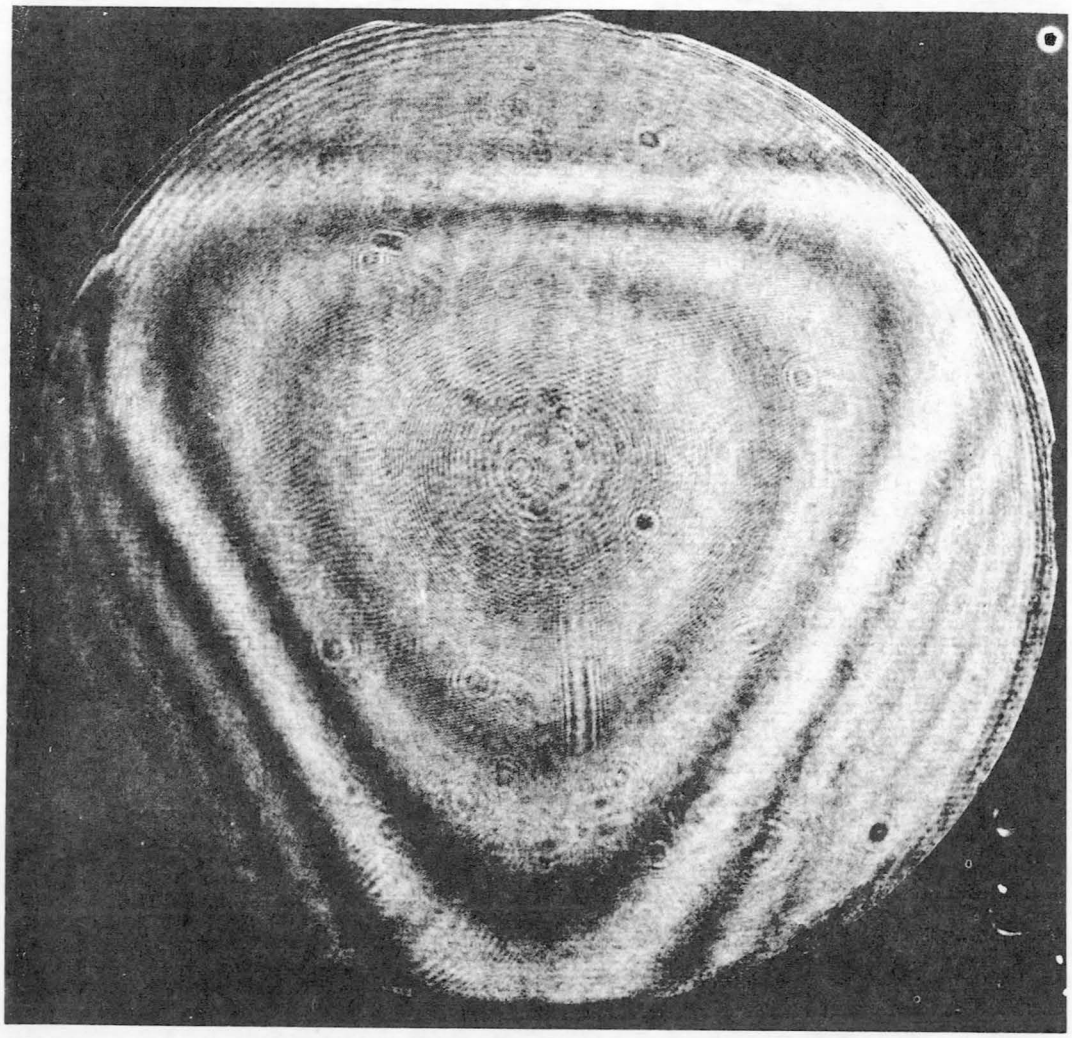


Figure A-14 Interferogram of Vibrating Mirror at 272 Hz

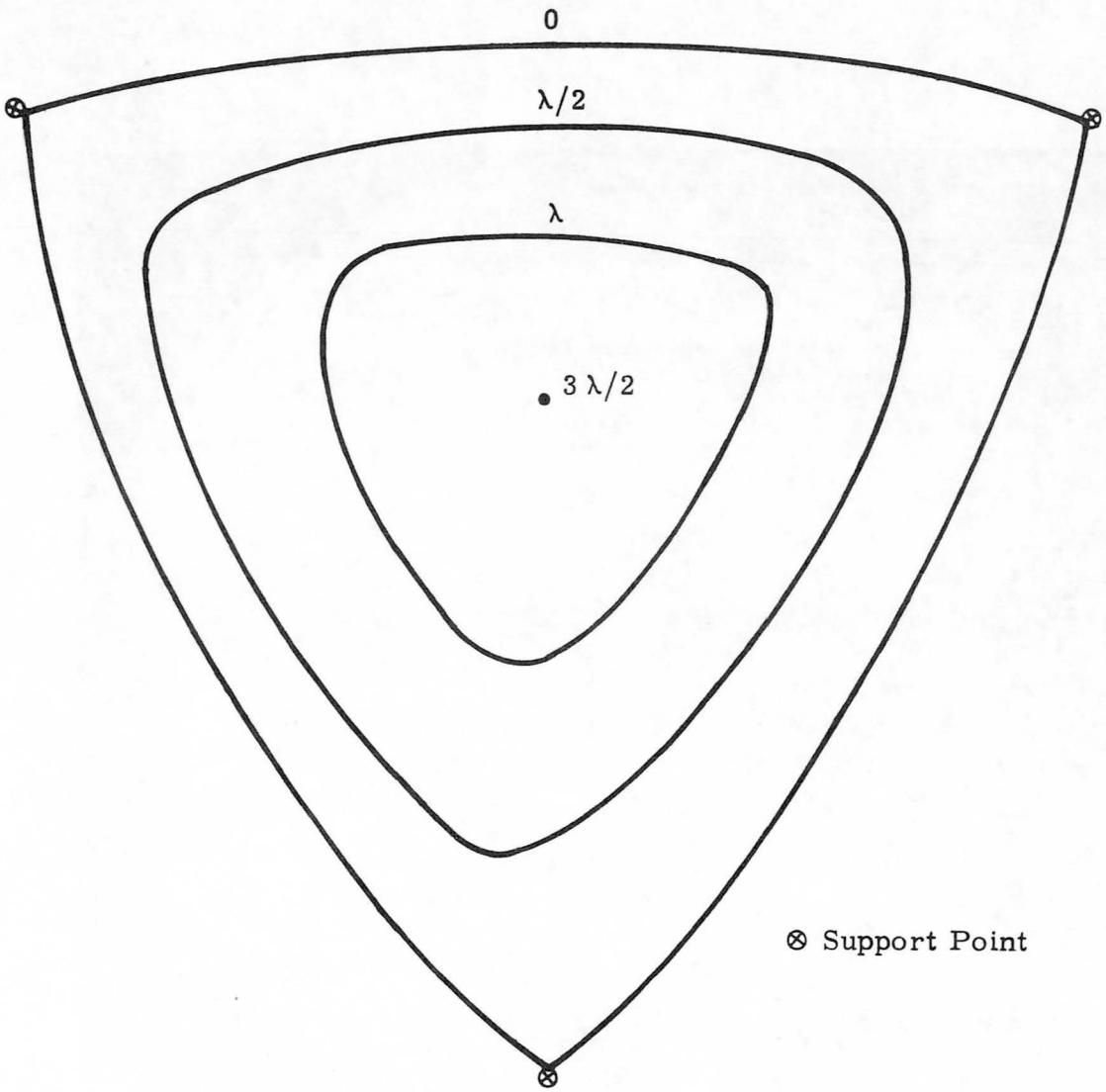


Figure A-15 Modal Contours Derived From Exposure in Figure A-14.

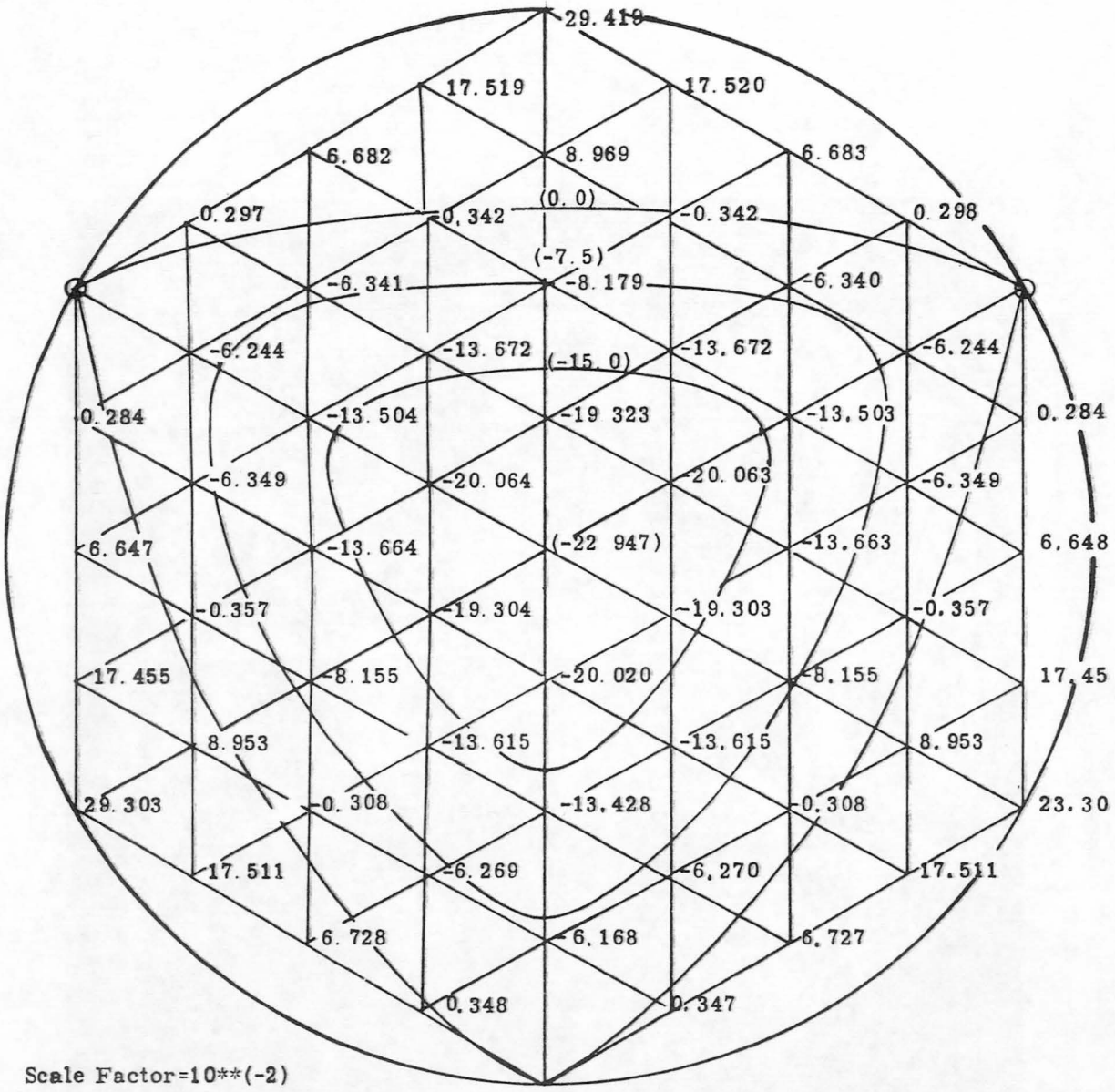


Figure A-16. Modal Contours Taken From SAMIS Program

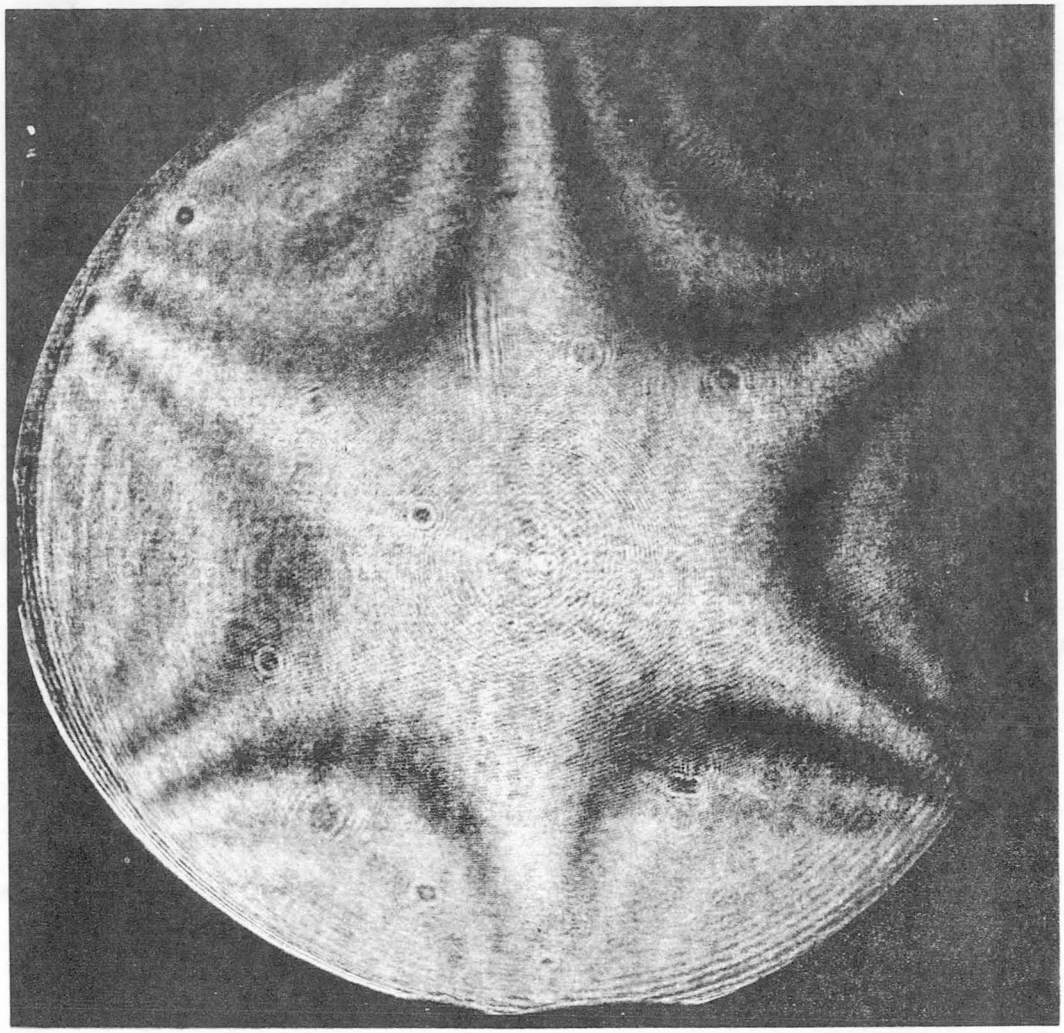


Figure A-17. Interferogram of Vibrating Mirror at 296 Hz

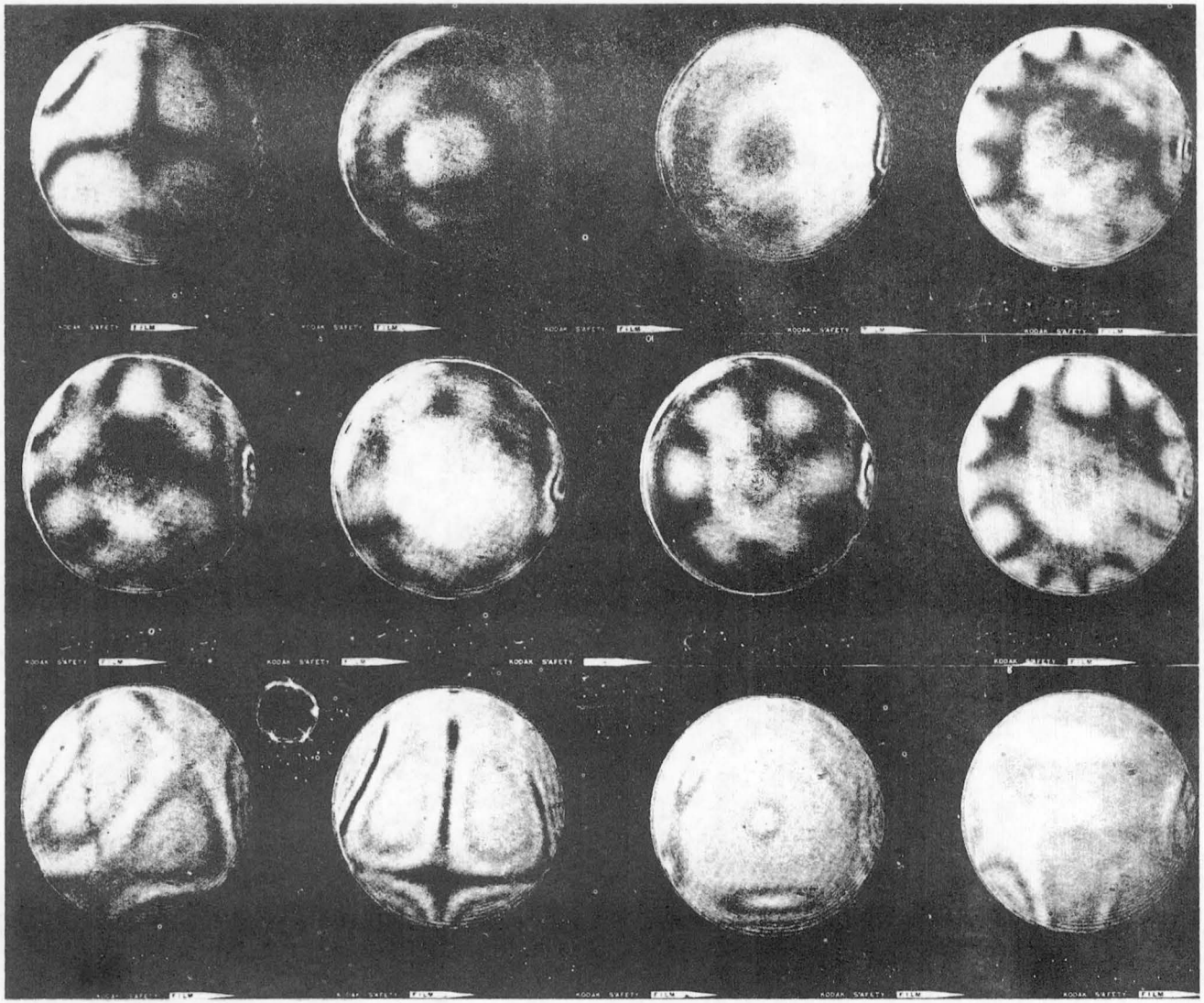


Figure A-18 Interferograms of Vibrating Mirror

A.3 RELATION BETWEEN MODAL CONTROL LAW AND MIRROR STIFFNESS CONTROL LAW

This section will show that when the number and placement of controlled displacement points and sensing points are identical, the controller design for perfect decoupling is the same whether the modal control approach is used or whether the original control law is used. The original control law used the mirror system's stiffness matrix to cancel the displacement interaction. The difference between the two systems is that the modal control law takes into account displacement error between the controlled points while driving the lower mode amplitude to zero; the stiffness control system drives displacements at the controller to zero without regard to displacement error between the control points.

To show the relation between the two methods let us consider the modal control approach. Following Creedon's notation we may expand the figure's displacement, w, and applied loading, p , according to

$$\begin{aligned} W(x,y\ t) &= \sum_i C_i(t)\,\mu_i(x,y) \\ P(x,y,t) &= \sum_i a_i(t)\,\mu_i(x,y) \end{aligned} \qquad (1)$$

where $\{\mu_i(x,y)\}$ is the orthonormal set of eigenfunctions of the mirror and support system. Their corresponding eigenvalues, λ_i, relate the mode amplitudes by

$$C_i = \lambda_i a_i \qquad (2)$$
$$(i = 1,2,3,\ldots m)$$

or in matrix notation

$$\bar{c} = \underline{\Lambda}\,\bar{a} \tag{3}$$

where $\bar{c}$ and $\bar{a}$ are the mode amplitude column vectors of dimension M x 1 = 58 x 1 and $\underline{\Lambda}$ is the eigenvalue diagonal matrix of dimension M x M = 58 x 58. Writing Eq. (1) in matrix notation

$$\begin{aligned} \bar{W} &= \underline{U}\,\bar{c} \quad (M \times 1 = 58 \times 1) \\ \bar{P} &= \underline{U}\,\bar{a} \quad (M \times 1 = 58 \times 1) \end{aligned} \tag{4}$$

where each column of $\underline{U}$ (dimension M x M ° 58 x 58) represents an eigenfunction whose components are a mode amplitude evaluated at the sensor points.

From equations (3) and (4):

$$\bar{c} = \underline{\Lambda}\,\underline{U}^{-1}\,\bar{p} \tag{5}$$

It is also known that the influence coefficient matrix, α (dimension M x M = 58 x 58), relates applied load to resulting displacement by

$$\bar{W} = \underline{\alpha}\,\bar{P} = \underline{U}\,\bar{C} \quad \text{(by Eq. (4))}$$

Then

$$\bar{C} = \underline{U}^{-1}\,\underline{\alpha}\,\bar{P} \tag{6}$$

Equating Eq. (5) to Eq. (6)

$$\underline{U}^{-1}\,\underline{\alpha} = \underline{\Lambda}\,\underline{U}^{-1} \tag{7}$$

or

$$\underline{\alpha} = \underline{U}\,\underline{\Lambda}\,\underline{U}^{-1}$$

But since the eigenfunctions form an orthonormal set (not complete)

$$\underline{U}^{-1} \doteq \underline{U}^{t} \text{ (transpose)} \tag{8}$$

so that

$$\underline{\alpha} \doteq \underline{U}\,\underline{\Lambda}\,\underline{U}^{t} \tag{9}$$

Equation (9) is the key relation between the two control methods. In the stiffness decoupling approach the controller is represented by the stiffness matrix

$$\underline{k} = \underline{\alpha}^{-1} = (\underline{U}^{t})^{-1}\,\underline{\Lambda}^{-1}\,\underline{U}^{-1} = \underline{U}\,\underline{\Lambda}^{-1}\underline{U}^{-1} \tag{10}$$

But the modal controller according to figure 5-1 is

$$\underline{\beta} = \underline{H_N}^{-1}\,D_{(\underline{S})}\,\underline{U}^{-1} \tag{11}$$

where H_N is the pad compensation matrix which prepares the load distribution to be a scalar multiple of a resulting displacement for any specific mode. Since $\underline{H_N} = \underline{U}^{t}$ for small pads (see reference 2),

$$\underline{H_N}^{-1} = (\underline{U}^{t})^{-1} = \underline{U},$$

So that

$$\underline{\beta} = \underline{U}\,\underline{D}_{(S)}\,\underline{U}^{-1} = \underline{U}\,D_{(S)}\,\underline{U}^{t} \tag{12}$$

Thus, the modal controller matrix, $\underline{\beta}$, is identical to the stiffness controller matrix, $\underline{k}$ if $D_{(\underline{S})} = \underline{\Lambda}^{-1}$. Other wise, they differ by a scaler matrix.

NATIONAL AERONAUTICS AND SPACE ADMISTRATION
WASHINGTON, D.C. 20546

OFFICIAL BUSINESS
PENALTY FOR PRIVATE USE $300

FIRST CLASS MAIL

POSTAGE AND FEES PAID
NATIONAL AERONAUTICS AND
SPACE ADMINISTRATION

U.S.MAIL

NASA 451

POSTMASTER: If Undeliverable (Section 158 Postal Manual) Do Not Return

"The aeronautical and space activities of the United States shall be conducted so as to contribute . . . to the expansion of human knowledge of phenomena in the atmosphere and space. The Administration shall provide for the widest practicable and appropriate dissemination of information concerning its activities and the results thereof."

—NATIONAL AERONAUTICS AND SPACE ACT OF 1958

NASA TECHNOLOGY UTILIZATION PUBLICATIONS

These describe science or technology derived from NASA's activities that may be of particular interest in commercial and other non-aerospace applications. Publications include:

TECH BRIEFS: Single-page descriptions of individual innovations, devices, methods, or concepts.

TECHNOLOGY SURVEYS: Selected surveys of NASA contributions to entire areas of technology.

OTHER TU PUBLICATIONS: These include handbooks, reports, conference proceedings, special studies, and selected bibliographies.

Details on the availability of these publications may be obtained from:

National Aeronautics and
Space Administration
Code KT
Washington, D.C. 20546

Technology Utilization publications are part of NASA's formal series of scientific and technical publications. Others include Technical Reports, Technical Notes, Technical Memorandums, Contractor Reports, Technical Translations, and Special Publications.

Details on their availability may be obtained from:

National Aeronautics and
Space Administration
Code KS
Washington, D.C. 20546

NATIONAL AERONAUTICS AND SPACE ADMINISTRATION
Washington, D.C. 20546